Polarizing ^{3}He by Spin Exchange with Potassium

Thesis by

Guodong Wang

In Partial Fulfillment of the Requirements

for the Degree of

Doctor of Philosophy

California Institute of Technology

Pasadena, California

2004

(Defended May 18, 2004)

To

My parents

and

My sister

Acknowledgements

First of all, I want to thank my advisor, Professor Emlyn Hughes, for his guidance on my research over last five years. Without his support and guidance, this work cannot be done.

I would like to thank my fellow members in our group. They were invaluable for the work in this thesis as well as for the success of my graduate studies at Caltech. Thanks to Wenjin Shao, who is my labmate and one of my best friends throughout these years, for the discussions and the lab work done by us together. When I first joined the group, Tina Pavlin showed me everything from the very beginning. Her curiosity, intelligence, and diligence always inspired me and pushed me to advance. I am also grateful to Kleda Beja, Mark Jones and Peter Mastromarino. Special thanks go to Georgia Freuch, the secretary of the group, for her countless help during these years.

I wish to thank Rick Gerhart, the glassblower at Caltech. It is my good fortune that his amazing glassblowing skill is readily available for this thesis work. Also, thanks go to Richard Fuzesy and Faye Witharm, for helping us build the vacuum system.

Outside the group, I am grateful to Dave Boozer and Christoph Naegerl. During

the first year of my graduate studies, I worked with Dave and Christoph on atomic trap experiments. Their guidance and tutoring educated me into the experimental atomic physics. I also wish to thank my friends at Caltech, George Ouyang and Xinkai Wu. My years at Caltech would be less memorable without them.

I also thank numerous professors at Caltech, whose classes taught me a broad range of physics knowledge. I regard taking these classes as an important part of my graduate studies. Thanks to Professor Mark Wise, Professor John Preskill, Professor Jeff Kimble, and there are just too many names to be listed here. Especially, I would like to express my thanks to Professor Kip Throne and Professor Roger Blandford. I was in their class and was a Teaching Assistant later in the same course. Both from the classroom and from the TA collaboration, I gained a better understanding on classical physics and a cherishable teaching experience, which would be beneficial to my future career.

Finally, I have to thank my parents and my sister. Their love and support drive me here.

Abstract

We present experimental studies on the spin-exchange optical pumping of ^{3}He using alkali metal potassium vapor. High ^{3}He polarizations are achieved using lower laser power than traditional rubidium-^{3}He pumping studies. In addition, spin-exchange rate coefficient measurements for potassium-^{3}He, rubidium-^{3}He and cesium-^{3}He pairs are reported.

By spin-exchange optical pumping with potassium vapor, a high ^{3}He polarization has been achieved in a mid-sized double-chamber glass target cell using only 5 watts of Ti:sapphire laser power. The spin-exchange rate coefficients of potassium-^{3}He, cesium-^{3}He and rubidium-^{3}He pairs are measured and compared. The results are $k_{SE} = (4.0 \pm 0.3) \times 10^{-20}\,\mathrm{cm}^3/\mathrm{sec}$ for the potassium-^{3}He pair, $k_{SE} = (6.5 \pm 0.4) \times 10^{-20}\,\mathrm{cm}^3/\mathrm{sec}$ for the rubidium-^{3}He pair and $k_{SE} = (13.6 \pm 1.3) \times 10^{-20}\,\mathrm{cm}^3/\mathrm{sec}$ for the cesium-^{3}He pair.

The results are consistent with theoretical predictions and confirm that the efficiency for spin-exchange polarization of ^{3}He with potassium is significantly higher than with rubidium or cesium. The results motivate the development of high power diode lasers tuned to the appropriate potassium wavelengths. Applied to the production of polarized ^{3}He as an atomic beam source for colliders, these developments could

have significant impact on future studies of neutron spin structure. These studies may also have impact on magnetic resonance imaging using hyperpolarized ^{3}He.

Contents

List of Figures

List of Tables

Chapter 1

Introduction

1.1 Overview

This thesis work focuses on the experimental studies of polarizing ^{3}He using potassium vapor via the method of spin-exchange optical pumping [28, 47, 62]. Hyperpolarized ^{3}He has a wide range of applications both in fundamental nuclear physics and in the field of magnetic resonance imaging (MRI). In the following sections of this chapter, the applications of hyperpolarized ^{3}He in nuclear physics and medical imaging are first reviewed; then the methods of producing polarized ^{3}He are discussed. In the last section, discussions of the motivation and goals as well as the organization of this thesis are presented.

1.2 Applications of Polarized ^{3}He

1.2.1 Polarized ^{3}He as a Nuclear Scattering Target

A polarized ^{3}He nucleus can be modeled as a polarized neutron bound to two unpolarized protons. The orientations of the proton spins are anti-parallel due to the

Pauli Exclusion principle. Therefore, in spin-dependent deep inelastic scattering experiments, the polarized ^{3}He can be used as a polarized neutron target to study the internal spin structure of the neutron. Over the past two decades, a series of deep inelastic electron-neutron scattering experiments using polarized ^{3}He targets have been performed at the Stanford Linear Accelerator Center (SLAC) to determine the neutron spin structure functions [56]. The development and production of large volumes of highly polarized ^{3}He for nuclear targets have already had an enormous impact on fundamental studies of the internal spin structure of the nucleon.

Before the emergence of polarized ^{3}He targets, experiments were performed on the experimental determination of the nucleon spin structure using solid proton and deuteron targets. Researchers are interested in such experiments not only because it helps us understand nucleon structure, but also because it provides fundamental tests of quantum chromodynamics (QCD). For example, QCD predicts a relationship between the spin-dependent deep inelastic lepton-nucleon scattering cross sections and the low energy weak coupling constants found in neutron decay, known as the Bjorken sum rule [14]. In addition, another relationship called the Ellis-Jaffe sum rule predicts values for the individual quark spin distributions in the nucleon [18]. Therefore, deep inelastic scattering experiments with polarized nucleon targets play an important role in experimental nuclear physics.

The first experimental studies of the Ellis-Jaffe sum rule used solid, polarized ammonia targets in the 1980s to derive the proton spin structure [20]. Until 1993, there was no polarized neutron target. To study about the neutron, deuterated ammonia was used as a deuteron target, and then the neutron spin structure was derived from the combination of polarized proton and deuteron target measurements. The associated uncertainties were large in these experiments. Since the proton target was solid, QED radiative corrections due to the unpolarized materials in the target also increased the systematic uncertainties.

These limitations were overcome by using polarized ^{3}He targets. As mentioned above, the spin of a polarized ^{3}He nucleus can be modeled well as a polarized neutron. This model is accurate to the extent that the initial state is found in an S-state [30], just as in the case of spin-dependent deep inelastic scattering experiments. In these experiments, the advantages of polarized ^{3}He targets over the previous solid nucleon targets are obvious, since the neutron results do not depend on previous proton measurements. The polarized ^{3}He is a gas target, so QED radiative corrections are also greatly reduced compared to solid targets. Over the past ten years, fixed target electron scattering experiments, using polarized ^{3}He, have been performed at numerous nuclear and particle accelerator centers around the world [33, 40, 43, 37, 82, 59, 64].

1.2.2 Magnetic Resonance Imaging Using Hyperpolarized ^{3}He

Nowadays magnetic resonance imaging (MRI) has become a mainstream imaging tool in medical research and in clinical disease diagnosis. MRI can produce unparalleled high quality images of human body tissues. The polarized He gas has been applied in new MR imaging technique [38], soon after it was developed in the field of nuclear physics.

Current MRI techniques detect the proton nuclear magnetic resonance signals from the dense population of hydrogen protons in the form of water existing in tissues. During MRI, a strong magnetic field around the body is generated to produce a proton thermal polarization, which follows Boltzmann statistics:

$$P = \frac{n_+ - n_-}{n_+ + n_-} = \frac{e^{\mu \cdot B/kT} - e^{-\mu \cdot B/kT}}{e^{\mu \cdot B/kT} + e^{-\mu \cdot B/kT}} = \tanh(\frac{\mu \cdot B}{k_B T}). \tag{1.1}$$

Then, an rf pulse at the proton resonance frequency is applied to the tissues in order to make the protons precess along the main magnetic field. When the rf pulse is turned off, the relaxation signals of the protons at resonance are detected.

The signal size depends on the proton density (i.e., water density in the tissues), and on the relaxation rates of the signal, which in turn are sensitive to the surrounding environment. Actually the discovery that the relaxation rates of nuclear magnetic resonance signals in tissues and in tumors are different was among the first motivations for using magnetic resonance to detect diseases [16].

To localize the signal positions in the tissues, additional magnetic field gradients in three dimensions are added to the main field, which alter the main magnetic field locally. Such gradients are turned on and off in a thin slice through the tissues so that the detected signals build up an image at this slice. When the gradients have scanned the whole body of the subject, all images of the slices can be combined together to get an entire image of the tissues.

The limitations of the current MRI technique originate from two conditions. First, since MRI makes use of the presence of water protons in the body, it is hard to get a clear MRI image of a human body tissue which contains no water. For example, the conventional MRI images of human lungs are far away from satisfactory. In the case of lungs imaging, the air space in the lungs contains too little water vapor to produce a successful MRI image. Although Computed Tomography (CT) can be used to obtain lungs images, the subject has to be exposed to x-ray radiation. This disadvantage is especially relevant when imaging pregnant women and children, since developing cells are very vulnerable to x-ray exposure.

The second factor that limits the proton-based MRI is the low proton thermal equilibrium polarizations. Since human imaging must be performed at room temperature, to get a reasonable signal size, uniform high magnetic fields have to be applied. Typically superconducting magnets are used to generate a ~ 2 Tesla field for MRI. Even with such high magnetic fields, the proton polarization is only on the order of 10^{-6}, according to Equation 1.1. In addition, the high cost associated with superconducting magnets is a factor limiting the technology.

In the 1990s, researchers realized that hyperpolarized ^{3}He gas by spin-exchange optical pumping with alkali vapor can be used in MRI to overcome the limitations mentioned above. The idea is to get a ^{3}He based image instead of a proton-based image, once the subject tissues absorb a certain amount of polarized ^{3}He. As a result, dynamic *in vivo* lung MRI is accessible when the subject inhales polarized ^{3}He gas.

It is worth noting that inhaling laser-polarized ^{3}He gas into lungs has no side effects. The only concern is that the oxygen percentage in the subject's body could be reduced when large quantities of ^{3}He gas are inhaled. In clinical ^{3}He MRI, one or two liters of ^{3}He are used, which does not cause an oxygen level problem for the subject [71].

Besides lung imaging, polarized ^{3}He can also be applied to build low-cost, low-field MRI systems. The polarized ^{3}He gas by spin-exchange optical pumping with alkali metal vapor can reach polarizations near $\sim 50\%$, which is five orders of magnitude larger than the thermal equilibrium polarization in water. What's more, the non-thermal-equilibrium ^{3}He polarization does not depend on the strength of the main magnetic field. This advantage can be used to realize MRI at a relative low magnetic field without using superconducting magnets. Consequently, the MRI system cost can be greatly reduced.

One example among the efforts of building a low-field laser-polarized noble gas MRI system is a collaboration between our group and Stanford in Appendix A [66]. Combining the laser-polarized noble gas MRI technique and a low-field MRI technique, namely, Pre-polarized MRI, images of gaseous polarized ^{129}Xe and water cells at room temperature were obtained with a low-field magnetic resonance scanner. This potentially low-cost imaging technique offers the possibility of high-resolution imaging using both polarized noble gas and proton MRI of tissues in the same scanner.

1.3 ^{3}He Polarizing Methods

1.3.1 Metastable Optical Pumping

To polarize ^{3}He, one straightforward method is to use the technique of optical pumping. However, the energy splitting of the ^{3}He $1S$ to $2P$ states is in the far ultraviolet regime so that no laser light is available. Therefore, instead of direct optical pumping the ground state of ^{3}He, the metastable 2^3S_1 state of ^{3}He is used. In this technique, the electron's spin is polarized by optical pumping with circularly polarized laser light at 1.08 μm between the 2^3S_1 and 2^3P_0 states. Then, the electron's spin transfers its polarization to the ^{3}He nucleus via a hyperfine interaction [12]. By this method, the ^{3}He nucleus can be highly polarized in a short time.

Although ^{3}He can be polarized very fast with the metastable state optical pumping technique, it is hard to get high densities of polarized ^{3}He. The reason is that one needs to produce the ^{3}He metastable state 2^3S_1 by rf discharge first, which limits the ^{3}He pressure to be on the order of a few torrs. To get polarized ^{3}He in large amounts, a complicated vacuum flow system has to be constructed. Today's polarized ^{3}He experiments use targets with pressures on the order of 10 atmospheres. These targets are difficult to achieve using the technique of metastable state optical pumping.

1.3.2 Spin-exchange Optical Pumping with Alkali Metal Vapor

The majority of spin-polarized neutron scattering experiments use a technique called spin-exchange optical pumping, to produce high density hyperpolarized ^{3}He in large amounts, which is the focus of this thesis work. In the process of spin-exchange optical pumping, the valence electrons in alkali metal atoms are polarized by optical pumping with circularly polarized laser light. Then, the polarization of the electrons is transferred to the ^{3}He nuclei by spin-exchange collisions [13].

Since spin-exchange collisions occur between different alkali metal atoms and the ^{3}He nucleus, the interaction cross section is much smaller compared to the hyperfine interaction cross section in the metastable pumping technique. This disadvantage is surpassed by the fact that high densities of alkali metal atoms can be easily optically pumped with high power lasers at the alkali metal atom's D1 lines. Today, in the lab, it is routine to polarize $\sim$ 100 cm^3 of ^{3}He nuclei in several tens of hours to polarizations near 50% by spin-exchange optical pumping with rubidium vapor.

1.4 Motivation and Goals

1.4.1 Background

The technique of spin-exchange optical pumping ^{3}He by alkali metal vapors was developed in the 1980s [25, 27, 35, 46] and applied to polarized electron scattering experiments in the 1990s [33, 40, 43]. Although researchers have been able to build polarized ^{3}He targets with optically pumped rubidium vapor in these experiments, such systems have yet to be optimized. In particular, the target polarization relaxation rates usually vary from cell to cell.

In the process of spin-exchange optical pumping, the detailed time evolution and the final ^{3}He polarization are determined by the physical processes of spin-related collisions among ^{3}He and alkali metal atoms, including the mechanism of optical pumping alkali metal electrons by laser photons and the various spin relaxation mechanisms for both the ^{3}He and the alkali metal atoms. Hence, to optimize such systems, thorough theoretical studies are needed. Measurements of the important rate constants are desirable. Before this thesis work, the experimental values of the key rates in the spin-exchange collisions for potassium-^{3}He pair and cesium-^{3}He pair have not been measured.

Theoretically, all alkali metal vapors can be used to spin-exchange optically pump ^{3}He. However, most of the past efforts were dedicated to rubidium vapor studies, since laser light sources at the rubidium D1 line were readily available. Nevertheless, the laser technology developed quickly, and the diode laser light for potassium and cesium D1 lines are now presently available. Today, the lack of light sources cannot justify rubidium as the sole candidate for spin-exchange optical pumping of ^{3}He. In fact, theoretical studies predict that the potassium-^{3}He pair has a higher efficiency than the rubidium-^{3}He pair in spin-exchange optical pumping [41]. Experimental investigations on the possibilities to build a better polarized ^{3}He target with potassium vapor could be beneficial to the field.

1.4.2 Goals

Following the discussions in the last section, the goals of this thesis work are mainly composed of three parts. (1). Developing a system to build good polarized ^{3}He targets, i.e., slow ^{3}He polarization relaxation rates and highly polarized ^{3}He cells. (2). Systematically measuring the spin-exchange cross sections of potassium-^{3}He, rubidium-^{3}He and cesium-^{3}He pairs. (3). Exploring the performance of polarized ^{3}He targets using potassium vapor.

The second chapter of this thesis provides a brief review of the theory of spin-exchange optical pumping, followed by a discussion of possible advantages of potassium over rubidium in polarizing ^{3}He. Estimates of the related rate constants are also presented.

The third chapter describes the lab system used for the polarized ^{3}He experiments, including the design and fabrications of the ^{3}He target cells, the construction of the gas system, the laser system and the target station. With this setup, we have been able to build long lifetime ^{3}He target cells consistently.

In Chapters 4 and 5, measurements of spin-exchange rate coefficients of potassium-^{3}He, rubidium-^{3}He and cesium-^{3}He pairs are presented. Chapter 5 also reports on the first production of a highly polarized ^{3}He target cell using potassium vapor. The results indicate that one can polarize ^{3}He with a higher efficiency compared to using rubidium vapor. Significantly less laser power is required to polarize an equivalent volume of ^{3}He gas.

Finally, the concluding chapter summarizes the results and discusses possible future applications.

Chapter 2

Spin-Exchange Optical Pumping

In this chapter, the physical processes of spin-exchange optical pumping are described and the related theories are reviewed. In the first section, the two underlying processes, optical pumping of alkali metal atoms and spin-exchange collisions between alkali metal atoms and ^{3}He atoms, are examined. The optical pumping rates and spin exchange rates are also estimated. Then, in the second and third sections, the ^{3}He polarization relaxations and ^{3}He polarization evolutions are discussed. The motivation of polarizing ^{3}He using potassium is discussed at the end of the chapter.

2.1 Theory of Spin-Exchange Optical Pumping

2.1.1 Optical Pumping of Alkali Metal Atoms

The ground state of the valence electron in alkali metal atoms is $^2S_{1/2}$, with angular momentum $J = 1/2$. In a magnetic field B, the populations of magnetic sub-states $m_J = \pm 1/2$ obey the normal Boltzmann distribution at the ambient temperature at thermal equilibrium. Taking room temperature $T \sim 300$ K and the magnetic field $B \sim 30$ Gauss, the population difference between the two sub-states is in the ratio of

$\exp(2\,\mu_e B/k_B T) \sim 1.00001$. The magnetic sub-levels are almost equally occupied.

To polarize the electron spins into one direction along the magnetic field, one needs to deplete one of the sub-levels and put all the electrons into the other sub-level. The depopulation optical pumping method was introduced in the 1950's [6] to achieve this goal.

In the depopulation optical pumping process, the atoms are illuminated with circularly polarized light. Suppose the helicity of the light is positive (σ^+), the wavelength of the light is tuned to the absorption line between the ground state $^2S_{1/2}$ and the excite state $^2P_{1/2}$ (D_1 line), then according to the angular momentum selection rule $\Delta m_J = +1$, only the electrons in the ground state $^2S_{1/2}, m_J = -1/2$ can absorb photons and be excited to the state $^2P_{1/2}, m_J = +1/2$. The electron population in $^2S_{1/2}, m_J = +1/2$ remains untouched. The excited electrons then decay to both ground states $^2S_{1/2}, m_J = \pm 1/2$, resulting in a net population transfer from the state $^2S_{1/2}, m_J = -1/2$ to the state $^2S_{1/2}, m_J = +1/2$.

Figure 2.1 shows a diagram of the relevant optical pumping scheme with the corresponding energy levels for an alkali metal atom. The branching ratios in Figure 2.1 indicate that the radiative decay to the $m_J = -1/2$ ground states is more favorable. On average, $1\frac{1}{2}$ photons are needed to polarize one unpolarized alkali metal atom. To speed up the polarization buildup process, usually ~ 100 torr of buffer gas, N_2, is introduced. Since the atom's spin angular momentum can transfer to the N_2 molecule rotational momentum via collisions, the sum of the angular momentum of the atoms and photons are not conserved in the presence of the N_2 buffer gas. Therefore, radia-

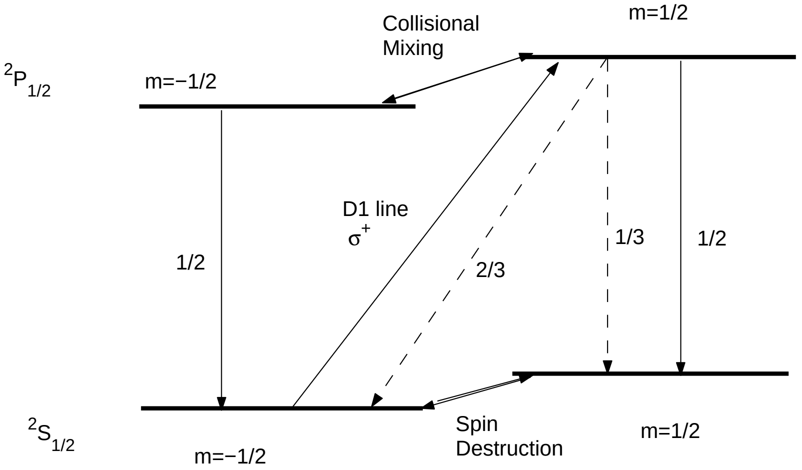

Figure 2.1: The energy level of an alkali metal atoms with D1 line optical pumping. The branching ratios 2/3,1/3 are for the case of spontaneous decays, which arise from the related C-G coefficient $< \frac{1}{2}\frac{1}{2}|\frac{1}{2}-\frac{1}{2}11 >= \sqrt{\frac{2}{3}}$ and $< \frac{1}{2}\frac{1}{2}|\frac{1}{2}\frac{1}{2}11 >= \sqrt{\frac{1}{3}}$. The number 1/2, 1/2 are for the case of collisional decays in the presence of a buffer gas.

tive branching ratios are not applied in this case. In addition, the collisions between the ^{3}He gas and the alkali metal atoms also mix the $^2P_{1/2}, m_J = \pm 1/2$ states. Overall, these collisions quench the atoms to the two ground state sub-levels with equal probability, resulting in a situation in which only one photon on average polarizes an alkali metal atom.

The optical pumping rate per unpolarized alkali metal atom γ_{opt} is determined by the incident light flux and the photon absorption cross section:

$$\gamma_{opt} = \int \frac{I(\nu)}{h\nu}\sigma(\nu)d\nu, \tag{2.1}$$

where $I(\nu)$ is the incident light spectral density in units of Watts cm^{-2} Hz^{-1}, and

$\sigma(\nu)$ is the photon absorption cross section with a Lorentzian profile

$$\sigma(\nu) = \frac{\sigma_0}{1 + 4(\nu - \nu_0)/\Gamma^2}. \tag{2.2}$$

The linewidth Γ in the above equation is dominated by pressure broadening (18GHz/atm for ^{3}He) while the alkali metal D1 lines natural widths are in the range of $\sim$10 MHz to $\sim$ 100 MHz.

The peak absorption cross section σ_0 per unpolarized alkali metal atom can be estimated by considering light scattering by a classical dipole oscillator. The incident light energy absorbed by a bound electron is (section 13.2 in [2])[1]

$$E = \pi \frac{e^2}{m} |E_0(\omega_0)|^2. \tag{2.3}$$

Dividing the energy by the the incident flux $I(\omega) \sim I(\omega_0) = (c/2\pi)|E_0(\omega_0)|^2$, we get the peak absorption cross section from the expression

$$\int \sigma(\nu) d\nu = \int \sigma(\omega) \frac{d\omega}{2\pi} \sim \Gamma \sigma(\nu_0) \sim \frac{E}{I(\omega_0)} = \pi \frac{e^2}{mc} = 8.46 \times 10^{-3}, \tag{2.4}$$

where we assume both the cross section and the incident light are peaked at ν_0. For $\Gamma \sim 20$ GHz, $\sigma(\nu_0) \sim 10^{-13}$ cm^2.

The peak cross section can also be calculated by time-dependent perturbation

---

[1] gaussian units and $\omega = 2\pi\nu$

theory. Using a quantum mechanical treatment [1], the sum rule becomes

$$\int \sigma(\nu) d\nu = \pi r_e c f, \tag{2.5}$$

where $r_e = e^2/mc$ is the classical electron radius and f is the oscillator strength, a dimensionless number on the order of one for alkali metal atoms ($f \approx 1/3$ for the $D1$ line and $f \approx 2/3$ for the $D2$ line [1]).

Equation 2.5 is only different from Equation 2.4 by a factor of f, which indicates that the optical pumping rates per atom (γ_{opt}) for different alkali metal atoms are the same order of magnitude, given the same incident light profile. Combining Equation 2.1 and Equation 2.5, one can see that γ_{opt} is proportional to the light power per unit area and inversely proportional to the absorption cross section linewidth Γ (i.e., the target cell's pressure).

In our experiments, the laser light power is 5 Watts, and the wavelength is ~ 770 nm (potassium D1 line). The target cell diameter is about 4 cm. According to Equation 2.1, the optical pumping time scale is approximately,

$$\begin{aligned} \gamma_{opt} &\sim \frac{5\text{watts}/(2\text{cm})^2}{6.63 \times 10^{-34}\text{m}^2\text{kg/sec} \times 3 \times 10^8\text{m/sec}/(770 \times 10^{-9}\text{m})} \times 10^{-13}\text{cm}^2 \\ &\sim 5 \times 10^5 \text{ sec}^{-1}. \end{aligned} \tag{2.6}$$

Note that the incident laser light power will decrease along the optical path, and the alkali metal atom spin destruction rates are not counted in the above estimate. Actually, the alkali metal atom spin destruction cross sections are smaller than the photon absorption cross section [32]. Equation 2.6 is a reasonable order of magnitude estimate.

The polarized alkali metal atoms lose their polarization by collisions with other atoms. During collisions, the electron spin can either transfer its angular momentum to the rotational angular momentum of the colliding pairs, or exchange its spin with the ^{3}He nuclear spin. The interaction Hamiltonian can be expressed as

$$H = H_{SR} + H_{SE} = \gamma(R) S \cdot N + A_b(R) S \cdot I, \tag{2.7}$$

where S is the electron spin, N is the rotational angular momentum and I is the ^{3}He nuclear spin. The coupling constants $\gamma(R)$ and $A_b(R)$ are functions of position and the corresponding wave function densities of the pairs. Given Equation 2.7, the electron spin flip cross section σ_{flip} can be calculated. The electron spin destruction cross section σ_{SD} is $2\sigma_{flip}$.

In practice, the total electron spin destruction rate of alkali metal atoms Γ_{SD} arises mainly through collisions with ^{3}He, buffer gas N$_2$ and alkali metal atoms themselves. Γ_{SD} is in the form

$$\begin{aligned} \Gamma_{SD} = (< \sigma_{SD}^{A-He} v_{He} > + < \sigma_{SE}^{A-He} v_{He} >)[^3He] \\ + < \sigma_{SD}^{A-A} v_A > [A] + < \sigma_{SD}^{A-N_2} v_{N_2} > [N_2] \end{aligned} \tag{2.8}$$

where A stands for alkali metal atoms, [ ] is the density, and <> denotes the thermal average, since the spin destruction cross sections are usually temperature dependent.

Due to the low buffer gas pressure, the last term in Equation 2.8 is smaller and less important than the first two terms.

Defining the rate constants $k_{A-i} =< \sigma^{A-i} v_i >$ for atom species i, the constants k_{A-i} are the key rates that finally determine the efficiency for optical pumping. Table 2.1 shows the theoretical estimates and experimental measurements of the velocity-averaged spin destruction cross sections for A-A pairs and A-^{3}He pairs, which indicate that

$$k_{K-K} < k_{Rb-Rb} < k_{Cs-Cs} \tag{2.9}$$

and

$$k_{K-He} < k_{Rb-He} < k_{Cs-He}. \tag{2.10}$$

Therefore, in a target cell filled with ^{3}He, optical pumping potassium will likely require less incident laser power among the choices of rubidium, potassium and cesium.

The fact that lighter alkali metal atoms have smaller spin destruction rates comes from the Hamiltonian in Equation 2.7. The coefficient $\gamma(R)$ in Equation 2.7 is proportional to the spin-orbit splitting of the alkali metal atom and inversely proportional to the reduced mass of alkali metal atom-^{3}He pair. Therefore, it decreases rapidly from Cs to Na [41].

Based on the values in Table 2.1, one can estimate the spin destruction rate for a typical cell in the lab with a ^{3}He density of 2×10^{19} cm^{-3} (pressure $\sim$ 1 atm) and a potassium density of $\sim 10^{14}$ cm^{-3} (temperature $\sim$ 171°C):

Atom pair	Ref.	Measured $\sigma_{SD}(\text{cm}^2)$	Ref.	Theory $\sigma_{SD}(\text{cm}^2)$
K-K	[47]	1.0×10^{-18}		
Rb-Rb	[29]	1.6×10^{-17}		
Cs-Cs	[48]	2.3×10^{-16}		
Na-^{3}He	[19]	1.4×10^{-25}	[42]	1.2×10^{-26}
K-^{3}He			[42]	6.5×10^{-25}
Rb-^{3}He	[35]	1.3×10^{-23}	[42]	7.5×10^{-24}
Cs-^{3}He			[42]	6.0×10^{-23}

Table 2.1: Measured values and theoretical estimates of spin destruction cross sections for alkali metal pairs and alkali metal-^{3}He pairs. The spin destruction cross sections decrease for smaller alkali metal atoms.

$$\Gamma_{SD} \sim 4_{(K-He)}\ \text{sec}^{-1} + 20_{(K-K)}\ \text{sec}^{-1} = 24\ \text{sec}^{-1}. \tag{2.11}$$

Equation 2.11 implies that potassium-potassium collisions are the main underlying processes responsible for the potassium spin destruction rate for the above experimental conditions.

The spin-exchange rate constants $k_{SE} =< \sigma_{SE}^{A-He} v_{He} >$ are much smaller than corresponding spin destruction rate constants k_{A-He} for ^{3}He atoms and alkali metal atoms. They both contribute little to the overall spin destruction of alkali metal atoms, but they are key factors in the process of ^{3}He nuclear spin polarization buildup. In subsequent chapters, these two rate constants will be discussed in more detail, and the measurement results for the spin-exchange rate constants will be presented.

With the relevant rate constants defined, it is possible to write down the alkali metal electron spin evolution equation for optical pumping. Introducing normalized ground state populations $N_{\pm}$ that satisfy $N_{+} + N_{-} = 1$, the alkali metal atom spin polarization is defined as twice the averaged spin:

$$P = 2 < S_z >= N_+ - N_-. \tag{2.12}$$

According to the definitions of γ_{opt} and Γ_{SD}, the rate equations are

$$\begin{aligned} \frac{dN_+}{dt} &= -\frac{dN_-}{dt} \qquad (2.13) \\ \frac{dN_+}{dt} &= \frac{1}{2}(2\gamma_{opt})N_- + \frac{\Gamma_{SD}}{2}N_- - \frac{\Gamma_{SD}}{2}N_+, \qquad (2.14) \end{aligned}$$

where the factor 1/2 in the first term of the rightside comes from the branching ratios of non-radiative quenching decay shown in Figure 2.1. Also, note that γ_{opt} is defined per unpolarized atom, which is half of the rate per atom in the sub-state $m_J = -1/2$.

From Equation 2.14, it is straightforward to show that for unpolarized atoms, the polarization evolves as

$$P(t) = P_0(1 - e^{-(\gamma_{opt}+\Gamma_{SD})t}). \tag{2.15}$$

After a time period $\sim (\gamma_{opt} + \Gamma_{SD})^{-1} \sim \gamma_{opt}^{-1} \sim 10$ microsecond, (comparing Equation 2.11 and Equation 2.6), the electron spin polarization arrives at its maximum steady value

$$P_0 = \frac{\gamma_{opt}}{\gamma_{opt} + \Gamma_{SD}}. \tag{2.16}$$

All the above discussions including the rate constant values in Table 2.1 ignore the effect of the non-zero nuclear spin of the alkali metal atoms. Basically, a non-zero nuclear spin slows down the optical pumping rate comparing to the zero nuclear spin case. The following discussions will show that this effect can be described by a slow down factor multiplied by the rate constants. Actually, this factor is the ratio of the averaged hyperfine polarization to the electron spin polarization for the alkali metal atoms.

In a weak magnetic field, since the zeeman splitting($\Delta m = 1$) is only on the order of 10^3 kHz/Gauss and the hyperfine splitting ($\Delta F = 1$) is $\sim$ GHz, the total spin $F = I + S$ is a good quantum number instead of S. The electron ground state has $2(2I+1)$ m_F sub-levels instead of only $2S+1 = 2$ sub-levels as shown in Figure 2.1. In the presence of a high-pressure ^{3}He gas, the hyperfine structures are not resolved within the pressure broadened absorption D1 line. The m_F sub-levels absorb the incident light with equal probability. The buffer gas will still quench the excited states to the ground sub-level with equal branching ratios. The only difference from the scheme in Figure 2.1 is now that it takes more steps to transfer the electrons to the righthand ground sub-level $m_F = I + \frac{1}{2}$. Therefore, the optical pumping rate gets slower compared to the zero nuclear spin situation discussed before.

The collisions between alkali metal atoms thermally mix the m_F sub-levels according to their energies in a weak magnetic field. The steady state m_F sublevel population can, therefore, be described by a spin temperature β^{-1} with Boltzmann distribution [7, 46]

$$N_m = \frac{1}{Z_F} e^{\beta m}, \tag{2.17}$$

where

$$Z_F = \Sigma e^{\beta m} = \frac{\sinh[\beta(F + 1/2)]}{\sinh(\beta/2)}. \tag{2.18}$$

The averaged alkali metal's hyperfine polarization for state F is

$$P_F = \frac{\Sigma m N_m}{\Sigma N_m} = \frac{1}{Z_F}\frac{\partial Z_F}{\partial \beta}. \tag{2.19}$$

In the presence of optical pumping laser light, the spin temperature β^{-1} is a function of the laser power. It is determined by requiring the averaged electron spin polarization change from Equation 2.12 to

$$P_S = \tanh\frac{\beta}{2} = 2 < S_z > . \tag{2.20}$$

It can be shown that under the spin temperature limit [32], the polarization evolution will slow down by a factor of $S = P_F/P_S$. As a result, Equation 2.15 becomes

$$P(t) = P_0(1 - e^{-\frac{\gamma_{opt}+\Gamma_{SD}}{S}t}), \tag{2.21}$$

where the final polarization P_0 is unchanged. Therefore, in our experiments, the alkali metal atom's electron spin polarization is established on a time scale of milliseconds, rather than the simplified estimate of $\sim 10^{-5}$ seconds from Equation 2.15.

The slowdown factor S can be understood as a requirement coming from angular momentum conservation. For simplicity, first consider the case without relaxation. Since the optical pumping rate is proportional to the unpolarized alkali metal electron population, the rate is proportional to a factor of $1 - P_S$, even in the presence of non-zero nuclear spins. Given the fact that each photon transfers $\hbar/2$ angular momentum to the atom's total hyperfine spin P_F, the rate equation for the atom's hyperfine spin P_F can be written as

$$\frac{dP_F}{dt} = \gamma_{opt}(1 - P_S)/2. \tag{2.22}$$

Therefore, the rate equation for the electron spin P_S becomes

$$\frac{dP_S}{dt} = \frac{d(P_F/S)}{dt} \simeq \frac{\gamma_{opt}}{S}(1 - P_S)/2. \tag{2.23}$$

Compared to Equation 2.14, the slowdown factor S arises naturally. The argument is the same for the case of the relaxation rate Γ_{SD}. Note that since $S = P_F/P_S$ is time dependent, the electron spin $P(t)$ does not increase exponentially. Only when $P(t)$ is small, $\frac{\gamma_{opt}+\Gamma_{SD}}{S}$ is approximately a constant.

In our experimental conditions, the target cells usually contain large amount of alkali metal vapor ($[A] \sim 10^{14}$ cm^{-3}). The incident light flux is not a constant along the light path through the cell (i.e., we are dealing with optically thick targets). In such situations, the incident flux $I(\nu) = I(\nu, z)$ is a function of position, hence $\gamma_{opt} = \gamma_{opt}(z)$. The consequence is that the alkali metal polarization $P = P(z)$ also varies along the cell. To determine $P(z)$, one has to solve the following equations,

$$\begin{aligned}
\frac{\partial I(\nu, z)}{\partial z} &= -[A]\sigma(\nu)[1 - P(z)]I(\nu, z) && (2.24)\\
\gamma_{opt}(z) &= \int \frac{I(\nu, z)}{h\nu}\sigma(\nu)d\nu && (2.25)\\
P(z) &= \frac{\gamma_{opt}(z)}{\gamma_{opt}(z) + \Gamma_{SD}}. && (2.26)
\end{aligned}$$

A mathematica code has been written to solve numerically the above equation arrays for given laser light powers/linewidths and alkali metal vapor densities. Although the calculation does not agree well with experimental measurements, due to large uncertainties on Γ_{SD} and $[A]$, it still shows one important aspect of optically thick pumping, the absorption length in the vapor is on the order of $\sim$ mm.

The laser incident light can travel along the cell beyond many absorption lengths for a optically thick cell. Since $\gamma_{opt} >> \Gamma_{SD}$, at the front of the vapor ($z \simeq 0$), the alkali metal polarization will be saturated and near one. Then, the saturated vapor cannot absorb more laser light. After passing the saturated vapor region, the incident light with the remaining power will continue to propagate along the path and saturate more alkali metal atoms. When all the laser power has been absorbed, the alkali metal polarization reduces to zero abruptly within one absorption length. So the cell is basically divided into two parts. The front part has an alkali metal polarization near one, and the rear part has a polarization near zero.

Collisions between the alkali metal atoms and the container's wall also relax the electron polarization in addition to the Γ_{SD} destruction. For the high-pressure cells in our experiments, this effect can be modeled as a polarization diffusion process near the wall [45]. Let D denote the alkali metal atom diffusion coefficient in the cell. Adding a diffusion term $D\nabla^2 P$ to Equation 2.21, the polarization evolution equation is

$$\frac{\partial P}{\partial t} = -\frac{\Gamma_{SD}}{S} P + D\nabla^2 P. \tag{2.27}$$

The diffusion term adds to the spin destruction rate by approximately $\sqrt{\frac{D}{\pi r^2 (\Gamma_{SD}/S)^{-1}}}$

[45]. For our ~ 1 atmosphere potassium-^{3}He cells, this effect is less than 5% of Γ_{SD}/S.

2.1.2 Spin-exchange Collisions

Spin-exchange collisions between alkali metal and noble gas ^{3}He atoms can be understood as interactions between two magnetic moments. The alkali metal atom's valence electron carries an electronic magnetic moment $\mu_s = 2\mu_B S$, where $\mu_B = \frac{e\hbar}{2m_e}$ is the Bohr magneton, and the ^{3}He nucleus carries a nuclear magnetic moment $\mu_I = \gamma_n I$. The parameter γ_n is the nuclear gyromagnetic ratio and

$$\gamma_n = \mu_I/I = g(\frac{e\hbar}{2m_p})I/I = g(\frac{e\hbar}{2m_p}) \equiv g\mu_N, \tag{2.28}$$

where $\mu_N = \frac{e\hbar}{2m_p}$ is the nuclear magneton and g is the g factor for nucleus I. For ^{3}He, $\gamma_{3_{He}} = 3243$ Hz/Gauss and for proton, $\gamma_p = 4258$ Hz/Gauss.

The spin-exchange Hamiltonian between two magnetic moments is [2]

$$H = -\frac{8\pi}{3}\boldsymbol{\mu}_s \cdot \boldsymbol{\mu}_I \delta(\boldsymbol{r}) + \frac{1}{r^3}\left[\boldsymbol{\mu}_s \cdot \boldsymbol{\mu}_I - 3\frac{(\boldsymbol{r}\cdot\boldsymbol{\mu}_s)(\boldsymbol{r}\cdot\boldsymbol{\mu}_I)}{r^2}\right], \tag{2.29}$$

where the first term describes the interaction at $\mathbf{r}$=0, which dominates the spin-exchange process. This expression was first introduced by Fermi and called the Fermi contact interaction energy.

Starting from Equation 2.29, it is natural to write down the spin-exchange Hamiltonian using quantum theory,

$$H_{ex} = A_b(R)\boldsymbol{I}\cdot\boldsymbol{S} = \frac{16\pi}{3}\mu_B\gamma_n\eta^2|\phi_e(R)|^2\boldsymbol{I}\cdot\boldsymbol{S}. \tag{2.30}$$

In Equation 2.30, R is the distance from the ^{3}He nucleus to the alkali metal atom center, and $\phi_e(R)$ is the unperturbed electron wave function for the alkali metal without ^{3}He present. The parameter η can be understood as an enhancement factor [13]. In the presence of ^{3}He nucleus, the Coulomb potential attracts the alkali metal electron to the ^{3}He nucleus, which increases the probability that the electron is located at the ^{3}He nucleus. The enhancement parameter η was calculated by Walker and collaborators in the 1980's [24].

Based on the Hamiltonian in Equation 2.30, the spin-exchange cross section σ_{SE} can be estimated by time-dependent perturbation theory. An order of magnitude estimate for σ_{SE} can be obtained as follows. Taking $R \sim r_A$ as the radius of an alkali metal atom (classically, it is the nearest distance between an alkali metal atom and the ^{3}He nucleus), and the collision interaction time as $\Delta t \sim r_A/v_{He}$, where $v_{He} = \sqrt{8kT/\pi m_{He}}$ is the thermal velocity of ^{3}He atoms, we can estimate σ_{SE} as,

$$\begin{aligned}\sigma_{SE} &= \pi r_A^2 \cdot 2\left|\frac{<\uparrow\downarrow|H(r_A)\Delta t|\downarrow\uparrow>}{\hbar}\right|^2 \\ &= 2\pi r_A^2\frac{A_b^2(r_A)\Delta^2 t}{4\hbar^2}.\end{aligned} \tag{2.31}$$

Correspondingly, the spin-exchange rate is

$$\gamma_{SE} = [A] \cdot v_{He} \cdot \sigma_{SE}. \tag{2.32}$$

According to the above equations, the spin-exchange cross section σ_{SE} is inversely proportional to the square of the ^{3}He thermal velocity. Therefore, we expect the cross section is inversely proportional to the temperature T. The rate coefficient

$$k_{SE} \equiv < v_{He} \cdot \sigma_{SE} > \tag{2.33}$$

should exhibit $1/\sqrt{T}$ dependence.

Equation 2.31 also suggests a positive correlation between the alkali metal atom size and the spin-exchange cross section. Table 2.2 shows the theoretical estimates of spin-exchange cross sections for alkali metal-^{3}He pairs derived by Walker and Happer [28].

Atom pair	Na-^{3}He	K-^{3}He	Rb-^{3}He	Cs-^{3}He
$\sigma_{SE}(10^{-24}cm^2)$	1.2	2.1	2.1	2.7

Table 2.2: Theoretical estimates for the spin-exchange cross sections at a temperature of 100 °C for alkali metal-^{3}He pairs from Reference [28].

At a temperature $\sim$ 150 °C, the ^{3}He thermal velocity is about 1700 m/s, and the potassium vapor density is on the order of 10^{14} cm^{-3}. The spin-exchange rate constant is estimated as $k_{SE} \sim 3.6 \times 10^{-19}$cm^3/s, which implies that the ^{3}He spin polarization rate is about $\sim$ (a few hours)$^{-1}$.

The theoretical spin-exchange cross sections for rubidium-^{3}He and potassium-^{3}He pairs are almost the same, since the radii for rubidium and potassium are similar. However, the spin destruction cross section for the rubidium-^{3}He pair is ten times larger than for the potassium-^{3}He pair due to spin rotation interactions, as shown in Table 2.1. So, we expect an overall higher spin-exchange efficiency for the potassium-^{3}He pair.

The spin-exchange photon efficiency η is defined as the inverse of the minimum photon number needed to fully polarize one unpolarized ^{3}He nucleus [45]. The efficiency is determined by the ratio of the spin-exchange rate of the alkali metal atom ^{3}He pair to the overall alkali metal electron's spin destruction rate, Γ_{SD}. Since each photon transfers $\hbar/2$ angular momentum to the alkali metal atom's electron, by definition, we have

$$\begin{aligned} \frac{1}{2}\eta^{-1} &= \frac{\Gamma_{SD} + k_{SE}[^3He]}{k_{SE}[^3He]} \\ \Longrightarrow \eta &= \frac{k_{SE}[^3He]}{2(\Gamma_{SD} + k_{SE}[^3He])}. \end{aligned} \tag{2.34}$$

Inserting the rate constant values from Table 2.1 and Table 2.2 into the above equation, the maximum spin-exchange photon efficiencies of alkali metal atom and ^{3}He pairs can be estimated and are given in Table 2.3.

Table 2.3 indicates the optimum specifies for polarizing ^{3}He. They are Na and K, in terms of power consumption for optical pumping laser light. Although the prediction is straightforward, one has to bear in mind that the actual photon efficiencies could be very different from the values listed in Table 2.3. In practice, at

Atom pair	Na-^{3}He	K-^{3}He	Rb-^{3}He	Cs-^{3}He
$2\eta_M = \sigma_{SE}/(\sigma_{SD} + \sigma_{SE})$	0.9	0.4	0.03	0.008

Table 2.3: Theoretical maximum spin-exchange photon efficiencies for the limit of low alkali metal densities. Spin destruction is mainly due to the rotation interaction of the alkali metal and ^{3}He atom pairs, ignoring the contribution from collisions between alkali metal atoms.

high temperature, the spin collisions between alkali metal atoms could dominate the spin destruction processes, hence the photon efficiency can be strongly temperature-dependent. What's more, systematic measurements for σ_{SD} and σ_{SE} are lacking in the literature, and it is possible that the differences between experimental values and theoretical estimates are large.

2.2 ^{3}He Spin Relaxation Studies

The ^{3}He nuclei gain polarization from spin-exchange collisions with polarized alkali metal atoms and lose polarization through various relaxation processes.

The fundamental physical process which ultimately limits the ^{3}He spin relaxation rate is the magnetic dipole-dipole interaction between ^{3}He atoms [34]. During collisions between ^{3}He atoms, the magnetic dipole-dipole interaction couples the ^{3}He nuclear spins to the orbital angular momentum of the colliding atom pair. Therefore, the individual ^{3}He nuclear spins are depolarized.

Newbury *et al.* calculated the relaxation rate Γ_{bulk} due to ^{3}He dipole-dipole interactions in Reference [34]. It was found that the dipolar relaxation is proportional to the ^{3}He density. At room temperature (23 °C),

$$\Gamma_{bulk} = \frac{[^3\text{He}]}{744}\ \text{hours}^{-1}, \tag{2.35}$$

where [^{3}He] is the ^{3}He density in units of amagats. (An amagat is the ideal gas density at one atmosphere and 0 °C. One amagat=2.69×10^{19} cm^{-3}.) For the target cells with ^{3}He pressures ~ 1 atm, γ_{bulk}^{-1} is longer than 744 hours at room temperature.

Newbury *et al.* also predicted a moderate negative temperature dependence for Γ_{bulk}. In the temperature range of 23 °C to 250 °C, the calculated γ_{bulk} decreases by a factor of 1.2.

In practice, the wall collision is the most important process which dominate the ^{3}He polarization relaxation rate. In a ^{3}He glass cell, the ^{3}He atoms collide with paramagnetic impurities such as Fe^{3+} on the cell's surface. The Fe^{3+} in the glass wall have random orientations, leading to the ^{3}He nuclear spin relaxation. For glass which is highly permeable to ^{3}He , such as Pyrex, the wall relaxation rates can be as fast as ~ 1 hours^{-1}. Some aluminosilicate glasses, namely, Corning 1720 and GE-180, both have a low ^{3}He permeability, therefore, wall relaxation rates $\sim 1/50$ hours^{-1} are achievable.

The temperature dependence of wall relaxation rates was studied both experimentally and theoretically in References [15] and [76]. At low temperatures, the relaxation rate decreases with increasing temperature, since ^{3}He atoms spend less time at the wall at higher temperature [15]. For temperatures above 130 K, the wall sticking time is the most important, leading to a temperature dependence of

$$\Gamma_{wall} = \Gamma_w^0 e^{-E/kT}, \tag{2.36}$$

where E is the binding energy of the ^{3}He atom at the wall [35].

Saam *et al.* confirmed Equation 2.36 in experiments and empirically determined Γ_w^0 and E for Pyrex glass in Reference [76]. They found that

$$\begin{aligned} \Gamma_{wall} &= \Gamma_w^0 e^{-1.65/T} \\ &\simeq \Gamma_w^0 (1 - \frac{1.65}{T}). \end{aligned} \tag{2.37}$$

In the temperature range of 23 °C to 250 °C, Γ_{wall} can be regarded as a constant for Pyrex glass cell according to Equation 2.37. The constant Γ_w^0 is proportional to the surface-to-volume ratio of the cell. Therefore, the wall relaxation time $1/\Gamma_{wall}$ scales with the cell's characteristic length. Larger cells have longer life times.

In addition to the above two basic ^{3}He spin relaxation processes, there are other relaxation mechanisms that typically contribute less to the ^{3}He spin relaxation. The inhomogeneous magnetic field can relax the ^{3}He spin polarization via [26]

$$\Gamma_{\nabla B} = D_{He} \frac{|\nabla B_x|^2 + \nabla B_y|^2}{|B_z|^2}, \tag{2.38}$$

where D_{He} is the ^{3}He self-diffusion constant and the holding magnetic field is along the z direction. For a cell with one atmosphere of ^{3}He , D_{He} is ~ 0.03 cm^2/s. The

Helmholtz coils in our experiments have a residual magnetic field gradients near the center on the order of $\sim$ 10 mG/cm and the holding field B_z is between 20-40 G, so $\Gamma_{\nabla B}^{-1} \sim 1400$ hours, which is negligible.

In the polarized ^{3}He scattering experiments, electron beam ionization also contributes to the ^{3}He depolarization. This effect was small in SLAC experiment E-154 [44] and is absent in our experiments.

The total ^{3}He polarization relaxation rate is then given by

$$\Gamma = \Gamma_{wall} + \Gamma_{bulk} + \Gamma_{\nabla B} + \Gamma_{other}, \tag{2.39}$$

where the first term typically dominates. We have been successfully making cells with Γ^{-1} greater than 50 hours using GE-180 glass. High ^{3}He polarizations have been achieved in these long lifetime cells in our laboratory.

2.3 ^{3}He Polarization Evolution Equations

The ^{3}He nuclear polarization evolution has a similar form to the alkali metal atoms polarization evolution Equation 2.14. Let $N_\pm$ be the normalized atom state populations satisfying $N_+ + N_- = 1$. The ^{3}He spin polarization can be expressed as $P = N_+(^3He) - N_-(^3He)$. The alkali metal atom polarization is $P_A = N_+(A) - N_-(A)$. The ^{3}He polarization rate equation is given by

$$\frac{dN_+(^3He)}{dt} = \left[\frac{\Gamma}{2} + \gamma_{SE} N_+(A)\right] N_-(^3He) - \left[\frac{\Gamma}{2} + \gamma_{SE} N_-(A)\right] N_+(^3He), \tag{2.40}$$

where

$$\frac{dN_+(^3He)}{dt} + \frac{dN_-(^3He)}{dt} = 0. \tag{2.41}$$

The time evolution of Equation 2.40 for initially unpolarized ^{3}He is

$$P(t) = P_A \cdot \frac{\gamma_{SE}}{\gamma_{SE} + \Gamma}(1 - e^{-(\gamma_{SE}+\Gamma)t}), \tag{2.42}$$

with a time constant of $(\gamma_{SE} + \Gamma)^{-1}$.

The steady state ^{3}He polarization becomes

$$P = P_A \cdot \frac{\gamma_{SE}}{\gamma_{SE} + \Gamma} = \left(\frac{\gamma_{opt}}{\gamma_{opt} + \Gamma_{SD}}\right)\left(\frac{\gamma_{SE}}{\gamma_{SE} + \Gamma}\right). \tag{2.43}$$

According to Equation 2.43, to achieve a high ^{3}He polarization, both $P_A \simeq 1$ and $\gamma_{SE} \gg \Gamma$ have to be satisfied. So one wants the alkali metal atom density $[A]$ large enough to ensure $\gamma_{SE} = k_{SE}[A] \gg \Gamma$, but still small enough so that $\Gamma_{SD} \ll \gamma_{opt}$, and $P_A \simeq 1$.

Explicitly, the requirements for achieving a high ^{3}He polarization are

$$\Gamma_{SD} \ll \gamma_{opt}, \tag{2.44}$$

and

$$\Gamma \ll \gamma_{SE} = k_{SE}[A]. \tag{2.45}$$

These requirements can be rewritten as conditions on the alkali metal density (temperature),

$$\frac{\Gamma}{k_{SE}^{A-He}} \ll [A] \ll \frac{\gamma_{opt} - k_{SD}^{A-He}[^3He]}{k_{SD}^{A-A}}. \qquad (2.46)$$

Higher laser power and longer lifetime cells can increase the range of the above inequality. On the other hand, for a given incident laser power and cell, choosing the alkali metal-atom-^{3}He pair which has the largest spin-exchange rate (k_{SE}^{A-He}) and smallest spin destruction rate coefficients (k_{SD}^{A-A} and k_{SD}^{A-He}) should optimize the ^{3}He polarization system. This is the main motivation for this thesis work, to polarize ^{3}He using potassium and to measure the spin-exchange rate coefficients for the potassium-^{3}He pair and the cesium-^{3}He pair.

Chapter 3

Experimental Setup

3.1 Overview

This chapter describes the experimental setup. In the first part, the design and fabrications of the ^{3}He target cells are discussed. Following is a description of the gas system built to clean and fill the cells with ^{3}He and N_2 gases, after which the gases filling process is presented. In the second part of the chapter, the target setup components and operations are described, including the lasers and optics layout, the production and control of the magnetic fields, and the heating oven with temperature measurements.

3.2 Target Cells

In our spin-exchange optical pumping experiments, ^{3}He gas and alkali metals were sealed in glass cells. Figure 3.1 shows a photograph of a cell used in the experiments. During the experiments, the cells were heated to between 100 °C and 200 °C, and a laser beam passed through the cell to polarize the alkali metal vapor.

Figure 3.1: A double-chamber cell used in the experiments. The background is an optical table with threaded holes with one inch spacing.

3.2.1 Cell Design

To polarize ^{3}He successfully, it is required that the cell's geometry and the laser optics are both optimized to improve overall laser light transmission efficiency into the cell. More importantly, the cell's wall should have low ^{3}He polarization relaxation rates. The cell should also have a low permeability to ^{3}He to reduce diffusion loss of ^{3}He through the cell over longtime periods.

All the above requirements come into considerations in the cell design and fabrication. The key factors are designing the cell geometry and choosing the correct glass materials for building cells.

3.2.1.1 Geometry Considerations

As shown in Figure 3.1, double-cylinder-chamber cells were built for the experiments. In principle, a spherical geometry would be a good choice, since a spherical cell has a small surface to volume ratio. Hence, a longer wall relaxation rate could be achieved with a spherical cell as discussed in Chapter 2. However, light reflection and refraction on a curved cell surface does seriously reduce the light transmission efficiency. Therefore, a cylindrical shape was adopted. The front end of the cell was constructed to be flat, and the cell's diameter was chosen to match the laser beam profile to use the maximum amount of laser light.

The two-chamber design, shown in Figure 3.1, was first adopted for electron scattering experiments [36]. In the electron scattering experiments, the laser light illuminated the upper chamber of the target cells, while the electron beam passed through the bottom chamber. This design allowed a separation of the optical pumping from the electron beam scattering process and, therefore, helped reduce radiation damage to the optical mirrors during the experiments.

Another technical reason for choosing the double-chamber design in the experiments is to allow for ^{3}He polarization measurements at room temperature, similar to the water calibration measurements. A better measurement of the ^{3}He polarization is achieved than using a hot single-chamber cell. Polarimetry, along with the relevant calibrations, will be discussed in detail in the next chapter.

	GE-180	Fused Quartz	Corning-1720	Pyrex
Softening Point (°C)	1015	1870	926	821
Anneal Point (°C)	785	1140	726	565
Strain Point (°C)	735	1070	674	510
Expansion Coefficient (10^{-7}/°C)	44	55	44	33
Density (g/cm^3)	2.77	2.20	2.64	2.23

Table 3.1: Comparative data for GE-180, Quartz, Corning 1720 and Pyrex glass. Note that the glass density is proportional to the permeability of ^{3}He. All the data are taken from the GE Lighting glass data sheet.

3.2.1.2 Material Considerations

Besides the geometry considerations, it is important to choose the correct glass material when constructing the cells. As discussed in the last chapter, the glass surface properties, such as the impurities, the ^{3}He permeability are largely responsible for the ^{3}He depolarization. Different glasses make huge differences in the polarized ^{3}He wall relaxation rates.

Quartz, borosilicate glass (Pyrex) and aluminosilicate glass (Corning 1720, GE type 180) are the most common candidates for constructing ^{3}He cells. All of them have been used for building polarized ^{3}He cells in different labs. Table 3.1 shows a comparison of different glass, namely, glass GE-180, Quartz, Corning 1720 and Pyrex.

Quartz is more permeable to ^{3}He compared to Pyrex and aluminosilicate glass. It also has a much higher softening point (1870 °C) than the other two types of glass. Correspondingly, it is harder to work with than Pyrex glass in terms of glassblowing. Therefore, quartz was not used for cell construction in our lab.

Pyrex is easy to work with, so it is preferred by glassblowers. However, the pyrex cells made in our lab had fast wall relaxation rates typically with 1 hour^{-1}

timescales. Though it had been difficult to make long ^{3}He polarization relaxation time cells out of Pyrex throughout the history of spin-exchange optical pumping, it is worth mentioning that some recent successes have been made in other labs using Pyrex cells. In 2002, long lifetime ($\sim$ 40 hours) bare Pyrex ^{3}He cells were produced in Saam's lab [75]. Another method, namely, sol-gel coating of Rb and Cs metal in the inner wall, was explored in Cates' lab [57] to increase the wall relaxation time of Pyrex cells. Relaxation times of hundreds of hours have been observed in some Pyrex cells [57].

In the SLAC polarized ^{3}He experiments, the ^{3}He target cells were all made out of aluminosilicate glass Corning 1720 [44, 36]. Corning 1720 has a very low permeability to ^{3}He. The wall relaxation rates in Corning 1720 cells can easily be several tens hours^{-1} or less. However, some serious drawbacks for using Corning 1720 glass exist. First, it is extremely difficult to work with, actually only a very few glassblowers can work with this glass. Second, it is hard to get Corning 1720 glass on the market. The price of Corning 1720 glass is high and the availability is limited. Actually in 2003, Corning Inc. stopped its product line of aluminosilicate glass tubes including Corning 1720.

All the cells used in this work were produced out of a new aluminosilicate glass, namely, GE-180. Originally GE-180 glass was developed and was used exclusively for halogen lamps. It has a superior heat strength, which tolerates temperatures higher than 500°C with minimal levels of impurities. GE-180 glass has a higher density than other glasses (see Table 3.1), and therefore it has a lower permeability to ^{3}He.

In terms of physical properties, it is a good substitute for Corning 1720 glass. The results in our lab confirm that GE-180 glass is an ideal material for polarized ^{3}He cells. Bare cells made of Ge-180 glass in our lab consistently have wall relaxation times on the order of $\sim$50 hours. It is also worth noting that unlike Corning 1720 glass, Ge-180 glass is easy for a glassblower to use and is cheaper and available on the market.

3.2.2 Cell Fabrications

For the cell fabrication and filling procedures, it was difficult to achieve consistent control of the cell wall relaxation rates. Besides choosing the right glass material, careful glass cleaning treatments were applied to reduce any additional ^{3}He relaxation rates resulting from gas-glass surface interactions. One highlight of this thesis work is that, by the end, long wall relaxation time cells were produced routinely in the lab.

Commercial glass tubing has many contaminants on the surface. Untreated tubing does not make long lifetime cells. The key treatment of tubing during the cell fabrication procedure was to reblow the tubing so that the inner wall of the cell has a cleaner surface.

Original Ge-180 glass tubing out of box was 16 ± 0.2 mm in outside diameter with a wall thickness of 1.2 ± 0.12 mm. The tubing was attached to a lathe, and the glassblower carefully expanded it to a size of 1.5 inch or 1.0 inch in outer diameter, for the upper chamber tubing and bottom chamber tubing, respectively. Since a simple expansion leaves the new tubing wall too thin, and the cell too fragile, the glassblower had to increase the tubing diameter, then shrink it in length to thicken the wall. These procedures were repeated until the tubing reached the desired diameter for a certain wall thickness. The measured wall thickness after blowing was 0.9 ± 0.1 mm. In this case, a direct measurement of the wall thickness is necessary, since the wall thickness cannot be calculated by assuming the wall thickness is inversely proportional to the diameter.

Before resizing the tubing, additional chemical cleaning procedures are typically applied. The glass was rinsed in nitric acid, deionized water and spectroscopic grade methanol. However, for the cells made in our lab, simple reblowing without chemical treatment cleaned the glass effectively enough. Future cell lifetime improvements may be achieved if the acid cleaning step are added.

The cell chambers were made from the resized tubing. Then, one or two cells were connected to a tube through a 1 inch long constriction stem, as shown in Figure 3.2. The whole string was annealed in an oven at $\sim 785\,^\circ$C for several hours. After annealing, a capsule containing alkali metal was attached to one end of the tube. The other end of the tube served as an entrance of the entire cells manifold to the vacuum system. (see Figure 3.2).

3.3 Cell Filling

A vacuum system was built in our lab to fill the cells. The system has the capacity to handle a wide pressure range from 10^{-8} torr to several atmospheres. It was used to monitor the contaminants in the cell, pump out the contaminants from the cell, and

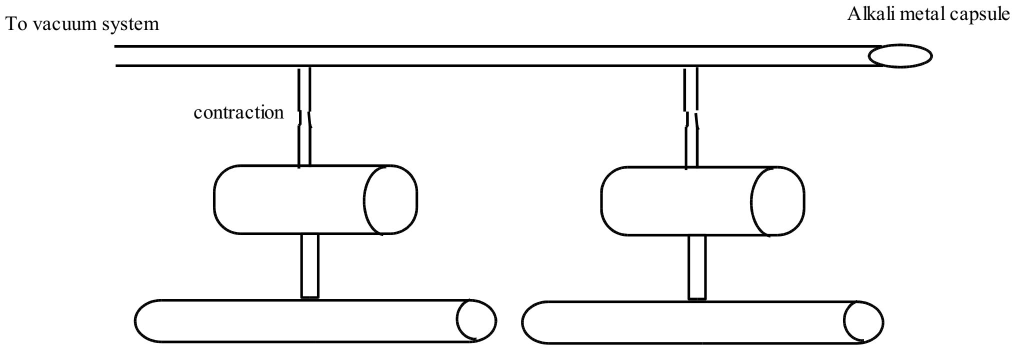

Figure 3.2: A string of cells on a manifold. The dimensions of the pumping chamber is 1.5 inches in diameter and 3 inches in length; the target chamber is 1 inch in diameter and 4 inches in length.

then fill the cell with the alkali metal vapor, and the ^{3}He and N_2 gas in a controlled manner.

3.3.1 Gas System

Figure 3.3 shows the layout of the vacuum system. It contains two pumps, one of which is a turbo molecular pump (Pfeiffer model TSH071E) and the other of which is an ion pump (Varian minivac model 9290091). Combining the two pumps can evacuate the system to a pressure down to 10^{-8} mbar. A residual gas analyzer (SRS model RGA 200) is attached to the vacuum manifold to identify and analyze the gas contaminants left in the system. Several pressure gauges are located in different positions to measure the system pressure.

It took one month in the lab to assemble and test the entire vacuum system. Before filling the cell, the system was leak tested with ^{4}He gas and baked for several

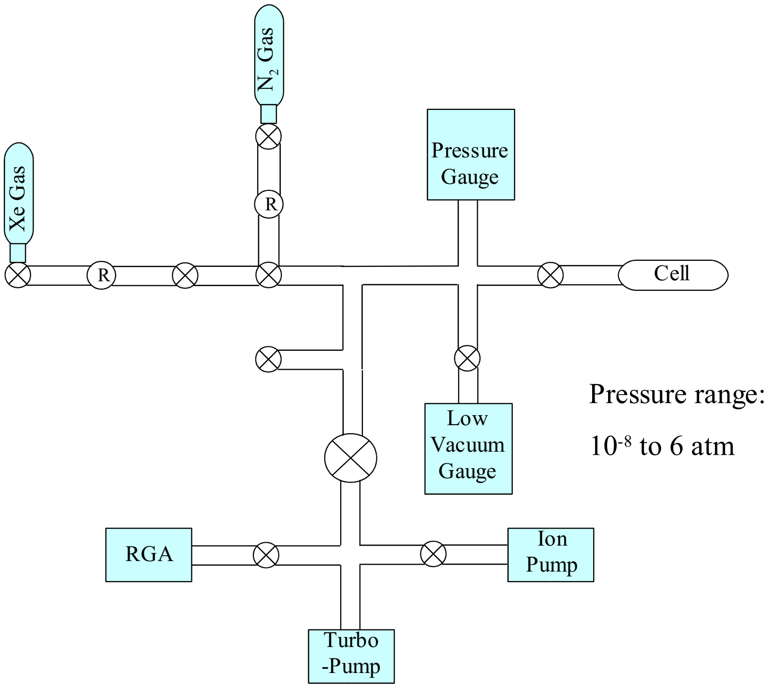

Figure 3.3: The vacuum system used for cell filling.

days to bring the pressure down to 10^{-8} mbar. One lesson learned in this process was that some valves in the system cannot stand high baking temperature.

Before attaching the cells to the vacuum, the string of cells was rinsed in deionized water, then sealed to a VCR fitting by epoxy. After 24 hours, when the epoxy fully dried, the string was connected to the vacuum system through a valve. The turbo molecular pump was turned on, until the the system pressure fell to ~ 1 torr, then the ion-pump was turned on. When the vacuum pressure was below 10^{-4} torr, the RGA was turned on to monitor the gas contaminants in the system. Figure 3.4 shows a typical RGA scan before baking the cell.

Initially the main contaminants in the system were water, nitrogen (air), CO_2 and hydrogen. To remove the contaminants, the cell string was wrapped with heating tape

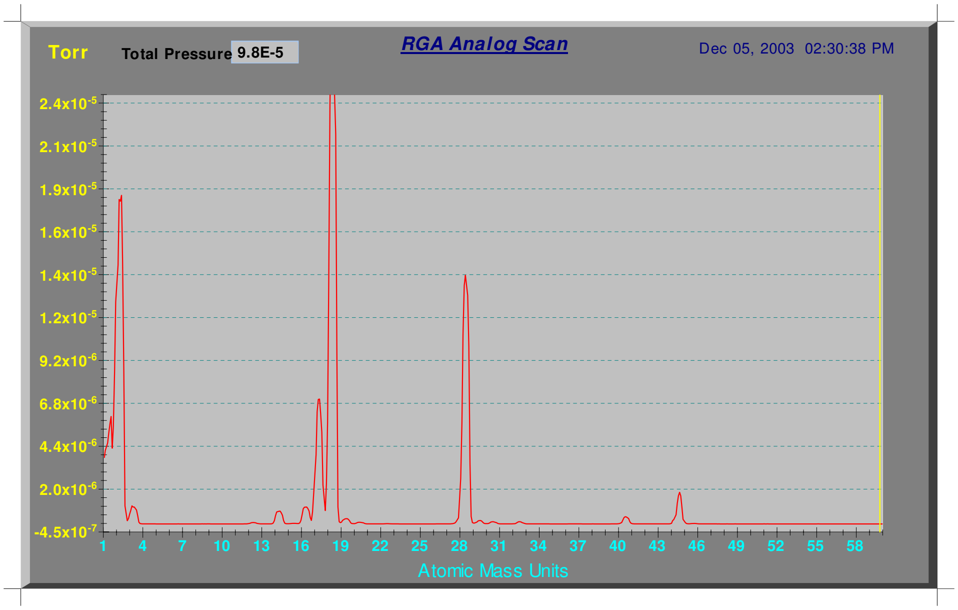

Figure 3.4: A typical RGA scan before baking the cell.

and baked at ∼ 150 °C overnight. Initially, large amounts of water were baked off the cell walls. The vacuum pressure would increase by an order of magnitude. After 12 hours or so, the pressure dropped to its minimum value, namely, $\sim 10^{-7}$ torr.

During the pump down, the pressure in the system was not uniform. Only after a very long time period did the whole system reach a pressure equilibrium. During most of the time, the pressure readings from different gauges had different values, since these gauges were located in different positions. As a consequence, the pressure read from the RGA scan are not the same as the pressure read from the hot-ion gauge. The RGA was placed near the pumps under the bottom part of the vacuum system, while the hot ion gauge was placed at the top near the cell string. The readings from the RGA were usually larger than those from the ion gauge by an order of magnitude.

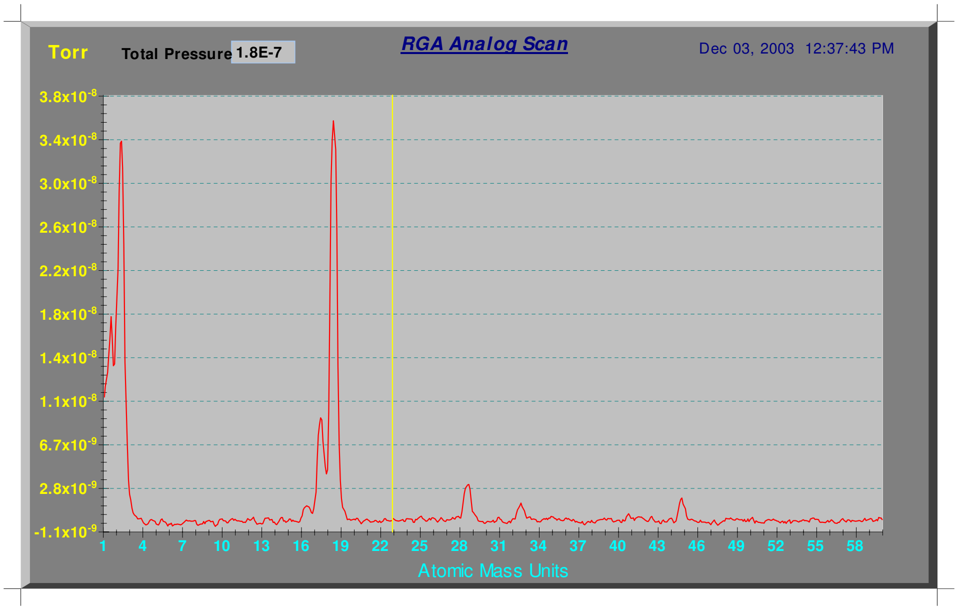

Figure 3.5: A typical RGA scan before filling the gas into the cell.

We use the values from the ion gauge to characterize the cell pressures, since the gauge is close to the cells.

After the cell string was cooled down, when the bake down was complete, the alkali metal capsule, attached at one end of the string, was broken by a small magnet. Contaminants were released from the broken capsule. The removal of impurities from the alkali metal is believed to be critical to the cell's final performance. Several hours are needed to pump off these contaminants. Figure 3.5 shows a RGA scan graph for a cell string after removing all contaminants. The major residual gases were only hydrogen and nitrogen.

3.3.2 Cell Construction

After the system's pressure reaches equilibrium, a few milligrams of alkali metal are chased with a torch into the upper chamber of the cell. Then the cell is ready to be filled with ^{3}He gas and N_2 buffer gas.

The entire vacuum system can be divided into two parts, by a main valve. The lower part contains all the pumps and the RGA. The upper part of the vacuum system contains ^{3}He, N_2 bottles and the cell string. Between the gas bottles and the remaining part of the vacuum manifold, there are small buffer volumes separated by valves, which serve as reservoirs between the gas bottles and the cells string.

To fill the cells, the main valve is first closed. Then valves between the buffer volumes and the vacuum manifold are closed. A small amount of nitrogen or ^{3}He gas is released into a buffer volume. After closing the gas bottle valve, the cell-end valve is opened. The gas in the buffer volume then enters the cells.

During the filling process, the cell's pressure is monitored by a gauge. The cell is filled to the desired ^{3}He and nitrogen densities by repeating the filling cycle. Finally, filled cells are pulled off from the vacuum manifold and sealed by a torch.

The ^{3}He had a purity of 99.9% (Spectra Gases, ^{3}He - atom 99.9%, 5 liter bottle). Since alkali metals are excellent getters to purify gas, we did not apply any additional ^{3}He gas purifying procedures.

The final ^{3}He number densities are converted from the gas pressure by $n = P/k_BT$. A typical potassium cell in the experiments contains a density of $\sim$0.66 amagats of ^{3}He and $\sim$0.1 amagats of nitrogen.

3.4 Target Setup

3.4.1 Overview

The experimental setup is shown in Figure 3.6. In the experiments, the top chamber of the cell was placed in a high temperature plastic oven and sealed with high temperature epoxy. The oven was then mounted in the target station. The target station was originally built and used in the polarized ^{3}He experiments performed at the Stanford Linear Accelerator Center in the 1990s [33, 40, 43, 36, 44] and has been adapted for laboratory tests.

The experimental setup shown in Figure 3.6 consisted of a pair of 1.4 meter diameter Helmholtz coils that generated a uniform 20 to 40 Gauss magnetic field along the pump beam direction, which worked as the holding field for the ^{3}He nuclear polarization. The residual magnetic field gradients near the center of the target stand were measured to be on the order of $\sim$10 mG/cm. The target cell was placed in the center of the Helmholtz coil. A pair of rf drive coils and a separate pair of pickup coils surround the cell and were used for nuclear magnetic resonance measurements of the ^{3}He polarization using adiabatic fast passage (AFP)[3].

During the experiments the top chamber was heated by hot air flow at temperatures between 180 °C and 230 °C, while the lower chamber was maintained at a relatively low temperature of 40°C for the polarization measurements. The cell's temperature was monitored by several RTD (Resistive Temperature Devices) elements.

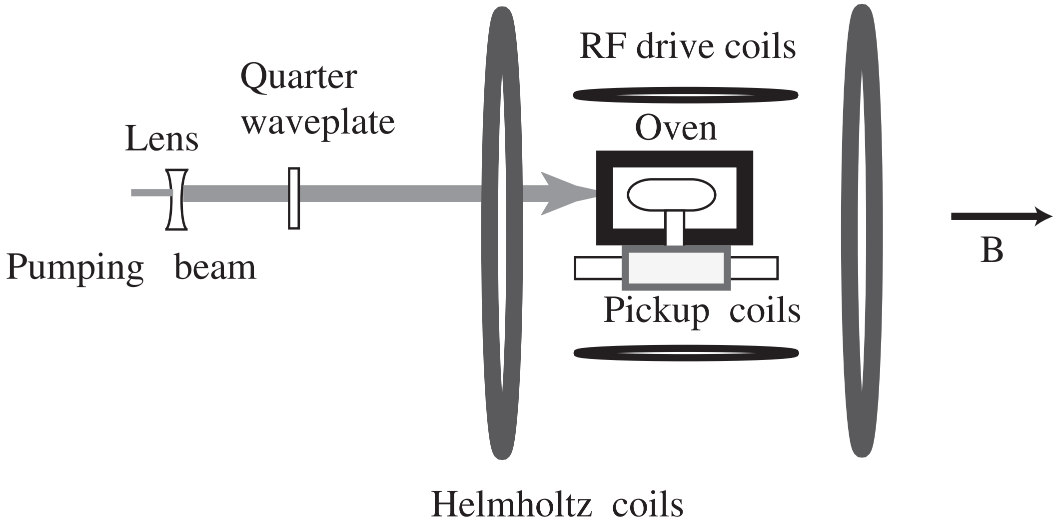

Figure 3.6: Experiment setup. Circularly polarized laser light was used to polarize the potassium vapor in the top chamber of the target cell. A holding magnetic field was generated by the Helmholtz coils. The ^{3}He polarization was measured using the drive and pickup coils shown. Thermal equilibrium polarization of protons in water was measured in the same setup to calibrate the ^{3}He signal.

3.4.2 Lasers and Optics

A single Ti:sapphire laser (Spectra-Physics, Model 3900S) with a linewidth of 40 GHz and 5 watts output power was used to polarize the potassium vapor. The Ti:sapphire laser was pumped by a 20 watt Argon ion laser (Spectra-Physics, Model 2040E). A picture of the Ti:sappire lasers with the pumping lasers is shown in Figure 3.7.

The wavelength was tuned to the potassium $D1$ line at 770 nm. A set of telescope lenses were placed in front of the laser head to expand the laser beam size from 1 mm to about 1.5 inch in order to expose the full upper cell chamber to the laser light, as shown in Figure 3.6. The laser light was originally linear polarized ($> 100 : 1$ horizontal). After passing through a high power quarter waveplate placed in the optical path, circular polarization of the light was created.

A series of measurements were conducted to characterize the laser light properties.

Figure 3.7: The Ti:sappire lasers and Argon ion lasers in the lab.

The laser power was measured by a power meter. For fine tuning, the laser wavelength was monitored by a wavelength meter (ILX Lightwave, model LWM-6500B) with a resolution of 0.01 nm. The spatial laser beam profile was observed by an infrared sensor card and an infrared viewer scope. A fiber beam profiler system (Photon Inc. Model 2350) was also used to analysis the laser beam mode parameters.

Besides laser powers, wavelengths and spatial modes, it is also important to know the laser circular polarization quantitatively in the experiments. To measure the circular polarization of laser light, Stokes polarimetry was applied. As shown in Figure 3.8, a polarizing beamsplitter cube (PBS) separated the laser beam into two orthogonally polarized components. The PBS was mounted on a rotary stage and served as a polarizer which has the ability to rotate the passing axis 360° in the plane vertical to the beam propagating direction. By measuring the transmitted light intensities in each direction, the minor axis and major axis of the light electric vector can be found, along with the maximum and minimum recorded intensities I_{max} and I_{min}. The circular polarization can be found by

$$P = \frac{2\sqrt{I_{min}/I_{max}}}{1 + I_{min}/I_{max}}. \tag{3.1}$$

In the experiments, a zeroth-order quarter waveplate designed for the correct wavelength was used to convert the horizontal polarized laser light to the circular polarized light. The resulting circular polarization was always better than 95% (corresponding to $I_{min}/I_{max} > 3/5$).

The derivation of Equation 3.1 is straightforward. An elliptical polarized beam can be modeled as

$$E = E_0 \cos\theta \cos\omega t \mathbf{e_x} + E_0 \sin\theta \cos(\omega t + \varphi)\mathbf{e_y}, \tag{3.2}$$

where E is the electric vector, $E_x = E_0 \cos\theta$ is the electric field amplitude of the x component, $E_y = E_0 \sin\theta$ is the y component, φ is the phase difference between E_x and E_y, and ω is the light frequency. In Equation 3.2, the light is linear polarized when $\varphi = 0$. On the other hand, the light is circularly polarized only when $\varphi = \pi/2$ and $\theta = \pi/4$. To describe the polarization, four Stokes Parameters were used [85]:

$$I = \text{total intensity} \tag{3.3}$$

$$q \equiv Q/I = < \cos 2\theta \cos 2\chi > \quad (3.4)$$

$$u \equiv U/I = < \sin 2\theta \cos 2\chi > \quad (3.5)$$

$$v \equiv V/I = < \sin 2\chi >, \quad (3.6)$$

where the angle χ satisfies $\sin 2\chi = \sin 2\theta \sin \varphi$. Consequently, $\tan \chi = E_{min}/E_{max}$ is the minor to major axis ratio. Note that

$$q^2 + u^2 + v^2 = 1 \quad (3.7)$$

for a fully polarized beam.

The degree of linear polarization is defined as

$$P = \sqrt{q^2 + u^2} \quad (3.8)$$

and the circular polarization is

$$P = v =< \sin 2\chi > . \quad (3.9)$$

Inserting the definition of χ into Equation 3.9, Equation 3.1 is obtained.

During the experiments, the helicity of the laser light is also needed. Left and right circularly polarized light excite alkali metal atom electrons in the opposite directions, respectively. If σ^+ light is applied, the electrons are pumped to the high energy Zeeman sub-state. In this case, a phenomenon called spin masing [44] can occur,

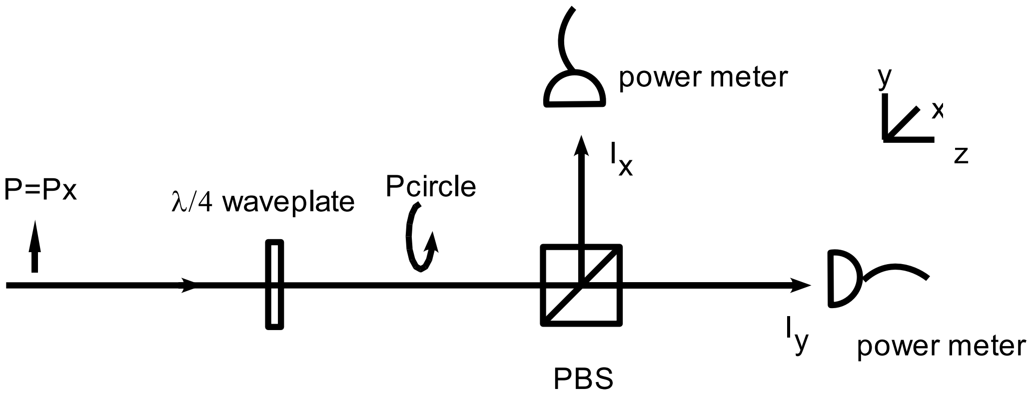

Figure 3.8: Laser light polarimetry setup. The light propagated along the z direction while the polarization lay in the x-y plane. After passing the polarizer, the transmitted light intensities were measured. The ratio of the minimum transmitted light intensity to the maximum transmitted light intensity is recorded as $I_{min}/I_{max} = \tan^2 \chi$. The circular polarization is $P_c = \sin 2\chi$.

which results in the electron polarization dropping abruptly. When this occurs, we have to reverse the helicity of the light to σ^- by rotating the quarter waveplate by 90°. In addition, when two or more laser beams were combined for optical pumping, the helicity of each beam needed be the same. Otherwise, their effects would cancel out.

The light helicity is easily checked by passing the beam through a quarter waveplate. Supposing the fast axis of the waveplate is along the x direction, then, when σ^+ light passes the waveplate, the transmitted light is linearly polarized with an angle of $-45°$ to the x-axis. On the contrary, when σ^- light passes the waveplate, the linear polarization direction of the transmitted light is $+45°$ to the x-axis.

The wavelength tuning range of the Ti:sapphire laser used in the experiments varies from 700 nm to 980 nm, which includes the D1 lines of potassium, rubidium and cesium. In the actual experiments, the wavelength was tuned to be a little bit off the D1 resonance, since on-resonant light will be strongly absorbed. Compared to the case of off-resonance pumping, on-resonance pumping will result in a decrease in the alkali metal polarization [32]. During the optical pumping process, a CCD camera monitored the light absorption in the target cell. The optimum laser wavelength was achieved when all the laser light was absorbed at the rear end of cell.

For comparison, the high power diode laser arrays were also used to optically pump the alkali metal atoms. The bandwidth of the diode laser arrays is about 2 nm, which is broader than the Ti:sapphire laser by a factor of 20. Experiments in our lab showed that 5 to 10 times more laser power was needed for the diode laser to yield a similar polarization compared to the Ti:sapphire laser.

Using the broadband diode laser rather than the Ti:sapphire laser for optically pumping potassium has another potential problem related to the laser power efficiency. The spacing between the D1 and D2 lines for potassium is narrower than the spacing for rubidium, 3 nm and 15 nm, respectively. The 3 nm spacing is comparable to the diode laser bandwidth, so the additional D2 resonant absorption may reduce the laser power efficiency for optically pumping potassium-^{3}He targets.

3.4.3 Magnetic Fields

The holding magnetic field was generated by a pair of 1.4 m Helmholtz coils, shown in Figure 3.9.

The holding magnetic field generated by the Helmholtz coils was controlled by a series of computer programs, a function generator, an rf amplifier and a power supply. A labview program controlled the function generator (Hewlett Packard, model

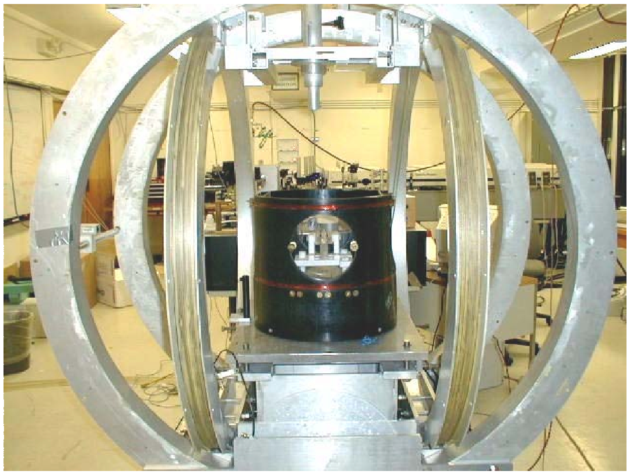

Figure 3.9: The target station.

3325B) through a GPIB interface. The function generator generated the drive signal with a programmed wave shape and frequency. Then, the signal was amplified by a bipolar operational power supply/amplifier (Kepco, Model BOP 36-12M). The Kepco amplifier worked in the constant current mode with an output of 5 to 10 Amperes and controlled the holding magnetic field. The magnetic field strength was adjusted and swept by the program.

The rf drive coils used in the ^{3}He polarization measurements were controlled in a similar manner as the Helmholtz coils.

3.4.4 Heating Oven and Temperature Measurements

The top chamber of the cell was placed in a homemade high temperature plastic oven. In our experiments, the top chamber was heated by hot air flow. The oven withstood continuous heating at 230 °C for several days. However, longtime heating can burn the screws and the plastic windows in the oven. Therefore, the heating time and heating temperatures were carefully controlled and monitored.

The cell temperature was detected by RTDs placed in different positions near the cell's pumping chamber and near the bottom chamber. Since the whole cell was not in thermal equilibrium, multiple RTDs were used to characterize the cell temperature.

In addition, since the pumping chamber was heated by the laser light, the hot air flow temperature near the cell detected by the RTDs is not necessarily the temperature of ^{3}He gas in the cell. To determine the temperature uncertainty, the ^{3}He polarization signals were measured and compared for the cases of laser on and laser off. The two measurements were taken in a relatively short time interval, so the ^{3}He polarization decay between the measurements can be ignored. The ^{3}He polarization signals are proportional to the ^{3}He density in the bottom chamber, which is inversely proportional to the temperature. Therefore, the signal amplitude variation between the two measurements is caused by laser heating. We found that a 5°C temperature uncertainty is adequate to understand these effects when calibrating the ^{3}He polarization in the cell.

The heat flowed from the upper chamber to the bottom through the neck. The temperature near the center of the bottom chamber is slightly higher than the temperature near the ends. A position averaged temperature with a ±5°C uncertainty for the bottom chamber temperature was used to calculate the ^{3}He density in the bottom chamber.

Chapter 4

^{3}He NMR-AFP Polarimetry

In this chapter, the principle of ^{3}He polarimetry using Nuclear Magnetic Resonance with Adiabatic Fast Passage (AFP) will be discussed, followed by a description of the electronics setup. Then, modeling of water NMR-AFP signals will be presented. The ^{3}He polarimetry using water signals will be discussed in detail.

4.1 Overview

To measure the ^{3}He polarization, a nuclear magnetic resonance technique named adiabatic fast passage [3] was adopted. In this method, the polarized ^{3}He target was exposed to an rf magnetic field B_y in the y-direction, plus a uniform holding magnetic field B_z along the z axis. A pair of pickup coils situated in the y-z plane were placed near the ^{3}He target. The induced voltage in the pickup coils from the ^{3}He spin precession was then detected. Figure 4.1 shows the experimental layout.

The induced voltage in the pickup coils is proportional to the changing rate of magnetic field flux in the x direction. Note that the holding field and the rf field are both orthogonal to the x-axis. The x-component of the magnetic flux is only produced

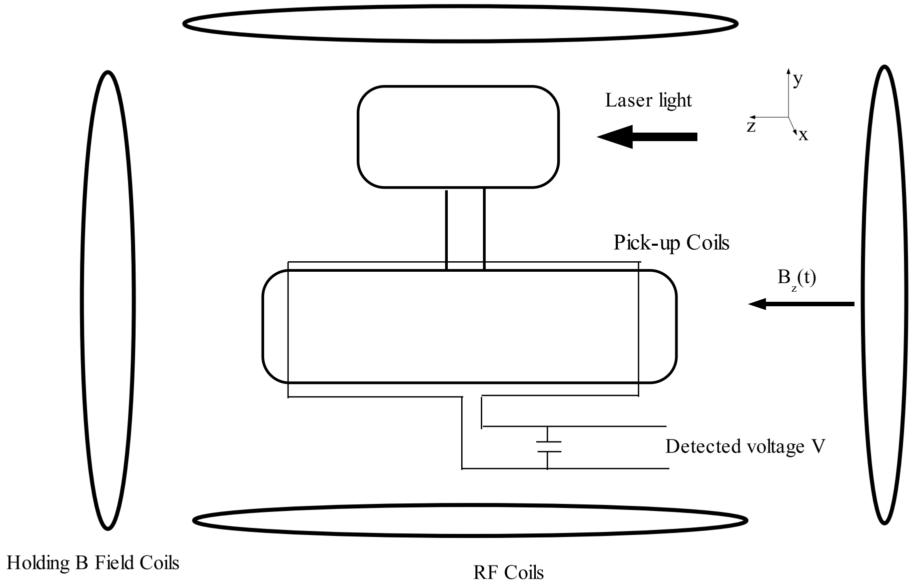

Figure 4.1: The NMR-AFP setup. The holding field, the rf field and a pair of detection pickup coils are in the z, y, x directions, respectively. The pickup coils are coupled to a capacitor. The induced voltage in the pickup coils is recorded and measured. Note that the objects sizes in this figure are not to scale.

by the magnetic moment from the polarized ^{3}He nuclei, which is proportional to the ^{3}He polarization. Therefore, the detected signal provides a measure of the ^{3}He polarization.

During AFP measurements, the holding field B_z is swept slowly so that the ^{3}He spins follow the field adiabatically. As a consequence, the detected signal varies with time. The B_z field is swept linearly in time through a resonance point, resulting in a peak signal passing through the pickup coils.

To calibrate the ^{3}He polarization signal, the polarization of protons in a water cell with the same geometry as the ^{3}He cell is measured in the same setup. The water thermal equilibrium polarization is known from Equation 1.1, which is a function of only the water temperature and the holding magnetic field strength. Comparing the calculated water polarization with the measured water signal, the calibration constant of the system can be determined.

In the subsequent sections, this method will be explained in detail.

4.2 Adiabatic Fast Passage

4.2.1 Spin Motion in Magnetic Fields

A nuclear spin **I** is related to its magnetic moment **M** by $\mathbf{M} = \gamma\hbar\mathbf{I}$ as described in Chapter 2. Supposing this spin is in a magnetic field **B**, then it feels a torque $\mathbf{M}\times\mathbf{B}$. The motion of the spin will be

$$\frac{d(\hbar\mathbf{I})}{dt} = \mathbf{M}\times\mathbf{B}, \tag{4.1}$$

which can be expressed in terms of magnetic moment **M** as

$$\frac{d\mathbf{M}}{dt} = \gamma\mathbf{M}\times\mathbf{B}. \tag{4.2}$$

For a uniform field $\mathbf{B} = B_z\hat{e}_z$, the magnetic moment precesses along $\hat{e}_z$ at the Larmor frequency $f = \gamma B_z$. And, the magnitude of **M** is constant in time,

$$\frac{d}{dt}(M^2) = 2M\cdot\frac{dM}{dt} = 0. \tag{4.3}$$

In the y direction, now let's suppose there is an additional oscillating rf field with a frequency of ω_0,

$$\mathbf{B_1} = 2B_1 \cos(\omega_0 t)\hat{e}_y. \tag{4.4}$$

This oscillating field can be decomposed into two counter rotating fields $\mathbf{B_1} = \mathbf{B}_+ + \mathbf{B}_-$, where

$$\mathbf{B}_+ = B_1\hat{e}_+(t) \equiv B_1[\cos(\omega_0 t)\hat{e}_y - \sin(\omega_0 t)\hat{e}_x] \tag{4.5}$$

$$\mathbf{B}_- = B_1\hat{e}_-(t) \equiv B_1[\cos(\omega_0 t)\hat{e}_y + \sin(\omega_0 t)\hat{e}_x]. \tag{4.6}$$

To solve for the precession in the field $B_z\hat{e}_z + \mathbf{B_1}$, it is convenient to switch to a rotating frame where

$$\begin{aligned}
\hat{e}'_z &= \hat{e}_z && (4.7)\\
\hat{e}'_x &= \hat{e}_+(t) = \cos(\omega_0 t)\hat{e}_y - \sin(\omega_0 t)\hat{e}_x && (4.8)\\
\hat{e}'_y &= \cos(\omega_0 t)\hat{e}_x + \sin(\omega_0 t)\hat{e}_y. && (4.9)
\end{aligned}$$

In this frame, $\mathbf{B}_+$ is constant along the x axis, while $\mathbf{B}_-$ rotates along the z axis at a frequency of $2\omega_0$.

Recall that in a rotating frame, the operator $\frac{d}{dt}$ transfers as

$$\frac{\partial}{\partial t} = \frac{d}{dt} + \omega_0 \times . \tag{4.10}$$

The magnetic moment's motion in this rotating frame is given by

$$\frac{\partial \mathbf{M}}{\partial t} = \gamma \mathbf{M} \times \{[(B_z - \frac{\omega_0}{\gamma})\hat{e}'_z + B_1 \hat{e}'_x] + B_1[\cos(2\omega_0 t)\hat{e}'_x + \sin(2\omega_0 t)\hat{e}'_y]\} \tag{4.11}$$

$$\equiv \gamma \mathbf{M} \times \{\mathbf{B_e} + B_1[\cos(2\omega_0 t)\hat{e}'_x + \sin(2\omega_0 t)\hat{e}'_y]\}, \tag{4.12}$$

where the effective field $\mathbf{B_e}$ is defined as

$$\mathbf{B_e} = (B_z - \frac{\omega_0}{\gamma})\hat{e}'_z + B_1 \hat{e}'_x \tag{4.13}$$

with a magnitude of

$$B_e = \sqrt{(B_z - \frac{\omega_0}{\gamma})^2 + B_1^2}. \tag{4.14}$$

In our experiments, the rf field B_1 was far smaller than the holding field B_z, i.e., $B_1/B_z \ll 1$. Under such conditions, it can be shown that the last counter rotating term in Equation 4.12 is negligible. The spin motion equation simplifies to

$$\frac{\partial \mathbf{M}}{\partial t} = \gamma \mathbf{M} \times \mathbf{B_e}. \tag{4.15}$$

According to Equation 4.15, the magnetic moment precesses along the effective field $\mathbf{B_e}$ with a Larmor frequency $\omega = \gamma B_e$ in the rotating frame.

Before continuing the discussion, it is useful to examine how well Equation 4.15 approximates Equation 4.12. The counter rotating $2\omega_0$ component is only noticeable when $B_e \approx B_1$, i.e., near the resonance

$$B_z = \frac{\omega_0}{\gamma}. \tag{4.16}$$

The magnetic moment will experience a resonance when the Larmor precession frequency $\omega = \gamma B_e$ is equal to the counter rotating frequency $2\omega_0$. So the resonance condition is modified from Equation 4.16 to

$$\gamma B_e = 2\omega_0. \tag{4.17}$$

Inserting the magnitude of B_e from Equation 4.14 into Equation 4.17, with a first-order approximation for B_1/B_z, the resonance frequency is solved and becomes

$$B_z = \frac{\omega_0}{\gamma}(1 + \frac{B_1^2}{4B_z^2}). \tag{4.18}$$

Compared to Equation 4.16, the resonance frequency shifts by a factor of $(B_1/2B_z)^2$, which is on the order of 10^{-6} for our experiments. This effect is indeed negligible.

4.2.2 Adiabatic Fast Passage

During AFP, the holding field B_z was swept linearly in time as $B_z(t) = \dot{B}t + B_z(t=0)$. Initially the condition $B_z \ll \frac{\omega_0}{\gamma}$ holds. Therefore, the effective field $\mathbf{B_e}$ is almost parallel to the z axis at the beginning (i.e., $\frac{\omega_0}{\gamma} - B_z(t) \gg B_1$). Since the ^{3}He magnetization is along the z-axis initially, the magnetization precesses around $\mathbf{B_e}$ with a very small angle that can be regarded as being parallel to $\mathbf{B_e}$.

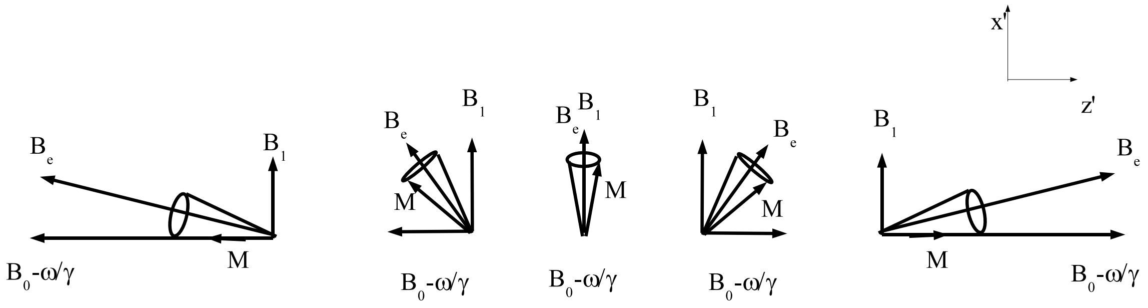

Figure 4.2: Adiabatic Fast Passage process. In the rotating frame, the magnetization **M** follows the effective field $\mathbf{B_e}$ through resonance. Initially the magnetization is along the -z direction. After sweeping, the magnetization reverses to the +z direction.

The adiabatic theorem [3] states that if the sweeping rate $\dot{B}$ is slow enough, the angle between the magnetization and the effective field will be constant. Providing this initial condition and the fact that the amplitude of the magnetization is a constant, from Equation 4.3, one can conclude that the magnetization will follow the effective field during a sweep.

The magnetic field B_z was swept through resonance at $B_z = \frac{\omega_0}{\gamma}$ until the effective field $\mathbf{B_e}$ is anti-parallel to the z axis ($B_z(t) - \frac{\omega_0}{\gamma} \gg B_1$). The magnetization then flips its direction while keeping the amplitude unchanged. Figure 4.2 shows the AFP process.

The adiabatic condition is satisfied when the relative rate of change of the effective field $\mathbf{B_e}$ in the radial direction is significantly slower than the Larmor precession frequency. In other words,

$$\frac{1}{B_e}(\dot{B} \cdot \frac{B_1}{B_e}) \ll \gamma B_e \tag{4.19}$$

$$\Rightarrow \dot{B} \ll \frac{\gamma B_e^3}{B_1}. \tag{4.20}$$

Since $B_e \geq B_1$, the above condition can be written as

$$\dot{B} \ll \gamma B_1^2. \tag{4.21}$$

Equation 4.21 sets an upper bound on $\dot{B}$. There is also a lower bound on $\dot{B}$. Since the target's magnetization is proportional to the ^{3}He polarization, the sweeping rate $\dot{B}$ can not be too slow so as to depolarize the ^{3}He . The ^{3}He relaxation rate due to inhomogeneities in the magnetic field is given by [36]

$$\frac{1}{T_r} \approx \frac{\pi D}{2} \frac{|\nabla B_z|^2}{B_1^2}, \tag{4.22}$$

where D is the ^{3}He diffusion constant. The following condition

$$\frac{\pi D}{2} \frac{|\nabla B_z|^2}{B_1^2} \ll \frac{\dot{B}}{B_e} \leq \frac{\dot{B}}{B_1} \tag{4.23}$$

has to be satisfied.

Equations 4.21 and 4.21 can be combined to give

$$\frac{\pi D}{2} \frac{|\nabla B_z|^2}{B_1} \ll \dot{B} \ll \gamma B_1^2. \tag{4.24}$$

For our case, the ^{3}He diffusion constant is ~ 0.03 cm^{2}s^{-1}, the holding field inhomogeneity and the rf field strength were about 10 mGauss/cm and 50×10^{-3} Gauss, respectively, which were found from the measured resonance signals. Therefore, Equation 4.24 becomes numerically,

$$10^{-4} \ll \dot{B} \ll 20 \ \texttt{(Unit:Gauss/Second).} \tag{4.25}$$

The sweeping rate $\dot{B}$ was set to be ~ 2 Gauss/Second in practice.

4.2.3 Measured AFP Signals

The ^{3}He gas contained in the target cell has a polarization P along the z axis as defined in Equation 2.42. The polarized ^{3}He sample, therefore, has a magnetization associated with P along the direction of the effective field:

$$\mathbf{M} = \mu\rho P \mathbf{B_e(t)}, \tag{4.26}$$

where μ is the nuclear magnetic moment of ^{3}He and ρ is the ^{3}He density. The induced voltage signal in the pickup coils is proportional to the sample's rate of change of magnetization in the x-direction:

$$S(t) = \frac{d}{dt}\left|\int \mathbf{M_x} ds\right| \tag{4.27}$$

Inserting Equations 4.26, 4.13 into 4.27, the pickup signal becomes

$$S(t) = \mu\rho P \frac{B_1}{\sqrt{(\dot{B}t - \frac{\omega_0}{\gamma})^2 + B_1^2}} \omega_0 \sin \omega_0 t A, \tag{4.28}$$

where we assume that the magnetization is uniform near the pickup coils. The integral over the pickup coil's area $\int ds$ can be separated out as a geometric parameter A.

Detecting the signal $S(t)$ in Equation 4.29 at the frequency ω_0 using a lock-in amplifier gives a square-root Lorentz shape signal proportional to the ^{3}He polarization:

$$S(t) = \mu_{He}\rho_{He}k\frac{B_1}{\sqrt{(\dot{B}t - \frac{\omega_0}{\gamma})^2 + B_1^2}}P \tag{4.29}$$

where $k = \omega_0 A$ is a geometric parameter related to the magnetic fields and pickup coil geometry. The constant k is the same for any uniform sample provided the sample geometry and the position are kept constant. This fact is used to calibrate ^{3}He polarization using water NMR-AFP signals.

The peak amplitude of the AFP signal in Equation 4.29 is

$$S(t) = \mu_{He}\rho_{He}kP, \tag{4.30}$$

which is independent of the holding field and of the rf field strengths. The line shape of Equation 4.29 can be used to estimate the rf field strength, since the FWHM (full-width half-maximum) of the signal $S(t)$ in Equation 4.29 is

$$\dot{B}\Delta t = 2\sqrt{3}B_1. \tag{4.31}$$

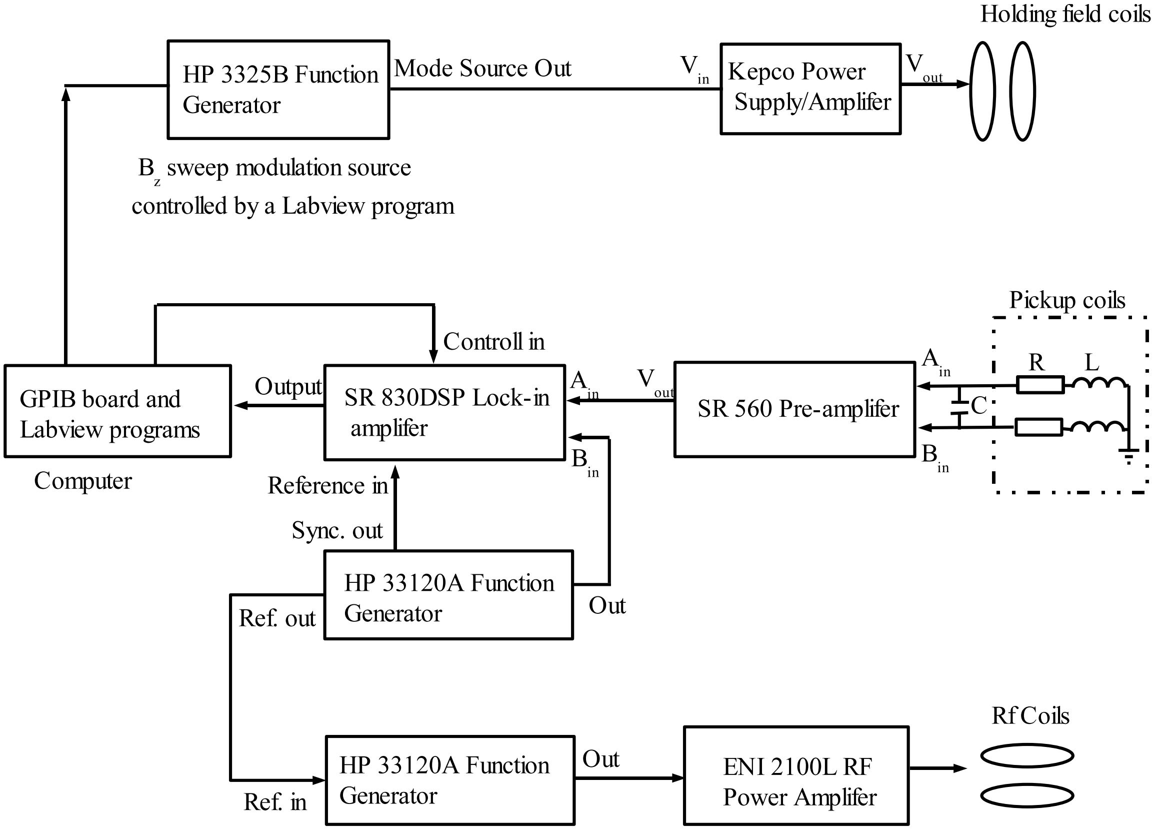

Figure 4.3: The NMR AFP electronics block diagram. The dashed block contains the equivalent RL circuit of the pickup coils. The pre-amplified induced voltage is sent to the lock-in amplifier. The data is recorded in the computer. The reference signal of the lock-in amplifier is locked to the driving source of the rf coils. A labview program controls the sweeping of the holding field and collects the measured data.

4.3 Electronics Setup

The electronic setup block diagram for the NMR-AFP system is shown in Figure 4.3. One pair of 1.4 m diameter coils served to generate the holding magnetic field in the z-direction, and another pair of 45 cm diameter coils were used to generate the rf oscillating field in the y-direction. The pickup coils are a pair of rectangular coils with a size of 3 inch in length by 1 inch in width. They were located at the center of the target station, aligned along the y-z plane. The ^{3}He target cell was placed between the pickup coils in the center of the main magnet.

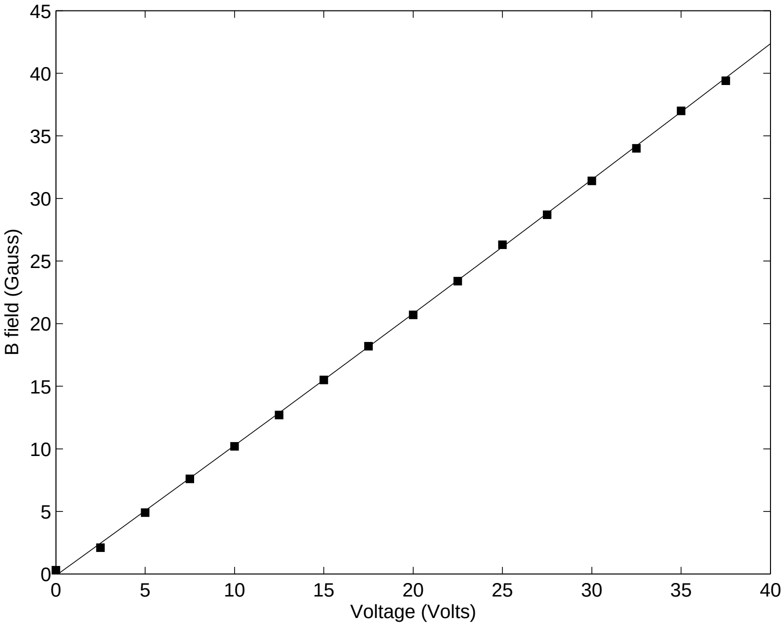

Figure 4.4: Calibration curve of the drive coils' voltage compared to the magnetic field strength. The solid line is a second-order polynomial fit of the measured data: $B = -0.12 + 1.03V + 0.0008V^2$ (Units: B Gauss; V Volts). The second-order correction is negligible.

4.3.1 Magnetic Coils

The holding magnetic coils were designed to generate a uniform magnetic field up to 40 Gauss along the z axis. The power supply was operated in the constant current mode to reduce magnetic field fluctuations caused by power supply fluctuations. The magnetic field strength was measured by a magneto-meter (Bell Inc, Model 615) and was calibrated to the voltage readings of the power supply as shown in Figure 4.4. The relationship between the voltage applied to the coils and the magnetic field strength is given by

$$B = -0.12 + 1.03V + 0.0008V^2. \tag{4.32}$$

Recalling that the nuclear gyromagnetic ratios for ^{3}He and protons are $\gamma_{^3He} = 3243$

Hz/Gauss and $\gamma_p = 4258$ Hz/Gauss, respectively, it was decided that the rf field frequency ω_0 should be set to about 100 kHz in order to have the NMR resonance be $B = \frac{\omega_0}{\gamma}$ centered near 25 guass. The rf field amplitude B_1 was between 50 to 100 mGauss.

The rf frequency was set to 85.6 kHz, corresponded to an AFP NMR resonance magnetic field for ^{3}He at 27.2 Gauss. During an AFP measurement, the holding field B_z was swept across the resonance linearly with time. The sweeping shape, sweeping rate and the sweeping range was set up in a waveform generated in the controlling program. Typically a triangle waveform with a frequency 0.1 Hz and an amplitude 10 volts was generated, and then was sent to a Hewlett Packard 3325B Synthesized Signal Generator. The generated signal waveform out of the signal generator was amplified and applied to the holding field coils. Figure 4.5 shows a typical holding main field sweep. In Figure 4.5, the holding magnetic field starts from 22 Gauss, then is increased linearly to 32.3 Gauss in 4.5 seconds and then returned to 22 Gauss at the same rate, $\dot{B} = 2.34$ Gauss/Second.

The rf coils were powered by a function generator (HP 33120A) and a rf power amplifier (ENI 2100L). The amplitude of the rf field was kept constant for all runs. The frequency and the phase of the rf field was synchronized with a reference signal for the lock-in amplifier, which was generated by another HP 33120A function generator.

4.3.2 Signal Detection

The signals are recorded by pickup coils and detected in a lock-in amplifier.

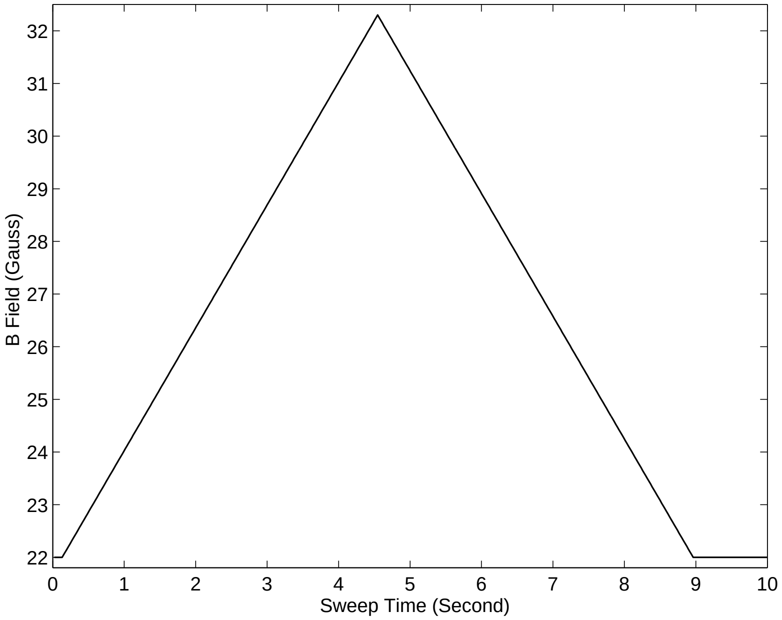

Figure 4.5: A typical sweep of the holding B field. The sweeping rate is 0.1 Hz. The flatten bottom period was designed to allow the ^{3}He polarization reaches its equilibrium between sweeps.

Each of the pickup coils was constructed out of insulated copper wires with a size of 34 AWG gauge with 150 turns. At room temperature, each of the coils has a resistance of R=39 ohm and an inductance L=3.4 mH. In Figure 4.3, the equivalent circuit of the pickup coils is shown in the dashed line block. A capacitor of 22 nF was connected across the two pickup coils. The capacitance of the coupling capacitor was chosen to correspond to a resonance frequency of $\sim$ 100 kHz ($\sqrt{\frac{1}{LC}} \sim 80$ kHz). The actual Q curve of the pickup coils was measured and is shown in Figure 4.6. During the experiments, the rf frequency was set near the peak of the Q curve, at 85.6 kHz.

The induced voltage signal from the pickup coils passed through the capacitor and was recorded in a lock-in amplifier (Stanford Research Systems Inc., model SR 830). Figure 4.7 shows a typical AFP sweep of the polarized ^{3}He NMR signal. The

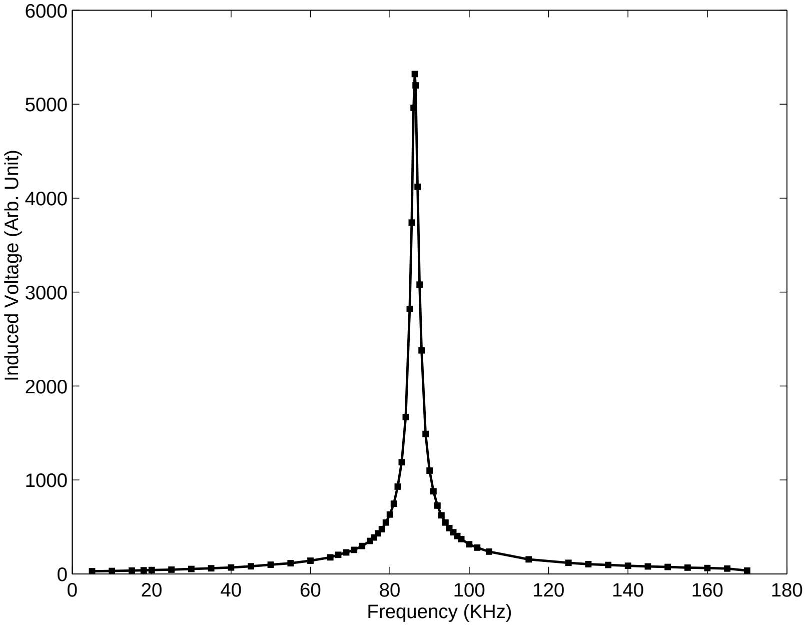

Figure 4.6: The measured Q-curve for the pickup coils.

FWHM of the first peak is about 73 ms. Using Equation 4.31, the rf field strength is estimated to be near 50 mGauss. The lock-in amplifier was controlled through a GPIB interface to the computer. The phase of the lock-in amplifier was adjusted to make the full signal appear in only one channel.

Since the rf coils are not perfectly orthogonal to the pickup coils in reality, some rf power leaks into the pickup coils as a background signal. To cancel out this background, the auto offset function on the lock-in amplifier is used during the measurements of the ^{3}He polarization. In the case where there is a large background, or the resonance signal is too small (i.e., when measuring the water AFP signal), an additional background cancelation signal was added to the amplifier. The cancelation signal was generated by a second HP function generator and was monitored on an oscilloscope (not shown in Figure 4.3).

The signal detected by the lock-in amplifier is not exactly in the form described

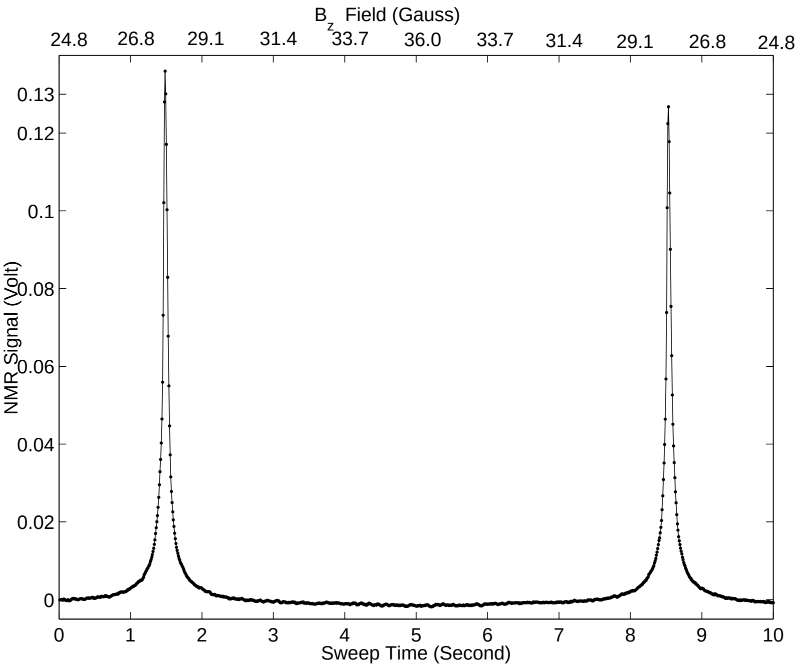

Figure 4.7: Typical polarized ^{3}He AFP NMR signals from one sweep. The top x axis corresponds to the holding magnetic field, while the bottom x axis indicates the sweep time.

by Equation 4.29. There is usually a linear background under the signal due to rf power leakage remaining after the cancelation. In addition, the time constant setting of the lock-in amplifier will modify the signal slightly. The time constant parameter of the lock-in amplifier is the inverse of the low pass filter bandwidth in the frequency domain. When it is set long, the noise is reduced. However, if the width of the peak signal is comparable to the time constant, the signal itself is attenuated.

Back in the time domain, the effect of the time constant τ can be expressed as a convolution product with the signal:

$$S_{out}(t) = \int_{-\infty}^{\infty} S_{in}(t-x)e^{-x/\tau}dx. \tag{4.33}$$

For the AFP sweeps of the ^{3}He and water signals, the time constant was set to be 10 ms. Using Equation 4.29 as the input signal $S_{in}(t)$, the time constant modification on the ^{3}He signal peak amplitude can be numerically estimated. The peak height is reduced by less than 1%. It is necessary to keep the time constant unchanged during the scans for both water and ^{3}He signals. In this case, the modification is the same for all measurements, and they cancel out in the calculation of the calibration constant.

On resonance during an AFP scan, it is possible that the ^{3}He magnetization exchanges energy with the RLC circuit of the pickup coils. Such possible AFP loss was determined by measuring the signal consecutively and rapidly, and then fitting the decay of the signals over the short time period. During such short periods, the ^{3}He polarization relaxation can be ignored, and the AFP power loss accounts for the signal decay. It was found that the AFP loss is about 0.3% for each measurement.

For certain conditions, the coupling of the pickup coils with the ^{3}He magnetization can be prominent. As discussed in Section 3.4.2, a phenomenon called spin masing can occur [44]. If the ^{3}He spins are polarized to the high energy sub-state and the ^{3}He polarization is above a threshold, the spin and the pickup coils can couple in a nonlinear manner, and the polarization of the ^{3}He target will decrease suddenly. To avoid spin masing during AFP measurements, the ^{3}He was always polarized to the lower Zeeman states.

4.4 Water Signal Calibration

Protons in water have a thermal equilibrium polarization in a magnetic field that follows Boltzmann statistics as given in Equation 1.1:

$$P = \frac{n_+ - n_-}{n_+ + n_-} = \tanh(\frac{\mu \cdot \mathbf{B}}{k_B T}). \tag{4.34}$$

At AFP resonance, $B = B_0 = \frac{\omega_0}{\gamma}$, so the thermal equilibrium polarization of protons is

$$P_r = \tanh(\frac{\mu B_0}{k_B T}) = \tanh(\frac{\hbar}{2} \cdot \frac{\omega_0}{k_B T}) \approx \frac{\hbar}{2} \cdot \frac{\omega_0}{k_B T}. \tag{4.35}$$

However, the measured water signal size is not simply related to the proton thermal equilibrium polarization in water by Equation 4.29. The situation is more complicated than the case for the ^{3}He AFP signal. The constant P_r in Equation 4.35 is only an approximation for P in Equation 4.29. The complications come from several facts.

First, the proton polarization is not in an equilibrium state during an AFP sweep. The reason is that the proton polarization relaxation rate T_1^{-1} in water is fast. The relaxation time T_1 is typically 2.4 seconds [36], which is comparable to the AFP sweeping rate. Since the relaxation cannot be neglected, the proton polarization obeys the following relaxation formula:

$$\frac{dP}{dt} = -\frac{1}{T_1}(P - P_e), \tag{4.36}$$

where P_e is the proton equilibrium polarization at time t and $1/T_1$ is the proton polarization relaxation rate in water.

The relaxation rate of polarized ^{3}He ($\sim$ hours^{-1}) is much slower than the AFP sweeping rate ($\sim$ second^{-1}), so the ^{3}He polarization can be regarded as being in an equilibrium state during an AFP scan. Therefore, Equation 4.29 describes the ^{3}He signal well.

Secondly, the thermal equilibrium proton polarization P_e changes over time during an AFP sweep. The proton energy in the holding magnetic field is $\mu \cdot \mathbf{B_t}$, where the proton magnetic moment μ is along the effective field $\mathbf{B_e} = (B_z - \frac{\omega_0}{\gamma})\hat{e}'_z + B_1\hat{e}'_x$, which is not aligned with the total magnetic field ($\mathbf{B_t} = B_z\hat{e}'_z + B_1\hat{e}'_x \neq \mathbf{B_e}$). Near resonance, the two fields are far away from parallel. Taking the inner product of the total magnetic field $\mathbf{B_t}$ with μ, the equilibrium polarization P_e is

$$P_e = \frac{\mu}{k_B T}\frac{B_z(B_z - \frac{\omega_0}{\gamma}) + B_1^2}{\sqrt{(B_z - \frac{\omega_0}{\gamma})^2 + B_1^2}}. \tag{4.37}$$

Inserting $B_z = \dot{B}t + B(t = 0)$, Equations 4.36 and 4.37 can be numerically solved. Strictly speaking, the numerical results for P should be used in the AFP evaluation, since it is not obvious that Equation 4.35 is a close approximation to the exact numerical solution.

To understand the approximation from Equation 4.35, first consider the limit when $B_1 \to 0$. Suppose $t = 0$ is the time when the AFP resonance occurs, and the initial field is below the resonance. For an up-AFP sweep when $B_1 \to 0$, Equation

4.37 reduces to

$$P_e(t) \approx -\frac{\mu}{k_B T}(\dot{B}t + \frac{\omega_0}{\gamma}). \qquad (4.38)$$

Taking the simplified $P_e(t)$ given above, the proton polarization from Equation 4.36 can be analytically solved as

$$P(t) = -\frac{\mu}{k_B T}[\frac{\omega_0}{\gamma} + \dot{B}t - \dot{B}T_1(1 - e^{\frac{t_i - t}{T_1}})], \qquad (4.39)$$

where the initial condition

$$P(t = t_i) = P_e(t = t_i) \Longleftrightarrow \frac{dP}{dt}(t = t_i) = 0 \qquad (4.40)$$

has been used. Note that the first term of Equation 4.39, when $t \to 0$, is just Equation 4.35.

During an AFP sweep, the holding field increases and then decreases at the same rate. For the down-sweep, $P_e(t)$ changes its direction and the signal size is slightly larger than the size of the up-sweep, due to the third term in Equation 4.39,

$$P(t) = \frac{\mu}{k_B T}[\frac{\omega_0}{\gamma} + \dot{B}t + \dot{B}T_1(1 - e^{\frac{t_i - t}{T_1}})]. \qquad (4.41)$$

The average of the up and down peak amplitudes is taken as the water polarization signal. Namely,

$$P_w = \frac{1}{2}(|P_{up}(t = 0) + |P_{down}(t = 0)|) \qquad (4.42)$$

$$= \frac{\mu}{k_B T}\frac{\omega_0}{\gamma}, \tag{4.43}$$

which is comparable to Equation 4.35.

To estimate the uncertainty in P_w, there are three major contributions. First, the rf magnetic field B_1 is non-zero. Second, the time interval between the sweep start time and the resonant time is not exactly the same for both the up and down sweeps, (i.e., $|t_i| \neq |t_f|$). Third, if the sweep up and down are averaged, then the signal size depends on T_1, the proton relaxation time in water.

Based on the measured B_1 values and the knowledge of T_1, Equations 4.36 and 4.37 can be solved numerically. We find that a shift of

$$R = 0.97 \tag{4.44}$$

should be multiplied to Equation 4.43 to calculate the true proton polarization. The calculation of R depends on the values of the rf field B_1 strength and the water relaxation rate T_1, and it has an overall 2% uncertainty. The treatment here follows Reference [50].

More precisely, the proton's longitudinal relaxation time T_1 and transverse relaxation time T_2 are actually slightly different. To address this difference, the relaxation Equation 4.36 is replaced by the Bloch equations [50]:

$$\frac{dP_x(t)}{dt} = -\frac{P_x(t)}{T_2} + \gamma[B(t) - \frac{\omega_0}{\gamma}]P_y(t) + \frac{\gamma B_1}{T_2} \tag{4.45}$$

$$\frac{dP_y(t)}{dt} = -\frac{P_y(t)}{T_2} - \gamma[B(t) - \frac{\omega_0}{\gamma}]P_x(t) + \gamma B_1 P_z(t) \tag{4.46}$$

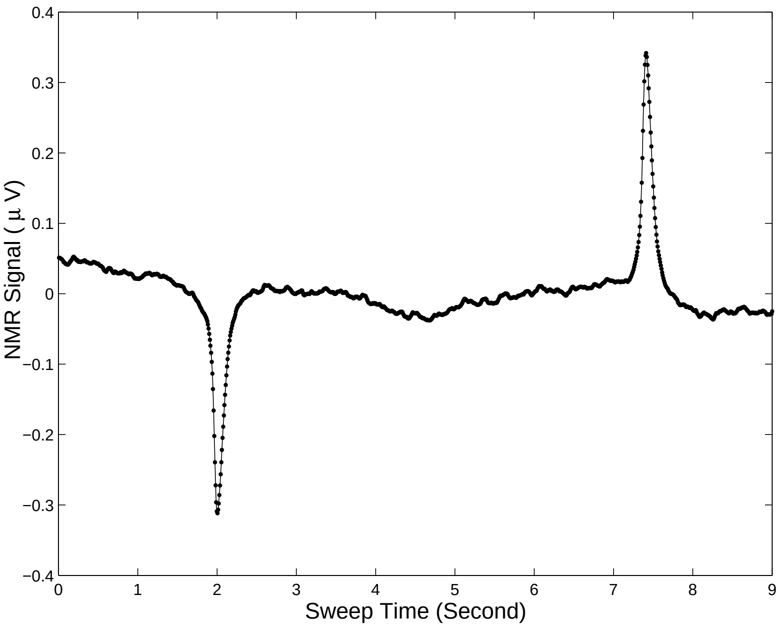

Figure 4.8: A typical water AFP NMR signal with one sweep up and down. The solid line is a fit to the peaks according to Equation 4.29.

$$\frac{dP_z(t)}{dt} = -\frac{P_z(t)}{T_1} - \gamma B_1 P_y(t) + \frac{\gamma B_1}{T_1}. \tag{4.47}$$

In deionized water, $1/T_2 = 1/T_1 + 0.125$ second^{-1} [10]. It was studied in Reference [44] and found that the height of the water peak is reduced slightly, once the effect of T_2 is taken into consideration. The relative correction from the simplified $T_1 = T_2$ assumption is less than 1%.

Figure 4.8 shows an AFP water signal. Since the water polarization is extremely small compared to the ^{3}He polarization, the water signal was amplified 100 times before feeding into a lock-in amplifier. To improve the signal-to-noise ratio, 100 sweeps were taken and averaged to get the data in Figure 4.8.

The reason that up and down sweep peaks have different directions in Figure 4.8 can be found from Equations 4.39 and 4.41. Unlike the ^{3}He polarization, since the proton relaxation rate T_1^{-1} is fast, after one sweep up, the proton polarization has relaxed back along the direction of the main holding field. For the case of ^{3}He , the relaxation can be neglected during one sweep , so the ^{3}He polarization always follows the effective field and the two ^{3}He peaks have the same sign as shown in Figure 4.7.

To minimize the uncertainty in the ^{3}He polarization determination, a water NMR signal measurement was performed immediately before and after every ^{3}He polarization process at the same driving field and the same resonant frequency as the ^{3}He measurements.

After obtaining the water AFP signal and proton polarization, the ^{3}He polarization was found from the following calibration equation,

$$P_{He} = P_{proton} \frac{S_{He}}{S_{water}} \frac{\mu_{proton}}{\mu_{He}} \frac{n_{proton}}{n_{He}^{bottom}} \frac{R_{water}^2}{R_{He}^2}, \tag{4.48}$$

where P_{He} is the ^{3}He polarization, P_{proton} is the proton polarization, S_{He} is the magnitude of the ^{3}He signal, S_{water} is the magnitude of the water signal, μ_{proton} and μ_{He} are the proton and ^{3}He magnetic moments, respectively, n_{proton} is the water proton density, n_{He}^{bottom} is the ^{3}He density in the bottom chamber, and R_{water} and R_{He} are the radii of the water and ^{3}He cells, respectively. All the gain settings of the amplifier have been taken into account.

The uncertainties in Equation 4.48 and the ^{3}He polarization data analysis are discussed in the next chapter.

Chapter 5

Measurements and Data Analysis

In this chapter, measurements of the ^{3}He polarization and the spin-exchange rate coefficients of ^{3}He and the alkali metal atoms pairs are discussed. The ^{3}He polarization calibration and the rate coefficients measurement uncertainties are studied, including discussions on the water signal calibration uncertainties, the determination of ^{3}He densities, and methods for measuring the alkali metal vapor densities.

5.1 ^{3}He Polarization Measurements

The target cells used in our experiments are made of GE-180 glass with a double-chamber design described in Chapter 3. The cells were filled with $0.5 \sim 1$ atmosphere ^{3}He and ~ 100 torr nitrogen gas. During the polarization process, a series of ^{3}He NMR-AFP signals were taken to obtain values for the ^{3}He polarization in the bottom chamber.

During the process of spin-exchange optical pumping, the ^{3}He polarization in the target cell builds up according to Equation 2.42,

$$P(t) = P_0(1 - e^{-(\gamma_{SE}+\Gamma)t}). \tag{5.1}$$

So at a particular temperature, the ^{3}He polarization versus time can be fit to a first-order exponential. The time constant parameter of the fit is $(\gamma_{SE} + \Gamma)^{-1}$.

Results from a ^{3}He polarization buildup curve are shown in Figure 5.1. The ^{3}He polarization achieved was ~27% after ~16 hours of optical pumping. The ^{3}He polarization was calculated from the calibration Equation 4.48. Table 5.1 shows a detailed breakdown of experimental values and systematic uncertainties. In Table 5.1, the water NMR-AFP signal was taken at room temperature $T = 23\,^\circ$C and the rf resonance frequency is $f = 85.6$ kHz. The water signal correction factor R is taken from Equation 4.44. The 2% uncertainty for P_{water} comes mainly from the calculation of R as discussed in the last chapter. The water signal S_{water} in Table 5.1 is the average of the up and down water NMR-AFP peak measurements. The 5% uncertainty comes from fits to the peak amplitude using a square root Lorentz shape. The peak amplitude is sensitive to the chosen baseline, which has a $\sim$ 3% statistical uncertainty, since the water signal is small. On the other hand, the ^{3}He AFP signal is large and has a small uncertainty ($<$ 1%) as seen in Figure 4.7.

A second large source of uncertainty comes from determining the ^{3}He number density in the target cell. The ^{3}He number density n_{He}^{cell} was calculated by measuring the pressure when the cell was filled. The quantity n_{He}^{cell} has a 2% relative uncertainty which comes primarily from temperature fluctuations during filling. When the target

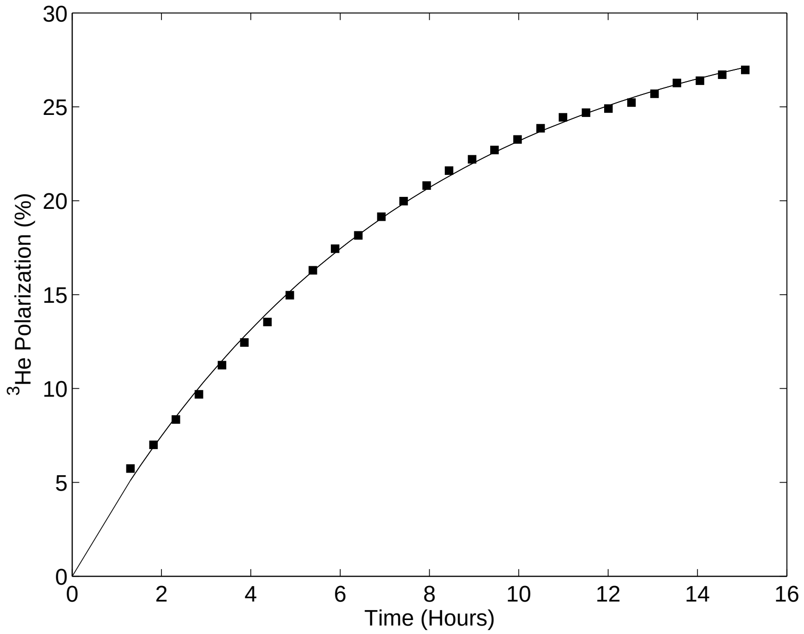

Figure 5.1: A ^{3}He spin polarization buildup curve showing the polarization of ^{3}He versus time. The pumping chamber temperature was 220 °C. The precision of the polarization measurements was ∼6%. One 4.5 watts output Ti: sapphire laser was used. The cell contains 10.3 psi of ^{3}He. The solid line is an exponential curve fit to Equation 5.1.

Parameter	value	relative uncertainty
P_{water}	6.73×10^{-9}	2%
S_{He}	4.64×10^{-2} Volts	1%
S_{water}	3.75×10^{-6} Volts	5%
μ_{proton}	$2.793\ \mu_N$	—
μ_{He}	$-2.127\ \mu_N$	—
n_{proton}	$6.647 \times 10^{22}\ cm^{-3}$	0.1%
n_{He}^{cell}	$1.77 \times 10^{19}\ cm^{-3}$	2%
$n_{He}^{bottom}/n_{He}^{cell}$	1.27	1%
R_{water}	12.0 mm	1%
R_{He}	13.2 mm	1%
P_{He}	27%	6%

Table 5.1: Calibration parameters and corresponding systematic uncertainties. In Eq. 4.48, the water protons polarization $P_{water} = R \tanh(\mu_p B/k_B T) = R \tanh(hf/2k_B T)$, where B is the resonant magnetic field, k_B is Boltzmann's constant, and a small correction factor R due to the Bloch equations is included. The rf frequency, f for both water and ^{3}He was 85.6 KHz. The ^{3}He number density in the cell n_{He}^{cell} was determined by measuring the pressure when the cell was filled.

cell is at room temperature, the ^{3}He number density is the same for both the upper and bottom chambers. The difficulty comes from the fact that it is necessary to determine the ^{3}He polarization during the pumping process when the upper chamber is hot and the bottom is near room temperature. Under such conditions, the ^{3}He number density in the bottom chamber n_{He}^{bottom} depends on the chamber temperature and is needed for extracting the ^{3}He polarization.

Suppose the volumes of the upper chamber and the bottom chamber are V_u and V_b, respectively. Ignore the volume of the connecting neck and assume the upper and bottom chamber's temperatures are T_u and T_b Then, it is easily found that the ^{3}He number density in the bottom chamber can be related to the ^{3}He filling number density via

$$\frac{n_{He}^{bottom}}{n_{He}^{cell}} = \frac{V_u + V_b}{V_b + \frac{T_b}{T_u} V_u}. \tag{5.2}$$

In order to determine the ^{3}He number density in the bottom chamber, knowledge of the inner volumes of the chambers and the chamber temperatures is required.

The cell's outside dimensions were measured by a caliper. The thickness of the cell walls was determined by measuring the resized tubes before the cells were sealed. The direct measurements have a statistical uncertainty of ±0.1 mm. The chambers' inner volumes were calculated based on the measured cell dimensions.

The partial volume calculations have uncertainties due to the fact that the cell chambers are not perfectly cylindrical. The uncertainties were estimated to be about 2%. In order to determine the volume uncertainties, for a particular Rb-He double cell used in our experiments and built for a previous experiment [36], the sum of the calculated partial volumes was compared to the result from a direct buoyancy measurement of the cell total volume. Based on the Archimedes' principle, the cell was attached to a metal block, and then was weighted under water. The inner cell volume is given by

$$V_{cell} = m_{cell}\left(\frac{1}{\rho_{water}} - \frac{1}{\rho_{glass}}\right) + m_{block}\left(\frac{1}{\rho_{water}} - \frac{1}{\rho_{block}}\right) - \frac{m_{buoyant}}{\rho_{water}}, \tag{5.3}$$

where m_{cell} is the cell's mass, m_{block} is the metal block's mass and $m_{buoyant}$ is the buoyant weight of the cell with the metal block attached under water. The difference between the buoyancy measurement and geometrical calculation is $\sim 3\%$. The GE-180 cells built in the lab did not receive such buoyancy measurements, however, all the GE-180 cells had more uniform shapes and wall thickness than the cell from Reference [36]. The 2% uncertainty of the volume for the GE-180 cells should be a reasonable estimate.

The partial volume uncertainty and the temperature measurement uncertainties contribute to the relative uncertainty of $n_{He}^{bottom}/n_{He}^{cell}$. Given that the upper chamber is 1.5 inch in diameter and 3 inch in length, the neck is 0.4 inch in diameter and 0.7 inch in length, and the bottom chamber is 1 inch in diameter and 4 inches in length, and allowing for a temperature uncertainty in the pumping chamber to be about $\Delta T \sim 5\,^{\circ}\mathrm{C}$, a simple calculation shows that a 1% relative uncertainty for $n_{He}^{bottom}/n_{He}^{cell}$ should be assigned. Note that the temperature in the pumping chamber was stabilized to within $\pm 1\,^{\circ}\mathrm{C}$. However, in the presence of the pumping laser light, the inner ^{3}He temperature could be higher than the cell wall temperature monitored by RTDs. For

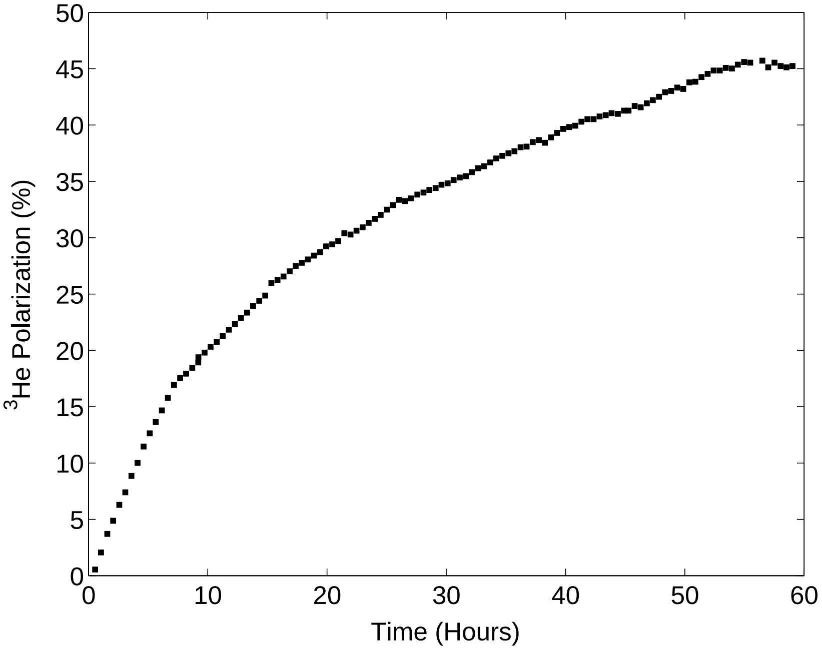

Figure 5.2: A ^{3}He spin polarization buildup curve showing the polarization of ^{3}He versus time. The temperature was adjusted several times during the measurement and ranged from 193 °C to 217 °C. The data point was taken every 30 minutes. The largest ^{3}He polarization was around 46%.

this reason, the cell temperature uncertainty was estimated to be $\sim 5\,^\circ$C when the laser is on.

The water calibration cell's radius R_{water} is slightly different from the ^{3}He cell's radius R_{He} as shown in Table 5.1. Since the ^{3}He magnetization is proportional to the number of spins in the chamber, which scales as R^2_{cell}, a correction factor of R^2_{water}/R^2_{He} enters into the ^{3}He polarization calibration in Equation 4.48.

Figure 5.2 shows a second ^{3}He polarization buildup curve for one potassium-^{3}He target cell with a higher ^{3}He polarization. After ∼60 hours of optical pumping, the final ^{3}He polarization was

$$P_{He} = (46 \pm 3)\%. \tag{5.4}$$

In Figure 5.2, the target cell was filled with 0.73 atmosphere of ^{3}He and a few mg of potassium metal. The cell was made of GE-180 glass, and the geometry was the same double-chamber design as mentioned before. The final volume of the target cell was 87 cm^3 in the top chamber and 51 cm^3 in the bottom chamber. Only one Ti sapphire laser with a linewidth of 40 GHz and 5 watts output power was used to polarize the potassium vapor.

During the pumping process, the top chamber was heated by hot air flow to temperatures between 193 °C and 217 °C, while the lower chamber was maintained at a temperature of 37°C for the polarization measurements. Note that in Figure 5.2, the temperature was adjusted several times during the measurement to find the optimum working temperature for a given laser power.

For comparison, in Figure 5.3, a polarization buildup curve for a ^{3}He cell using optical pumping of rubidium is shown. The cell used in this figure was the same cell used in the SLAC E142 experiments in the early 1990s [33, 40, 36]. The high polarization demonstrated in this figure used the same setup as for the potassium-^{3}He cell studies. The higher polarization, larger pressure and larger volume were handled by pumping with significantly more laser power, coming from both a pair of Ti:sapphire lasers and a 30 Watt diode laser operating at the rubidium D1 line. Modern polarized ^{3}He targets such as the one presently operating at Jefferson Laboratory [37, 59, 64] use multiple diode lasers consisting of ∼100 Watts of power.

Additional ^{3}He cells using optical pumping of rubidium were also built for comparison. Under the same setup as for the potassium-^{3}He cell, only ∼15% ^{3}He polarization

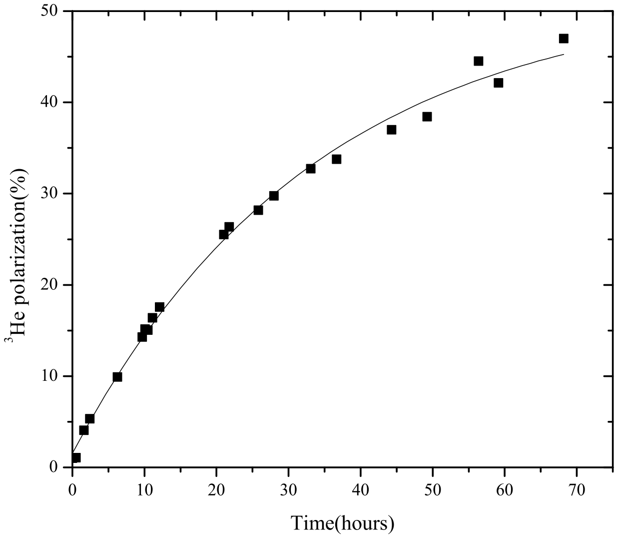

Figure 5.3: A ^{3}He spin polarization buildup curve of a rubidium-^{3}He cell. A pair of 5 watts Ti:sapphire lasers and a 30 Watt diode laser were used to optically pump rubidium vapor. A ^{3}He polarization of 44% was achieved.

was achieved with significantly more laser power, coming from three of Ti:sapphire lasers operating at the rubidium D1 line.

The rubidium-^{3}He cells were built for comparison to the potassium-^{3}He cells for the same experimental conditions. The performances of the rubidium-^{3}He cells in our lab are not as good as what has been achieved elsewhere. For rubidium-^{3}He studies, under more optimized conditions, it is possible to get good ^{3}He polarizations with less laser power. In Reference [81], a ^{3}He polarization of 70% was achieved by spin-exchange optical pumping with rubidium in cells 100 cm^{3} in volume with 1 atmosphere ^{3}He. One of the key factors in their experiments is that a homemade narrowband diode laser was used instead of the commercial ones available in most other labs, including ours. In Reference [81], a 30 W diode laser array bar selected for low array curvature was applied and the bandwidth was narrowed from 700 to 125 GHz using an external cavity, with a 4X telescope and a 2400 lines/mm grating. It is expected that when the same improvements are applied to the potassium-^{3}He cell, the potassium-^{3}He system should also show an improved efficiency.

Another effort to improve the spin-exchange optical pumping efficiency uses a hybrid K-Rb vapor mixture [80]. In this method, the rubidium atoms are optically pumped by a laser working at the rubidium D1 line. The rubidium electron spin polarization is transferred to potassium electrons via collisions. Spin-exchange collisions between both the K-^{3}He and Rb-^{3}He pairs then polarize ^{3}He with a greater efficiency than the case when only Rb-^{3}He pair are present. By this method, the advantages of cheaper rubidium lasers and a higher potassium-^{3}He spin-exchange rate can be combined at the same time. However, the performance of the hybrid cells will depend on the rubidium to potassium vapor ratio. Since the vapor pressure of rubidium is larger than that of potassium at the same temperature, it needs special treatments during the cell filling process to regulate the rubidium to potassium ratio in the cell. In the case when potassium laser sources become readily available, a potassium-^{3}He target cell may become a better candidate than a Rb-K cell mixture.

5.2 Spin-exchange Rate Coefficients

5.2.1 Overview

In the absence of pumping light, when the polarized ^{3}He target cell is hot and potassium vapor is present in the cell, the spin-exchange collisions transfer ^{3}He polarization to the potassium electron spins and contribute to the ^{3}He polarization relaxation rate. Similar to the discussions leading to Equation 2.40, it can be shown that the ^{3}He polarization relaxation rate is $\gamma_{SE}+\Gamma$. When the pumping laser is off, since alkali metal atom polarization relaxes at a much faster rate than the ^{3}He polarization relaxation rate, the alkali metal atom polarization is $P_A = N_+(A) - N_-(A) = 0$,where $N_\pm$ stand for the normalized atom state populations that satisfy $N_+ + N_- = 1$. So $N_\pm = \frac{1}{2}$ in this case. The ^{3}He polarization rate equation then becomes

$$\begin{aligned} \frac{dN_+(^3He)}{dt} &= \left[\frac{\Gamma}{2} + \frac{\gamma_{SE}}{2})\right] N_-(^3He) - \left[\frac{\Gamma}{2} + \frac{\gamma_{SE}}{2}\right] N_+(^3He) \\ 0 &= \frac{dN_+(^3He)}{dt} + \frac{dN_-(^3He)}{dt}. \end{aligned} \tag{5.5}$$

It immediately follows that the ^{3}He polarization relaxes as

$$P = P_0 e^{-(\gamma_{SE}+\Gamma)t}, \tag{5.6}$$

where the spin-exchange rate γ_{SE} has been defined in Equation 2.32 as

$$\gamma_{SE} = [K] \cdot v_{He} \cdot \sigma_{SE} \equiv [K] k_{SE}, \tag{5.7}$$

where $[K]$ stands for the potassium density and k_{SE} is called the spin-exchange rate coefficient or spin-exchange rate constant.

According to Equations 2.32 and 5.6, fits for the measured ^{3}He polarization relaxation curves at different temperatures can be used to find Γ and γ_{SE} from the data. Providing the potassium vapor density is known, then the spin-exchange rate coefficient k_{SE} can be determined. We now will discuss the measurements of Γ and γ_{SE}, the determination of the potassium density and then present results for the calculated spin-exchange rate coefficients k_{SE} for different alkali metal atom-^{3}He pairs.

Alternatively, the spin-exchange rate γ_{SE} can also be found from the exponential fit of ^{3}He polarization buildup curve as shown in Figure 5.1. However, this determination has several disadvantages.

First, in order to extract the time constant from the ^{3}He polarization buildup curve, it is necessary to polarize the ^{3}He over a time period longer or comparable to the time constant $(\gamma_{SE}+\Gamma)^{-1}$. Since the final maximum ^{3}He polarization is unknown, one has to measure the whole curve in order to obtain a reliable fit. This is not only extremely time consuming, but also it requires strict control of experimental conditions. During the measurements, one needs to keep the cell's temperature stabilized, in order to maintain a constant potassium vapor population. The measurements typically take several days of continuous optical pumping. The laser power fluctuation during the pumping process changes the potassium polarization immediately so that it contributes to the measurement uncertainties.

Secondly, the knowledge of potassium density is critical to the calculation of the spin-exchange coefficient, k_{SE}. The potassium density is inferred from the potassium vapor pressure, which is measured by monitoring the cell temperature. When the pumping laser is on, the laser light will heat the inside of the cell significantly such that the inside vapor temperature can be several degrees higher than the cell wall temperature. Even worse, since the potassium vapor is optically thick to the laser light, a temperature gradient along the laser propagation direction may exist. Therefore, the measured cell temperature can be quite different from the actual potassium vapor temperature inside the cell. As a result, it is hard to obtain a reliable potassium density measurement when the pumping laser is on.

On the other hand, the ^{3}He hot polarization relaxation measurements can be both timesaving and reliable. Without the laser light present, the ^{3}He polarization relaxation only depends on the cell temperature, which can be easily stabilized to within $\pm 1^\circ$C. The potassium vapor in the cell should be in thermal equilibrium with the cell wall, so the measured cell temperature is a good indicator of the vapor temperature.

Since the ^{3}He polarization will eventually relax to zero, the hot polarization relaxation measurements can be accelerated to obtain the time constant. One only needs to take the ^{3}He relaxation data points during a relative short time period compared to $(\Gamma + \gamma_{SE})^{-1}$, then perform a linear fit to get the time constant. Namely, when $(\Gamma + \gamma_{SE})t \ll 1$, for a particular ^{3}He polarization relaxation curve,

$$P \cong P_0[1 - (\Gamma + \gamma_{SE})t]. \tag{5.8}$$

The intercept from the fit divided by the slope is the time constant $(\Gamma + \gamma_{SE})^{-1}$.

5.2.2 ^{3}He Polarization Relaxation Rate Measurements

5.2.2.1 Room Temperature Relaxation Rates

The ^{3}He polarization wall relaxation rate in the cell, $1/\Gamma_{He}$, can be found from a room temperature ^{3}He polarization relaxation measurement as shown in Figure 5.4.

At room temperature, the potassium vapor present in the cell is negligible, so the ^{3}He polarization decays as

$$P = P_0 e^{-\Gamma t}. \tag{5.9}$$

In Figure 5.4, the solid line is a first-order exponential fit to Equation 5.9. The cell in Figure 5.4 has a wall relaxation lifetime of

$$\Gamma^{-1} = (20.6 \pm 0.3) \text{ hours}. \tag{5.10}$$

The cell shown in Figure 5.4 was among the first GE-180 potassium-^{3}He cells that we made. Later cells consistently had lifetimes Γ^{-1} greater than 50 hours. Figure 5.5 shows the lifetime measurements of the cell used to demonstrate high ^{3}He polarization shown in Figure 5.2. The wall relaxation lifetime is measured to be 58 ± 2 hours.

For the long lifetime cells, since the ^{3}He polarization relaxation rate is slow, it is necessary to correct for the NMR-AFP loss in the data before performing the fit. The measured 0.3% AFP loss has been added to the data points in Figure 5.5. In Figure 5.5, the first several data were excluded during the fits, because at that time

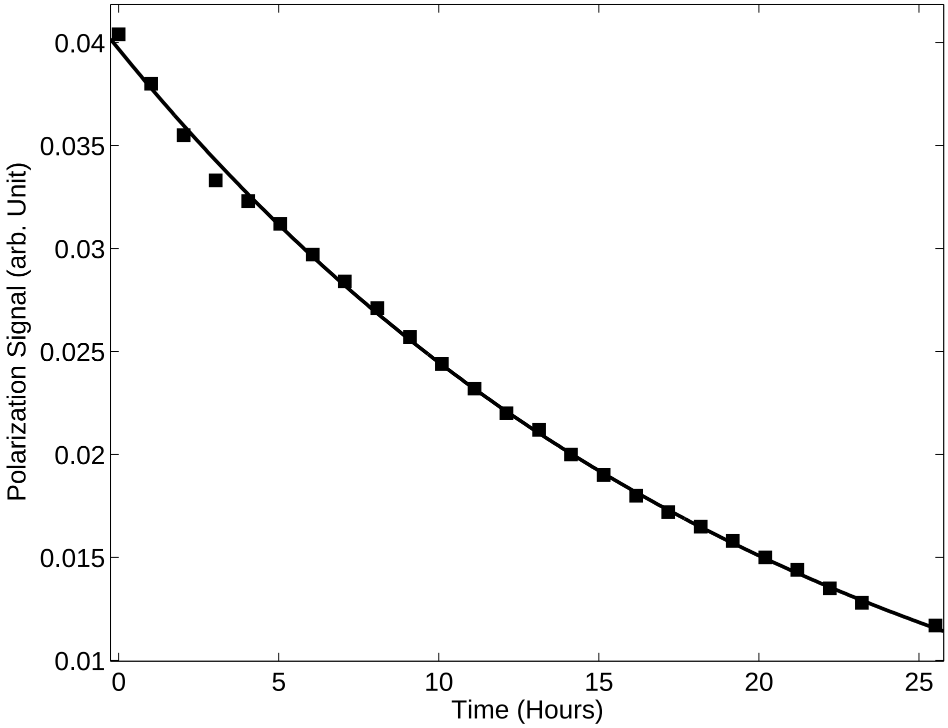

Figure 5.4: A ^{3}He polarization relaxation curve at room temperature. The solid line is an exponential fit to find the cell's lifetime.

the target cell had not reached thermal equilibrium at room temperature.

To get an accurate measurement of Γ^{-1}, it is safe to take the data over a time interval comparable to or longer than Γ^{-1}. To speed up the measurements and check whether a shorter time range is good enough to determine Γ^{-1}, an exponential fit was performed each time when a new data point is taken and included in the data set, until the results are stable.

The time interval between consecutive measurements and the minimum total number of data points were carefully chosen based on consideration of the measurement uncertainties. For the room temperature cell lifetime measurements, when the ^{3}He polarization relaxation is slow, it is possible that the ^{3}He NMR-AFP peak amplitude uncertainty is comparable to the magnitude of the ^{3}He polarization relaxation between

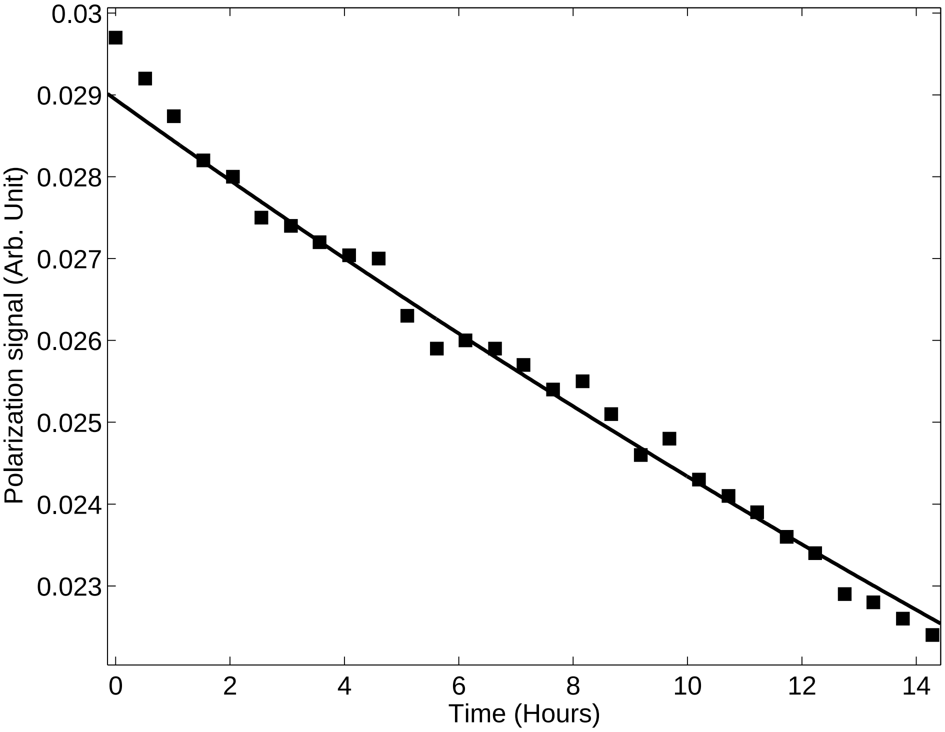

Figure 5.5: A ^{3}He polarization relaxation curve at room temperature for a second potassium-^{3}He cell.

measurements. In this case, taking too fewer points brings in large uncertainties in the determination of the time constant Γ.

To illustrate this point, suppose that the NMR-AFP signal uncertainty is 1% as listed in Table 5.1, and denote Δt as the time interval between two consecutive measurements, n is the number of data points, then we want

$$\Gamma\Delta t \geq 1\% \tag{5.11}$$

$$\frac{\Delta P}{P} = n\Gamma\Delta t \gg 1\% \tag{5.12}$$

to ensure that the individual uncertainties do not affect the final results significantly.

For the cells with $\Gamma^{-1} \sim 50$ hours, according to Equation 5.12, the time interval between two consecutive measurements was set to 0.5 hours or longer to make sure that the ^{3}He polarization decay is observable and to reduce the ^{3}He polarization measurement uncertainty. The total number of the data point n was set to be larger than 10 in order to satisfy $n\Gamma\Delta t \gg 1\%$.

5.2.2.2 ^{3}He Polarization Relaxation in a Hot Double Chamber Cell

The ^{3}He polarization relaxation measurements are straightforward for a hot single-chamber cell, similar to the room temperature measurements. Several single cells were built to measure γ_{SE} during the early stage of the experiments. However, in the setup of our target station, the pickup coils are included inside the heating oven. The heat on the pickup coils changes their resistance and inductance. As a result, one has to normalize the pickup coils response under different temperatures in order to calibrate the absolute ^{3}He polarization. This is one reason that all the measurements were performed on double-chamber cells.

For a double-chamber cell, the ^{3}He polarization relaxation rates are not the same in the two chambers, when the upper chamber is hot and the bottom cell is at room temperature, since the potassium vapor is confined to the upper chamber.

One basic observation for the double-chamber cells is that although the ^{3}He polarization relaxes at different rates in the two chambers, the value of ^{3}He polarization can be regarded as uniform over the whole cell. For a cell with less than 1 atmosphere of ^{3}He, the diffusion time constant of ^{3}He inside the cell is about 10 minutes. This is much shorter than the ^{3}He polarization relaxation rate of $\sim$ 10 hours. This fact can be used to model the ^{3}He polarization relaxation in a hot double-chamber cell as follows.

Studying a single ^{3}He atom in the cell, the ^{3}He nucleus will lose its spin orientation by collisions with the cell walls. If this ^{3}He atom is located in the upper chamber, it will also lose its spin orientation by spin-exchange collisions with the potassium atoms. The probability that this atom is in the upper chamber is $N_{He}^{upper}/N_{He}^{cell}$, where N stands for the ^{3}He atom total number. In a double-chamber cell, the averaged spin destruction rate for a ^{3}He atom is

$$\gamma_{SE}\frac{N_{He}^{upper}}{N_{He}^{cell}}+\Gamma, \tag{5.13}$$

where we assume the wall relaxation rate Γ in the upper chamber and in the bottom chamber is the same.

Compared to Equation 5.13, a factor of

$$R_d \equiv \frac{N_{He}^{upper}}{N_{He}^{cell}} = \frac{1}{1+\frac{V_b}{V_u}\frac{T_u}{T_b}} \tag{5.14}$$

has to be applied for a double-chamber ^{3}He cell. In Equation 5.14, V is the chamber volume, T is the corresponding temperature, and the indexes u and b stand for upper chamber and bottom chamber, respectively. Explicitly, the ^{3}He polarization relaxation rate is

$$R_d\gamma_{SE}+\Gamma = R_d[K]\cdot k_{SE}+\Gamma. \tag{5.15}$$

Plotting the hot ^{3}He polarization relaxation rates as a function of $R_d[K]$, the spin-exchange rate coefficient k_{SE} can be found from the slope, and the wall relaxation rate Γ can be found from the intercept.

In the above discussions, it is assumed the cell's wall relaxation rate Γ is independent of the temperature of the glass wall. In Chapter 2, it was discussed that it is true for Pyrex glass (see Equation 2.37 and the discussions therein). It is reasonable to assume that the same is true for the GE-180 glass. One way to test this assumption is to compare the Γ measurements at high temperatures to the direct measurements of ^{3}He polarization relaxation rates at room temperature. The data presented in the following sections show that the measured Γ agrees well with the direct measurements. The good linearity of the fit also indicates that Γ is insensitive to temperature changes for our target cells.

5.2.3 Alkali Metal Vapor Density Determinations

5.2.3.1 Vapor Pressure Formulae

Knowing the potassium vapor density is critical for the calculation of the spin-exchange rate coefficient k_{SE} in Equation 5.15. During the experiments, the cell's temperature was monitored by several RTDs. Following the potassium vapor pressure formula, the potassium vapor pressure was taken from the temperature readings. The potassium number density is related to the pressure by the ideal gas law $n = P/k_BT$.

The alkali vapor pressure formulae taken in this work come from the Killian formulae for rubidium and potassium [4] and the cesium formula from Reference [11]:

$$\log_{10} P_{Rb} = 9.55 - 4132/T \tag{5.16}$$

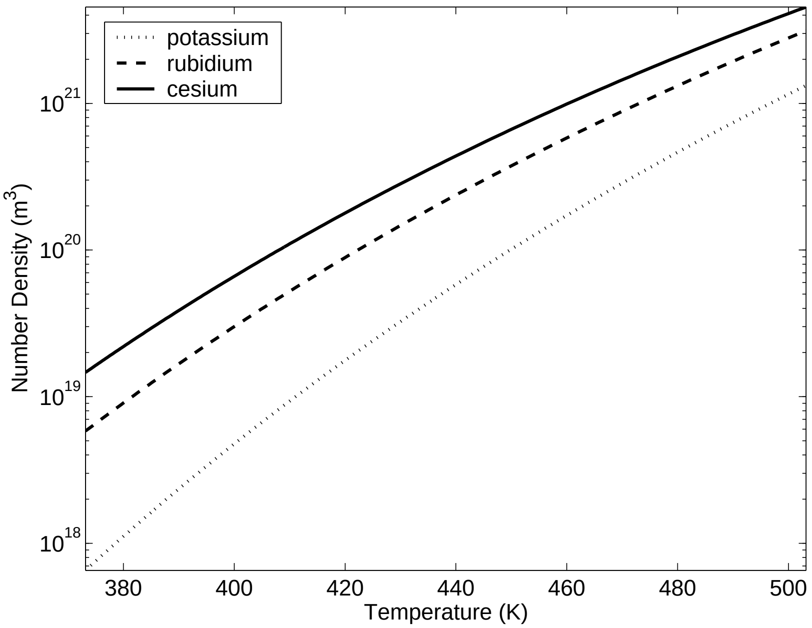

Figure 5.6: Alkali vapor densities as functions of temperature. The rubidium and potassium formulae are from Reference [4] and the cesium formula is from Reference [11].

$$\log_{10} P_K = 10.83 - -4964/T \tag{5.17}$$

$$\log_{10} P_{Cs} = 13.1781 - 4041/T - 1.35 \log_{10} T, \tag{5.18}$$

where P is in Pa and T is in Kevin.

Figure 5.6 shows the alkali metal vapor densities as functions of the vapor temperature. In order to have the same number density as rubidium at $\sim 180 - 200$°C, which is the working temperature for typical rubidium-^{3}He targets experiments, the temperature of the potassium has to be $20 - 30$°C higher.

The alkali metal vapor pressure formulae are widely used in the spin-exchange optical pumping ^{3}He community. However, recently some groups have claimed that these formulae do not agree well with the true alkali metal number densities [69, 78]. The alkali metal number density depends on the individual cell surface and efforts to find a uniform empirical pressure formula failed for these groups.

To find out whether the alkali metal vapor pressure formulae are applicable to the individual cells in our lab, measurements were performed in two different potassium-^{3}He cells, and the results were compared. Also, for the rubidium-^{3}He cells, results were obtained in our lab and compared with the published k_{SE} measurements. Basically, we observed that different cells produce the same results when using the same alkali metal vapor pressure formula as discussed in the following subsections.

5.2.3.2 Direct Vapor Density Measurements by the Faraday Rotation Method

Direct alkali metal number density measurements were also performed in our lab using a Faraday rotation method to further test the applicability of the vapor pressure formulae [86]. In the work of [86], for each alkali metal vapor, namely, rubidium, potassium and cesium, two 1 inch diameter 3 inch length cells were made, one from GE-180 glass and one from Pyrex. The vapor atom number densities at different temperatures in the different cells were measured directly and compared to the empirical formulae. No cell to cell vapor density variations were observed at the same temperature.

The Faraday rotation measurements detect the Faraday rotation angle of an incident linear polarized probe laser light. The probe light passes through the target cell along the direction of the holding magnetic field. Since the alkali metal vapor inside the cell is circularly birefringent, the linear polarization plane of the probe light will rotate by an angle, which is proportional to the alkali metal vapor density.

The Faraday rotation angles are very small for our experimental conditions. For the holding magnetic field $B_z \sim 40$ Gauss and with an alkali metal number density on the order of 10^{14} cm^{-3} (corresponding to a temperature $\sim 200°$C), a typical rotation angle is $\sim 0.5°$. The angle was detected by a lock-in detection scheme using a photoelastic modulator (PEM) (Hinds Instruments, model PEM90-I/FS50), a photodiode (PD) detector and a lock-in amplifier. The PEM is a birefringent medium which oscillates at a frequency of $f = 50$ kHz. After the incident light passing the PEM, the net circular polarization component of the transmission light produces a signal in the PD at the modulator frequency f(50 kHz), and the net linear polarization component produces a signal at $2f$ (100 kHz). Therefore, all four Stokes parameters of the incident light can be measured by lock-in detection and the rotation angle can be determined with high sensitivity. The rotation angles were measured at different wavelengths of the probe light at the same temperature, then a fit of the angles versus the wavelengths gives the measured alkali vapor density. Figure 5.7 shows the optical experimental setup for the Faraday rotation measurements.

For the work in Reference [86], the fits show that for each alkali metal, the densities in the two cells are the same at the same temperature. However, it is possible that the contaminants in the cell walls and in the alkali metals could change the vapor pressure relations noticeably. Fabrication and alkali metal filling procedures could be responsible for this difficulty arising in the vapor density determination [69, 78]. In this thesis work, the vapor pressure method is still adopted for the determination of alkali metal vapor densities, since we found no evidence for a violation of the vapor

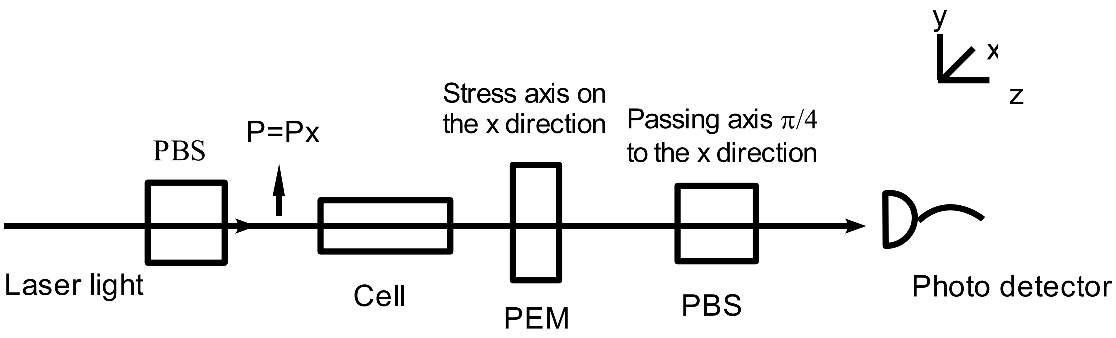

Figure 5.7: Setup for Faraday rotation measurements. The first PBS is used to obtain horizontally polarized probe light. The axis of the second PBS is set at 45° compared to the stress axis of the PEM. The photo detector records the transmitted light at the PEM frequency f and at a frequency of $2f$.

pressure formulae for our cells.

5.2.4 Calculations of Spin-exchange Rate Coefficients

The ^{3}He polarization relaxation rates at different temperatures were measured as discussed in previous sections to find the spin-exchange rate coefficients k_{SE}. Figure 5.8 shows one of the actual hot ^{3}He polarization relaxation curves obtained from a potassium-^{3}He cell, which is the same cell used in Figure 5.5. The fit in Figure 5.8 shows a ^{3}He polarization relaxation time constant of $(\gamma_{SE}+\Gamma)^{-1} = 9 \pm 0.3$ hours at 230°C. The temperature fluctuations were stabilized to within ±1°C.

Combining the fits of $\gamma_{SE}+\Gamma$ from Figure 5.8 and Γ from Figure 5.5, we can derive the potassium-^{3}He spin-exchange rate coefficient k_{SE} at 230°C to be

$$k_{SE} \equiv \frac{\gamma_{SE}}{R_d[K]} = (3.9 \pm 0.2) \times 10^{-20}\mathrm{cm}^3/\mathrm{sec}, \qquad (5.19)$$

where $R_d = 0.506$ is the correction factor for the double-chamber geometry as shown

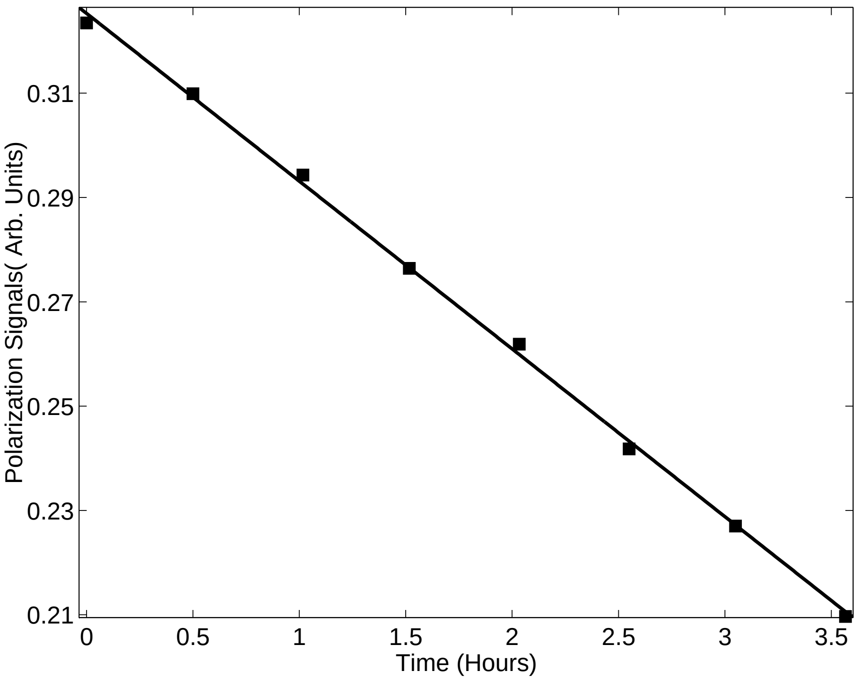

Figure 5.8: The ^{3}He spin polarization relaxation curve for a potassium-^{3}He cell at 230°C. The fit shows a polarization relaxation time constant $(\gamma_{SE} + \Gamma)^{-1} = 9 \pm 0.3$ hours.

in Equation 5.14. The potassium number density $[K] = 1.326 \times 10^{21}\text{m}^{-3}$ is calculated from the Killian vapor pressure Formula 5.18. The uncertainties are largely due to the potassium number density variation caused by temperature fluctuations.

The spin-exchange rate coefficient k_{SE} measurement in Equation 5.19 is based on two assumptions. First, the wall relaxation rate Γ measured at room temperature is the same at high temperatures, and second, the potassium number density inferred from the vapor pressure formulae is accurate. Neither assumptions can be taken for granted. Therefore, during the experiments, for each cell, the ^{3}He polarization relaxation rates at different temperatures are measured. Figure 5.9 shows the measured $\gamma_{SE} + \Gamma$ at several temperatures ranging from 177°C to 230°C. The ^{3}He polarization relaxation rates show excellent linearity with the potassium densities calculated from

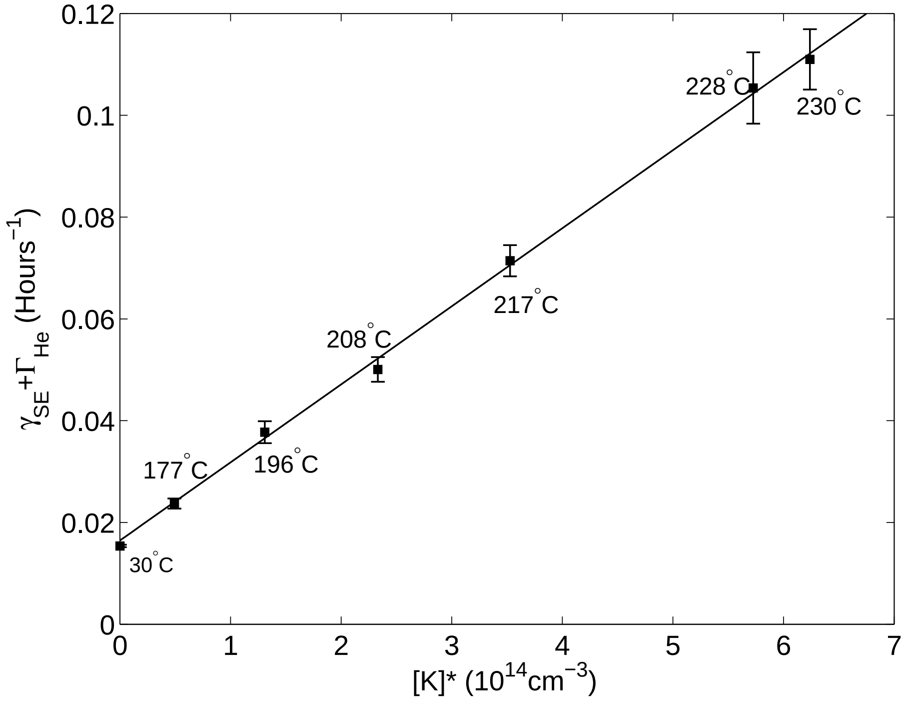

Figure 5.9: The ^{3}He spin polarization relaxation rates for a potassium-^{3}He cell as a function of $[K]^*$, where $[K]^* = R_d[K]$ and $[K]$ is the density of potassium, $R_d \equiv N_{He}^{top}/N_{He}^{cell}$, N_{He}^{top} is the number of ^{3}He atoms in the top chamber, and N_{He}^{cell} is the total number of ^{3}He atoms in the cell. The listed temperatures correspond to the temperature in the top chamber of the cell. Systematic uncertainties, coming primarily from the uncertainty in the temperature measurement, are included in the error bars, and therefore the uncertainties are correlated.

the Killian vapor pressure formula.

Assuming that the ^{3}He polarization wall relaxation rate in the cell, $1/\Gamma_{He}$, is approximately a constant for the temperature range of 177°C to 230°C, then $1/\Gamma_{He}$ can be read out as 61 ± 16 hours from Figure 5.9. This is consistent with the cold ^{3}He polarization relaxation measurements, but less accurate. From the slope of the line in Figure 5.9, the spin-exchange rate coefficient at a temperature of 197°C was found to be

$$k_{SE} \equiv \frac{\gamma_{SE}}{[K]} = (4.0 \pm 0.3) \times 10^{-20}\,\mathrm{cm}^3/\mathrm{sec}. \tag{5.20}$$

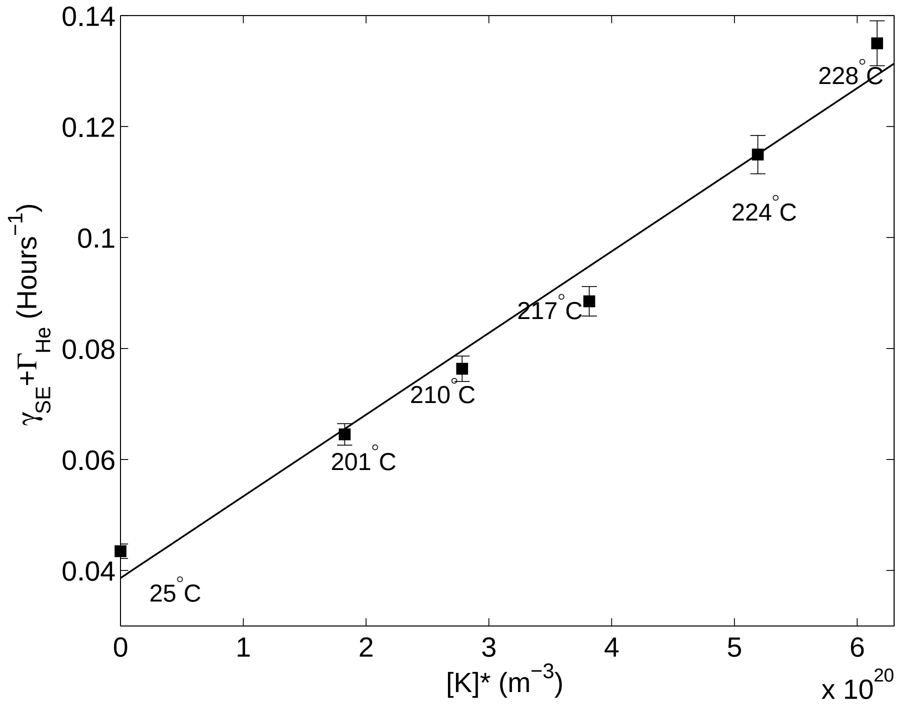

Figure 5.10: The ^{3}He spin polarization relaxation rates measurements for a second potassium-^{3}He cell.

As discussed in Chapter 2, the spin-exchange rate coefficient k_{SE} has a temperature dependence in the form of $1/\sqrt{T}$. This brings in a small correction (3% relative) on the x-axis in Figures 5.9 and has been accounted for when performing the fit.

Figure 5.10 shows the spin-exchange rate coefficient k_{SE} measurements for a second potassium-^{3}He cell.

The spin-exchange rate coefficient calculated from Figure 5.10 is

$$k_{SE} \equiv \frac{\gamma_{SE}}{[K]} = (4.1 \pm 0.3) \times 10^{-20}\,\mathrm{cm}^3/\mathrm{sec}, \tag{5.21}$$

which agrees well with Equation 5.20.

Using the same method, the spin-exchange rate coefficient of cesium-^{3}He pair has

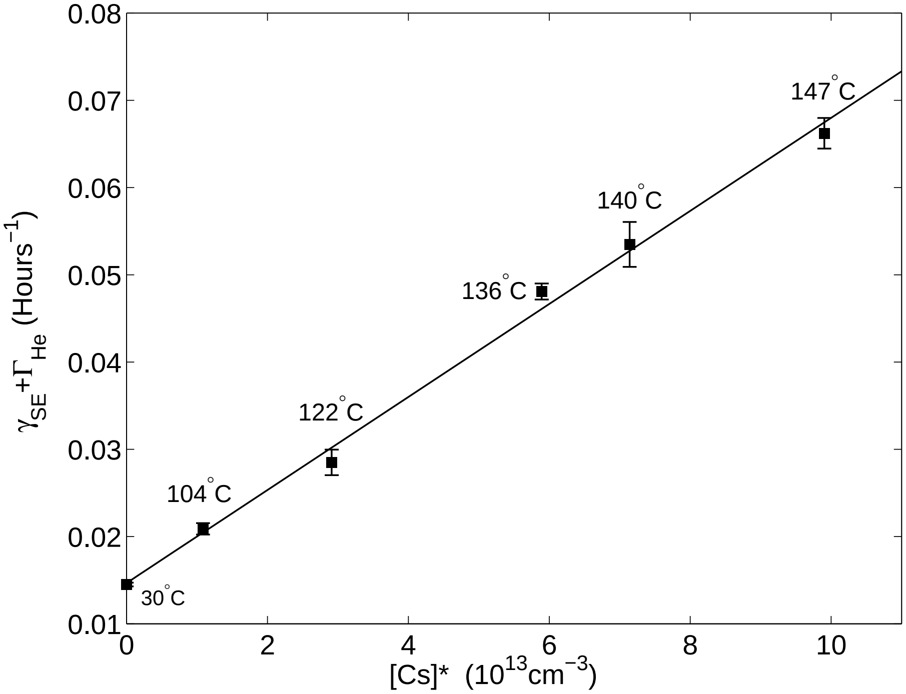

Figure 5.11: The ^{3}He spin polarization relaxation rates measurements for a cesium-^{3}He cell.

also been measured for a cesium-^{3}He double-chamber cell in the temperature range of 100°C to 150°C as shown in Figure 5.11.

The cesium-^{3}He spin-exchange rate coefficient is found from Figure 5.11 to be

$$k_{SE} \equiv \frac{\gamma_{SE}}{[Cs]} = (13.6 \pm 1.3) \times 10^{-20}\,\mathrm{cm}^3/\mathrm{sec}. \tag{5.22}$$

The cell used in Figure 5.11 has a ^{3}He polarization wall relaxation time constant of 69 ± 1 hours measured at room temperature. The hot ^{3}He polarization wall relaxation time constant comes from the intercept in Figure 5.11 is found to be 68 ± 13 hours. The results agrees well with each other.

The spin-exchange rate coefficient for rubidium-^{3}He pair has been measured before by several groups [45, 31, 69]. A rubidium-^{3}He cell measurement has also been performed in our lab, and a value for the Rb/He spin-exchange coefficient at a temperature of 171°C is found to be

$$k_{SE} \equiv \frac{\gamma_{SE}}{[Rb]} = (0.65 \pm 0.04) \times 10^{-19}\,\mathrm{cm}^3/\mathrm{sec}, \tag{5.23}$$

The rubidium results agree well with previous measurements [69].

In conclusion, the results from Equations 5.21, 5.22 and 5.23 show that the spin-exchange rate coefficients for potassium-^{3}He, rubidium-^{3}He and cesium-^{3}He pairs are of the same order of magnitude and they satisfy

$$k_{SE}(K -^3 He) < k_{SE}(Rb -^3 He) < k_{SE}(Cs -^3 He) \tag{5.24}$$

as predicted by theoretical studies [41]. Recalling that the alkali metal atom spin destruction coefficients have the relationship

$$k_{SD}(K) \ll k_{SD}(Rb) \ll k_{SD}(Cs) \tag{5.25}$$

as shown in Table 2.1, it is indicated that potassium-^{3}He pair are more efficient than rubidium-^{3}He and cesium-^{3}He pairs for spin-exchange optical pumping. This prediction is in agreement with the high ^{3}He polarization results achieved in the potassium-^{3}He cells in this thesis work.

Chapter 6

Conclusion

6.1 Conclusion

Spin-exchange optical pumping using potassium rather than rubidium as the polarizing agent offers the possibility of obtaining higher ^{3}He polarizations using substantially lower laser power. The high ^{3}He polarization achieved in the potassium-^{3}He cells reported in this thesis work is the first successful attempt to realize a practical potassium-^{3}He target which have comparable performance with traditional rubidium-^{3}He system using less laser power. Our work motivates further researches on the building of high-pressure polarized ^{3}He targets and on the development of high power lasers at the potassium D1 wavelength, namely, 770 nm.

The measured spin-exchange rate coefficients of potassium-^{3}He pairs, rubidium-^{3}He pairs and cesium-^{3}He pairs agree with theoretical predictions discussed in Chapter 2. The rubidium-^{3}He results are also in agreement with previous measurements conducted by other groups. By the time of this thesis writing, no cesium-^{3}He spin-exchange rate coefficients measurements have been measured.

6.2 Future Work

For future polarized ^{3}He studies, it is important to improve the precision of the rate coefficient measurements. It would be beneficial, for example, to try to polarize a high-pressure ^{3}He cell with potassium using a diode laser.

It is possible that the efficiency of the diode laser may be different from that of the Ti:Sapphire laser, since the D1 line and D2 line of potassium are closer than that of rubidium. The commercial diode laser has a wide bandwidth, therefore, it is likely that a significant fraction of the laser power will be absorbed by the potassium D2 line during spin-exchange optical pumping. The efficiency for the D1 line will then be decreased. For the same reason, due to pressure broadening, the high-pressure potassium-^{3}He cell may have a worse performance than the one atmosphere cells studied in this thesis.

The performance of high-pressure potassium-^{3}He cells pumped by diode lasers at the potassium D1 line can be estimated based on the relevant spin destruction and spin-exchange rate coefficients characterized in this thesis work.

For comparison, consider a typical rubidium-^{3}He high-pressure double-chamber target cell in SLAC 154 experiment. It contained 9 amagats of ^{3}He with a lifetime of 85 hours. About 50% ^{3}He polarization was achieved after several days of pumping using three diode laser arrays (15 watts each, FWHM 2-4 nm) and four Ti:sapphire lasers (5 watts each, FWHM $<$ 40 GHz) [44].

If we construct a potassium-^{3}He cell at the same ^{3}He density, the potassium D1 linewidth is dominated by pressure broadening up to 0.5 nm. (The potassium D1 line broadening is about 30 GHz/amagats [5], which is larger than the rubidium D1 line broadening.) Suppose we use commercial diode laser arrays at 770 nm with 2 nm spectral width. Then, $\sim 20\%$ laser power will be absorbed by the cell with optically thick potassium vapor. (For a Gaussian laser beam profile with 2 nm width, the 0.5 nm K D1 line width occupies a ratio of $1/\sqrt{\pi} \cdot \int_{-0.25 \ln 2}^{0.25 \ln 2} e^{-x^2} dx = 0.2$.)

The spin destruction rates due to collisions with gas atoms are proportional to the density of that gas. For the rubidium case, the experimental values of Rb-Rb and Rb-He spin destruction rate coefficients are given in Table 2.1. They contribute similarly to the Rb spin destruction rate Γ_{SD} for a 9 amagats ^{3}He cell. For the potassium case, the K-K spin destruction cross section was measured to be one order of magnitude smaller than that of Rb-Rb, and the theoretical estimate for the K-He spin destruction cross section is also one order of magnitude smaller than Rb-He's [41]. Judging by these results, we expect that the potassium density, rather than the ^{3}He density, will dominate in affecting Γ_{SD} for a 9 amagats potassium-^{3}He cell. The high-pressure cell should not be very different from a 1 atmosphere cell with regard to the potassium spin destruction rate at the same temperature.

For a typical potassium-^{3}He cell as presented in this thesis work, 5 watts of laser power operating for 60 hours results in a 46% polarization. We expect a diode laser arrays at 25 watts should be able to pump the high-pressure cell to several-tens of percent of ^{3}He polarization on the same time scale, which would be very efficient both in time and in terms of laser power consumption.

In addition, the diode laser spectral width can be narrowed by using reflection feedback from an etalon as demonstrated in the rubidium-^{3}He studies from Reference [81]. This technique can significantly increase the laser power available for potassium optical pumping.

Based on the above discussions, we estimate that a single 30 watts diode laser tuned to the potassium D1 line should be adequate to polarize the ^{3}He gas at high pressures (∼10 atmospheres) and large volumes (∼liters) to values of ∼50%.

The highly polarized ^{3}He gas have important applications in both fundamental nuclear physics and in medical imaging as introduced in Chapter 1. With better performance, the potassium-^{3}He system can supersede the traditional rubidium-^{3}He systems and further benefit the polarized noble gas user community. One potential future application of highly polarized potassium-^{3}He system is the production of polarized beams of ^{3}He used in colliders to study the neutron spin structure at high energies.

In the field of high energy nuclear physics, future studies of the internal spin structure of the proton and neutron will require even higher energy beams than can be produced by present-day fixed target experiments. The next step will be to study proton and neutron spin structure at collider facilities. A program to study the proton spin structure using polarized proton collisions at center of mass energies of 200 to 500 GeV is already active at Brookhaven National Laboratory [83, 84], and studies to develop a new facility to collide polarized electrons with polarized protons are ongoing [74]. However, at present, little attention is devoted to developing programs to learn about neutron spin structure in a high-energy collider environment.

Accelerator physics considerations on how to operate a polarized ^{3}He and deuteron beams for a collider program have been briefly studied [52]. One of the requirements for the operation and development of a polarized ^{3}He beam source would be the continuous production of large volumes of highly polarized ^{3}He. A likely scenario is that the polarized ^{3}He beam source will use spin-exchange collisions with optically pumped alkali vapor as the technique for the polarization process, since large volumes of polarized gas would be needed. However, the optical pumping efficiency, polarization optimization, and adaptation of the technique for accelerator beam operation will need to be improved compared to what exists using today polarized ^{3}He targets from rubidium spin-exchange collisions. In particular, high polarizations will be needed in order to have sufficient statistical precision on the polarized neutron measurements. The potassium-^{3}He system could be critical for the success of these future experiments.

For the storage of a polarized beam of ^{3}He in a collider facility, it is estimated that one will only need to produce on the order of 10^{-5} liters per hour of highly polarized ^{3}He ions at one atmosphere pressure in order to reach source currents comparable to the existing polarized proton beams planned in the future RHIC spin program [68]. In this thesis work, we have achieved a reasonably high polarization for 140 cc of of ^{3}He at 0.73 atmospheres in 60 hours. Although this ^{3}He number density is many orders of magnitude larger than the 10^{-5} liters per hour needed, the conversion and transport efficiency of polarized ^{3}He to a polarized ^{3}He ion beam is unknown. Achieving polarizations greater than $\sim$80% will be needed in order to test the low

x substructure for the neutron spin program competitive with a comparable proton spin program, and to test fundamental QCD predictions such as the Bjorken Sum Rule [14] with a new electron-ion collider [74].

Bibliography

[1] Igor I. Sobelman, *Atomic Spectra and Radiative transitions*, Springer-Verlag, 1992.

[2] J. D. Jackson, *Classical Electrodynamics*, John Wiley & Sons, Inc. 1975.

[3] A. Abragham *Principles of Nuclear Magnetism* (Oxford university Press, Oxford, 1961)

[4] Killian, *Phys. Rev.* **27**, 578(1926)

[5] Shang-yi Ch'en and Makoto Takeo, *Rev. Mod. Phys.* **29**, 20 (1957).

[6] A. Kastler, Optical Methods of Atomic Orientation and of Magnetic Resonance, *J. Opt. Soc. Am.* **47**, 460-465(1957).

[7] L. W. Anderson, F. M. Pipkin and J. C. Barid, *Phys. Rev.* **120**, 1279(1960).

[8] M. A. Bouchiat, T. Carver, C. M. Varnum, *Phys. Rev. Lett.* **5**, 373 (1960).

[9] Morrel H. Cohen and V. Heine, *Phys. Rev.* **122**, 1821 (1961).

[10] S. Meiboom, *Journal of Chemical Physics* **34**, 375 (1961)

[11] A. N. Nesmeyanov, *Vapor Pressure of the Elements* (Academic, New York, 1963).

[12] F. D. Colgerove, L. D. Scheafer, and G. K. Walters, *Phys. Rev.* **132**, 2561 (1963).

[13] R. M. Herman, *Phys. Rev.* **137**, A1062 (1965)

[14] J. D. Bjorken, *Phys. Rev.* **148**, 1467 (1966); Phys. Rev. D **1**, 1376 (1970).

[15] W. A. Fitzsimmons, L. L. Tankersley, and G. K. Walters, *Phys. Rev.* **179**, 156 (1969).

[16] R.V. Damadian, *Tumor Detection by Nuclear Magnetic Resonance. Science*, March 19, 1971.

[17] William Happer, *Rev. Mod. Phys.* **44**, 169 (1972).

[18] J. Ellis and R. Jaffe, *Phys. Rev. D* **9**,1444(1974)

[19] H. Soboll, *Phys. Lett.* **41A**, 373 (1972)

[20] J. Ashman *et al.*, *Phys. Lett.* **B206**, 364 (1988)

[21] X. Zeng, Z. Wu, T. Call, E. Miron, D. Schreiber and W. Happer, *Phys. Rev. A* **31**, 260 (1985).

[22] Z. Wu, T. G. Walker and W. Happer, *Phys. Rev. Lett.* **54**, 1921 (1985).

[23] W. Happer and W. A. Van Wijngaarden, "An optical pumping primer", *Hyperfine Interactions* **38**, (1987) 435-470

[24] T. G. Walker, K. Bonin, and W. Happer, *Phys. Rev. A* **35**, 3749 (1987).

[25] T. E. Chupp, M. E. Wagshul, K. P. Coulter, A. B. McDonald, and W. Happer, *Phys. Rev. C* **36**, 2244 (1987).

[26] C. G. Cates, S. R. Schaefer and W. Happer, *Phys. Rev. A* **37**, 2877(1988).

[27] M. E. Wagshul, T. E. Chupp *Phys. Rev. A* **40**, 4447 (1989).

[28] Thad G. Walker, *Phys. Rev. A* **40**, 4959 (1989).

[29] R. J. Knize, *Phys. Rev. A* **40**, 6219 (1989).

[30] J. L. Friar, B. F. Gibson, G. L. Payne, A. M. Bernstein, T. E. Chupp, *Phys. Rev.* **C42**, 2310 (1990).

[31] B. Larson, O. Hausser, P. P. J. Delheij, D. M. Whittal, and D. Thiessen, *Phys. Rev. A* **44**, 3108 (1991).

[32] M. E. Wagshul, Ph. D. thesis, Harvard University, 1992.

[33] P. L. Anthony *et al.*, *Phys. Rev. Lett.* **71**, 959 (1993).

[34] N. R. Newbury, A. S. Barton, G. C. Cates, W. Happer, and H. Middleton, *Phys. Rev. A* **48**, 4411 (1993).

[35] M. E. Wagshul, T. E. Chupp *Phys. Rev. A* **49**, 3854 (1994).

[36] H. L. Middleton, Ph. D. thesis, Princeton University, 1994.

[37] H. Gao *et al.*, *Phys. Rev.* **C50**, 546 (1994).

[38] M. S. Albert,G. D. Cates,B. Driehuys, W. Happer, B. Saam, C. S. Springer, and A. Wishnia, *Nature* **370**, 199 (1994).

[39] W. J. Cummings, O. Hausser, W. Lorenzon, D. R. Swenson and B. Larson *Phys. Rev. A* **51**, 4842 (1995).

[40] P. L. Anthony *et al.* (SLAC E142 Collaboration), *Phys. Rev.* **D54**, 6620 (1996).

[41] Thad G. Walker, William Happer, *Rev. Mod. Phys.* **69**, 629 (1997).

[42] T. Walker, J. H. Thywissen and W. Happer, *Phys. Rev. A* **56**, 2090 (1997).

[43] K. Abe et al. (SLAC E154 Collaboration), *Phys. Rev. Lett.* **79**, 26 (1997).

[44] M. V. Romalis, Ph. D. thesis, Princeton University, 1997.

[45] A. B. Baranga, S. Appelt, M. V. Romalis, C. J. Erickson, A. R. Young, G. D. Cates, and W. Happer, *Phys. Rev. Lett.* **80**, 2801 (1998).

[46] S. Appelt, A. B. Baranga, C. J. Erickson, M. V. Romalis, A. R. Young, and W. Happer, *Phys. Rev. A* **58**, 1412 (1998).

[47] S. Kadlecek, L. Anderson, and T. Walker, *Nucl. Instrum. Methods Phys. Res. A* **402**, 208 (1998).

[48] P. Leo, E. Tiesinga, P. Julienne, D. K. walter, S. Kadlecek and T. Walker, *Phys. Rev. Lett.* **81**, 1389 (1998).

[49] A. Ben-Amar Baranga, S. Appelt, C. J. Erickson, A. R. Young, and W. Happer, *Phys. Rev. A* **58**, 2282(1998).

[50] Sebastien Incerti and Enkeleida Lakuriqi, E94010 Technical Note 10, Jefferson Lab, 1998

[51] D. K. Walter, W. Happer and T. G. Walker, *Phys. Rev. A* **58**, 3642 (1998).

[52] E. D. Courant, Brookhaven National Lab internal report, BNL-65606 (1998).

[53] D. Rohe *et al.*, *Phys. Rev. Lett.* **83**, 4257 (1999).

[54] Jaideep Singh, B. S. thesis, California Institute of Technology, 2000.

[55] M. V. Romalis, *Appl. Phys. Lett.* **77**, 1080 (2000).

[56] E. W. Hughes and R. Voss, *Ann. Rev. Nucl. Part. Phys.* **85**, 2900 (2000) and references therein.

[57] Ming F. Hsu, G. D. Cates and I. Kominis, I. A. Aksay and D. M. Dabbs *Appl. Phys. Lett.* **77**, 2069 (2000).

[58] C. J. Erickson, D. Levron, W. Happer, S. Kadlecek, B. Chann, L. W. Anderson and T. G. Walker, *Phys. Rev. Lett.* **85**, 4237 (2000).

[59] W. Xu *et al.*, *Phys. Rev. Lett.* **85**, 2900 (2000).

[60] W. Happer, G. D. Cates, M.V. Romalis, and C. J. Erickson, U.S. Patent No. 6 318 092 (2001).

[61] E. Vliegen, S. Kadlecek, L. Anderson, T. Walker, C. J. Erickson and W. Happer *Nucl. Instrum. Methods A* **460**, 444 (2001).

[62] S. Kadlecek, T. Walker, D. K. Walter, C. Erickson, and W. Happer, *Phys. Rev. A* **63**, 052717 (2001).

[63] R. E. Jacob, S. W. Morgan, and B. Saam, J. C. Leawoods *Phys. Rev. Lett.* **87**, 143004 (2001).

[64] F. Xiong *et al.*, *Phys. Rev. Lett.* **87**, 242501 (2001).

[65] P. A. Mastromarino, C. R. Otey, D. Pripstein and E. W. Hughes, *Nucl. Instrum. Methods B* **194**, 69 (2002).

[66] W. Shao, G. Wang, R. Fuzesy, E. W. Hughes, B. A. Chronik, G. C. Scott, S. M. Conolly, and Albert Macovski, *Applied Physics Letters* **80**,2032(2002)

[67] D. K. walter, W. M. Griffith and W. Happer, *Phys. Rev. Lett.* **88**, 093004 (2002)

[68] H. Huang *et al.*, "Polarized Proton Acceleration at the Brookhaven AGS - An Update", *Proc. of EPAC 2002*, Paris, France, p. 335.

[69] B. Chann, E. Babcock, L. W. Anderson and T. Walker, *Phys. Rev. A* **66**, 032703 (2002).

[70] B. Chann, E. Babcock, L. W. Anderson, and T. G. Walker, *Phys. Rev. A* **66**, 033406 (2002).

[71] Salerno M., de Lange E. E., Altes T. A., Truwit J. D., Brookeman J. R., Mugler III J. P. *Radiology* **222**, 252-260 (2002).

[72] Yuan-Yu Jau, Nicholas N. Kuzma and William Happer, *Phys. Rev. A* **66**, 052710 (2002).

[73] T.W. Kornack and M.V. Romalis, *Phys. Rev. Lett.* **89**, 253002-1 (2002).

[74] R. Holt *et al.*, The Electron Ion Collider, Brookhaven National Lab report, BNL-68933, February 2002.

[75] R. E. Jacob, S. W. Morgan, and B. Saam, *Journal of Applied Physics* **92**, 1588 (2002).

[76] R. E. Jacob, B. Driehuys, and B. Saam, *Chem. Phys. Lett.* **370**, 261-267 (2003).

[77] G. Wang, W. Shao and E. W. Hughes, ”Polarizing Helium-3 by Spin-Exchange Collisions with Potassium and Cesium”, American Physics Society, the Division of Atomic, Molecular and Optical Physics (DAMOP) Meeting, May 2003

[78] Yuan-Yu Jau, Nicholas N. Kuzma and William Happer, *Phys. Rev. A* **67**, 022720 (2003).

[79] Tina Pavlin, Ph. D. thesis, California Institute of Technology, 2003.

[80] E. Babcock, I. A. Nelson, S. Kadlecek, B. Driehuys, L. W. Anderson, F. W. Hersman, and T. G. Walker, *Phys. Rev. Lett.* **88**, 123003 (2003).

[81] B. Chann, E. Babcock, L. W. Anderson, T. G. Walker, W. C. Chen, T. B. Smith, A. K. Thompson, and T. R. Gentile, *Journal of Applied Physics*, **94**, 6908, 2003

[82] K. Ackerstaff *et al.* (HERMES Collaboration), *Phys. Lett.* **B404**, 383 (1997).

[83] G. Bunce, N. Saito, J. Soffer, W. Vogels ang, *Ann. Rev. Nucl. Part. Sci.* **50**, 525 (2000) and references therein.

[84] G. Bunce *et al.*, *Particle World*, **3**, 1 (1992).

[85] G. Schmidt, *Lecture notes*, the University of Arizona, 2003.

[86] Wenjin Shao, Ph. D. thesis, California Institute of Technology, 2004.

Appendix A

Low-Field MRI of Hyperpolarized Noble Gas and Water in A Single System

This is a reprint of a Letter on the experimental studies of building a low-field laser-polarized noble gas MRI system. Collaborated with Stanford, we combined the laser-polarized noble gas MRI technique and a low-field MRI technique, namely, Pre-polarized MRI, images of gaseous polarized ^{129}Xe and water cells at room temperature were obtained with a low-field magnetic resonance scanner. This potentially low-cost imaging technique offers the possibility of high-resolution imaging using both polarized noble gas and proton MRI of tissues in the same scanner.

APPLIED PHYSICS LETTERS VOLUME 80, NUMBER 11 18 MARCH 2002

Low readout field magnetic resonance imaging of hyperpolarized xenon and water in a single system

Wenjin Shao, Guodong Wang, Raymond Fuzesy, and Emlyn W. Hughes[a)]
Kellogg Radiation Laboratory, Division of Physics, Math, and Astronomy, California Institute of Technology, Pasadena, California 91125

Blaine A. Chronik, Greig C. Scott, Steven M. Conolly, and Albert Macovski
Magnetic Resonance Systems Research Laboratories, Department of Electrical Engineering, Stanford University, Stanford, California 94305

(Received 5 December 2001; accepted for publication 23 January 2002)

Using a low-field magnetic resonance scanner, we have obtained images of gaseous polarized ^{129}Xe and water cells at room temperature. This potentially low-cost imaging technique offers the possibility of high-resolution imaging using both polarized noble gas and proton magnetic resonance imaging of tissues in the same scanner.
[DOI: 10.1063/1.1459759]

Magnetic resonance imaging (MRI) is an imaging technique in which a nuclear magnetic resonance (NMR) signal is obtained from a sample within an external magnetic field.[1] In normal MRI, the equilibrium magnetization in the sample and the amplitude and frequency of the induced voltage in the receive coil are proportional to the strength of the main, static field. There are, however, two methods of MRI in which the magnetization is not directly related to the magnetic field used to collect the signal: hyperpolarized gas imaging[2,3] and prepolarized MRI (PMRI).[4,5] In the first case, a hyperpolarized gas is produced through spin–exchange optical pumping of a polarized noble gas[6] such as ^{3}He and ^{129}Xe in the presence of a weak magnetic field. The polarized gas is then introduced into the biological system of interest, for example, the lungs,[7] and images are obtained based on the NMR signal from the gas magnetization. In the case of PMRI, magnetization is produced in the sample using a strong (~1 T) but not very uniform (~20%) magnet which is subsequently and very rapidly switched off (after ~40 ms). The magnetization is then detected in the presence of a weak (~30 mT) but uniform (~10 ppm) field. These two methods share the capability to read out the NMR signals in the presence of very low fields while still having magnetizations typical of high fields. The combination of these two approaches should allow the investigation of proton signals in tissues at both low and high fields using PMRI, and at low fields using hyperpolarized noble gas, on the same sample, in the same system. In this letter, we present preliminary ^{129}Xe and proton images obtained with our prototype system.

Hyperpolarized xenon images were obtained first by polarizing the sample of ^{129}Xe in the laser system and then carrying the polarized cell into the PMRI scanner for imaging. Figure 1 shows a schematic of the experimental setup.

The polarized xenon cell used in this study was made of uncoated Pyrex and was spherical in shape. The cell had an inner diameter of 2 cm and a wall thickness of a few millimeters. After baking overnight on a high vacuum system (10^{-7} Torr) similar in design to filling stations used in the production of polarized targets,[8] the cell was filled with a mixture of 0.57 amagat of natural abundance xenon, 0.13 amagat of N_2, and a few droplets of rubidium. The cell was sealed and removed from the system by glass blowing the Pyrex tube connecting the cell to the vacuum system.

The cell was placed between a pair of 50 cm diam Helmholtz coils, whose central field (45 mT) acts as a holding field during the polarization process. A heat gun warmed the cell to approximately 100 °C, so that a sufficient rubidium (Rb) vapor density (on the order of 10^{-4} amagats) was present for the optical pumping process. A 30 W Coherent

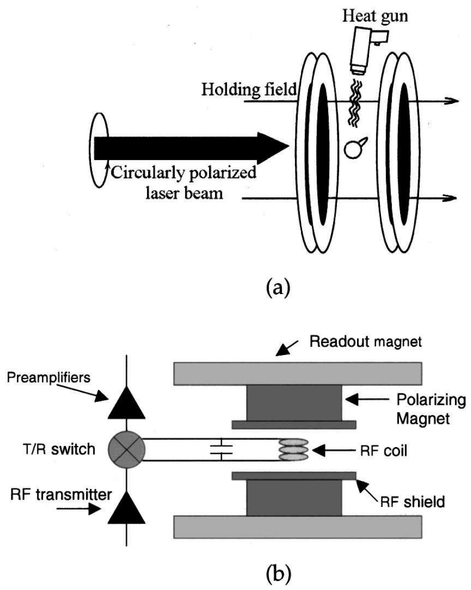

FIG. 1. (a) Schematic of the experimental setup used for polarizing the xenon cell. Circularly polarized laser light impinged upon the xenon cell, which is located within a pair of Helmholtz coils. The cell was heated to approximately 100 °C with a heat gun. (b) Schematic of the PMRI system. The sample was placed within a solenoid rf coil after being removed from the polarizing apparatus. The polarizing magnet was only necessary for the water imaging and was not activated during the xenon experiments.

[a)] Electronic mail: emlyn@its.caltech.edu

diode laser (FAP-System™), was circularly polarized and tuned to the Rb $D1$ wavelength (795 nm) to pump the electronic polarization of Rb. The polarized Rb then transfers its polarization to the Xe nuclei via spin–exchange collisions. After approximately 10 min of optical pumping, the cell was manually removed from the holding field, immersed in room temperature water for approximately 5 s to condense the Rb vapor, and then transferred to the imaging system.

The PMRI system was based on the combination of a resistive readout magnet[5] capable of producing fields between 0 and 35 mT and a resistive polarizing magnet producing fields from 0 to 0.3 T. For the ^{129}Xe signal acquisitions, the readout magnet was operated alone at 33.6 mT, corresponding to a ^{129}Xe NMR frequency of 399 kHz. The ^{129}Xe magnetization was excited using a 40° flip angle, thereby allowing several excitations before the cell had to be repolarized in the laser system. To allow estimation of the polarization achieved in the ^{129}Xe cell, a proton signal was collected from a distilled water sample identical in shape and size to the xenon cell, with the magnet at 9.37 mT (399 kHz NMR frequency for water) and using the same rf coil and preamplifier. Proton magnetization was excited using a 90° flip angle. The polarizing magnet was not used during the collection of the calibration water spectra.

^{129}Xe images were acquired using a low flip angle, 2DFT gradient-recalled echo sequence without slice selection. Water images were acquired using a 2DFT gradient echo sequence without slice selection. During water imaging, the polarizing magnet was pulsed on to 0.3 T for 300 ms during each TR recovery interval in order to establish high-field equilibrium magnetization in the sample for each acquisition.

The signal to noise ratios (SNRs) in the proton and ^{129}Xe spectra were estimated to be 5:1 and 20:1, respectively. The absolute polarization of the sample was estimated by comparing the two spectral lines:

$$P_{\mathrm{Xe}}=P_{\mathrm{W}}\frac{\mu_{\mathrm{proton}}}{\mu_{\mathrm{Xe}}}\,\frac{n_{\mathrm{proton}}S_{\mathrm{Xe}}}{n_{\mathrm{Xe}}\,S_{\mathrm{W}}},$$

where P_{Xe} is the xenon polarization, n_{Xe} is the density of ^{129}Xe (only about one fourth of all Xe atoms), n_{proton} is the density of protons in water, μ_{Xe} and μ_{proton} are the nuclear magnetic moments, and S_{Xe} and S_{W} are the signal sizes. P_{W} is the thermal polarization of protons in water, calculated from the Boltzmann distribution. From the NMR signals for xenon and water, polarization of the xenon cell was found to be approximately 4%.

The polarization of the Xe cell used was independently measured in a low field (3 mT) NMR system. Using the identical optical pumping system and xenon cell, the polarization of the xenon cell was estimated to be between 5% and 10% and had a lifetime on the order of 1 min at room temperature.

Figure 2(a) shows the ^{129}Xe image collected. The pull-off seal where the cell was removed from the vacuum system resulted in a small extrusion from the spherical cell, which can be seen in the image. Figure 2(b) shows the image of a similarly shaped and sized spherical water cell collected on the PMRI system.

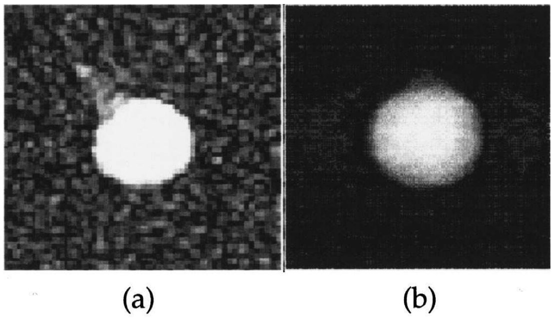
(a) (b)

FIG. 2. (a) 2DFT gradient-recalled echo ^{129}Xe image. The image is magnified to a display field of vision (FOV) of 4 cm×3.5 cm. Imaging parameters: Original FOV = 14.5 cm×10 cm, image matrix = 128×64, zero filled to matrix of 256×256, in plane resolution = 1.13 mm×1.56 mm, readout frequency = 399 kHz, BW = ±2415 kHz, tip angle $(\alpha)=13.5°$, echo time (TE) = 25 ms, repetition time (TR) = 255 ms, total imaging time = 16.3 s. (b) Gradient echo image of a water cell of the same dimensions as the ^{129}Xe cell. Imaging parameters: Original FOV: 10 cm×10 cm, image matrix 64 ×128, readout frequency: 398 kHz, tip angle = 90°, echo time (TE) = 13.6 ms, total imaging time = 10 s.

It has been previously noted[9,10] that, in systems for which the magnetization is independent of the readout field strength, the SNR achievable varies as the readout frequency to the 3/4 power if the dominant source of noise is thermal motion of electrons in the receive circuit (a scenario referred to as "coil noise dominance"). This condition occurs for low readout frequencies. If the readout field is increased, the noise contribution from inductive coupling to the sample (referred to as "body noise") increases relative to the coil noise. As the body noise becomes dominant, the SNR achievable becomes independent of the readout frequency; therefore, no gains in SNR can be obtained through higher readout fields.[5] As the sample and coil are increased in size, the frequency at which body noise dominance occurs decreases. Previous studies have demonstrated that in head-sized coil systems of simple geometry, body noise dominance is achieved at frequencies above approximately 6 MHz.[11] The primary technical challenge for future versions of the scanner system used in this study is to achieve body noise dominance in the receive systems used.

Due to the smaller magnetic moment and lower polarizations, ^{129}Xe images are not yet competitive with those produced using ^{3}He; however, ^{129}Xe has a number of advantages. The spin–exchange cross section for polarizing ^{129}Xe is much larger, and as a result full polarization can be achieved in seconds or minutes, as opposed to several hours for ^{3}He. Natural abundance ^{129}Xe is approximately an order of magnitude cheaper than ^{3}He, which can only be produced as a by-product of tritium decay. Unlike ^{3}He, ^{129}Xe can be frozen at liquid nitrogen temperatures, stored, and transported for use in imaging facilities.[12]

Low-field ^{129}Xe imaging could have advantages over high-field ^{129}Xe applications due to reduced susceptibility effects and therefore smaller depolarizing gradients that affect the spins during imaging. This effect could make low-field ^{129}Xe material studies attractive. It has already been demonstrated that hyperpolarized ^{129}Xe is a potentially powerful probe of porous surfaces.[13–15] Additional low-field imaging techniques using polarized noble gas are being developed using low temperature superconducting quantum interference devices (SQUIDs).[16,17] Using a low field scanner such as a PMRI system, such studies have the potential of becoming much more affordable while at the same time maintaining the capability to image water. Nevertheless, significant advances in imaging with polarized ^{129}Xe at any field will require improvement in the polarization values that can be achieved, now typically 5% (compared to the 40%–50% range available with ^{3}He).

This work was supported by the National Science Foundation, under Grant No. PHY-72192, the National Institutes of Health, under Grant No. 1 R21 CA7972801, and the W. M. Keck Foundation Fund for Discovery in Basic Medical Research at the California Institute of Technology. One of the authors (B.A.C.) thanks the Natural Sciences and Engineering Research Council of Canada for fellowship support. One of the authors (E.W.H.) thanks the Alfred P. Sloan Foundation (Grant No. BR-3602) for its support of this work.

[1] P. T. Callaghan, *Principles of Nuclear Magnetic Microscopy* (Oxford University Press, New York, 1993).

[2] M. S. Albert, G. D. Cates, B. Driehuys, W. Happer, B. Saam, C. S. Springer, and A. Wishnia, Nature (London) **370**, 199 (1994).

[3] Y. Q. Song, B. M. Goodson, and A. Pines, Spectroscopy (Eugene, OR) **14**, 26 (1999).

[4] A. Macovski and S. M. Conolly, Magn. Reson. Med. **30**, 221 (1993).

[5] P. Morgan, S. Conolly, G. Scott, and A. Macovski, Magn. Reson. Med. **36**, 527 (1996).

[6] T. G. Walker and W. Happer, Rev. Mod. Phys. **69**, 629 (1997).

[7] E. E. de Lange, J. P. Mugler, J. R. Brookeman, J. Knight-Scott, J. D. Truwit, C. D. Teates, T. M. Daniel, P. L. Bogorad, and G. D. Cates, Radiology **210**, 851 (1999).

[8] J. R. Johnson, A. K. Thompson, T. E. Chupp, T. B. Smith, G. D. Cates, B. Driehuys, H. Middleton, N. R. Newbury, E. W. Hughes, and W. Meyer, Nucl. Instrum. Methods Phys. Res. A **356**, 148 (1995).

[9] C. H. Tseng, G. P. Wong, V. R. Pmeroy, R. W. Mair, D. P. Hinton, D. Hoffmann, R. E. Stoner, F. W. Hersman, D. G. Cory, and R. L. Walsworth, Phys. Rev. Lett. **81**, 3785 (1998).

[10] L. Darrasse, E. Durand, G. Guillot, P. Nacher, and G. Tastevin, Magn. Reson. Mater. Phys., Biol., Med. **6**, 101 (1998).

[11] B. A. Chronik, R. Venook, A. Macovski, S. M. Conolly, and G. C. Scott, Syllabus of the ISMRM Workshop on Limits of Detection in Nuclear Magnetic Resonance, Berkeley, CA, June 2001.

[12] R. J. Fitzgerald, M. Gatzke, D. C. Fox, G. D. Cates, and W. Happer, Phys. Rev. B **59**, 8795 (1999).

[13] E. Brunner, M. Haake, L. Kaiser, A. Pines, and J. A. Reimer, J. Magn. Reson. A **138**, 155 (1999).

[14] R. W. Mair, C.-H. Tseng, G. P. Wong, D. G. Cory, and R. L. Walsworth, Phys. Rev. E **61**, 2741 (2000).

[15] R. W. Mair, G. P. Wong, D. Hoffmann, M. D. Hurlimann, S. Patz, L. M. Schwartz, and R. L. Walsworth, Phys. Rev. Lett. **83**, 3324 (1999).

[16] K. Schlenga, R. McDermott, J. Clarke, R. E. de Souza, A. Wong-Foy, and A. Pines, Appl. Phys. Lett. **75**, 3695 (1999).

[17] M. P. Augustine, A. Wong-Foy, J. L. Yarger, M. Tomaselli, A. Pines, D. M. Ton That, and J. Clarke, Appl. Phys. Lett. **72**, 1908 (1998).